Multifunctional Hierarchical Cellular Solids

Yongtao Sun

Multifunctional Hierarchical Cellular Solids

Tesi per il conseguimento del titolo di Dottore di Ricerca
XXV Ciclo (A.A. 2010; 2011; 2012)

Dottorato di Ricerca in Ingegneria delle Strutture
Politecnico di Torino

Gennaio 2013

Dottorato di Ricerca in Ingegneria delle Strutture
Politecnico di Torino
10129 Torino, Italia
Tutore: Prof. Nicola M. Pugno
Coordinatore: Prof. Alberto Carpinteri

To My Family

Acknowledgements

I appreciate my tutor Prof. Nicola M Pugno very much for his continous and patient supervisions. If the scientific research is a sea, at first I was a student who was not familiar with the sea and was even afraid of the water. Prof. Pugno taught me how to swim hand by hand and day by day I learned swimming myself. Now I become very interested in swimming in the sea of Science and enjoy it very much evey day. I am very indebted to my friend Qiang Chen, he helps me a lot and sets a very good example to me. I am also indebted to my friends in our group, Abdalrahman Tamer, Lepore Emiliano, Federico Bosia and all those who have accompanied and helped me in the past three years. Finally, I would like to express my deep appreciations to the China Scholarship Council (CSC) for the financial support, without it I should not have the chance to study at Italy.

Contents

Summary

Due to their peculiar low density properties, cellular solids are widely used in industries and play a very important role in our daily life. Two of the most studied celluar solids are honeycombs and foams. With the development of nanotechnology, another kind of cellular solids - carbon based materials are drawing more and more attentions nowadays, e.g., the carbon nanotube related researches. The other very hot research field is the bio-inspired materials. Many efforts have been made by the scientists all over the world and a lot of insightful results are obtained. No matter the well studied celluar solids or the newly studied natural and artificial materials, what we care about them are not only their mechicanl properties but also the multifunctionality they may display, in order that they could serve the human being more effectively and more conveniently. Therefore, in this thesis we have focused on the multifunctional hierarchical cellular solids.

In the first chapter, by reviewing some recent developments of the cellular solids, honeycombs and carbon nanotube networks, we summarized the potential multifunctionality they show and thus the significance they may be of for practical applications. Based on this simple review, the motivation of this thesis is introduced, which is to explore the multifunctionalities of these two kinds of cellular solids more widely and deeply.

In chapter 2, through the effective media model, the thermal and thermomechanical performances of the two-dimensional metal honeycombs (with relative density less than 0.3), hexagonal, triangular, square and Kagome honeycombs, are systematically studied.

To improve the in-plane stiffness of the regular hexagonal honeycombs, in chapters 3 and 4 we proposed the multifunctional hierarchical honeycombs (MHH). The MHH is constructed by substituting the cell wall of an original regular honeycomb with five different equal mass lattices, hexagonal, triangular, Kagome, re-entrant hexagonal and chiral honeycombs, respectivley. Elastic and transport properties of the MHH with hexagonal, triangular and Kagome substructures are studied. In-plane stiffnesses of the MHH with re-entrant hexagonal and chiral honeycombs are analyzed.

Chapter 5 involves the cellular solids, super carbon nanotubes (STs). To avoid the

diameter shrinkage that the normal STs under uniaxial tension show, a new kind of hierarchical fibers with a negative Poisson's ratio for tougher composites is proposed and their equivalent elastic parameters are calculated. Chapter 6 reported an application of the hierarchical fibers in bridged crack model.

Chapter 7 provides conclusions and an outlook for the future work.

Chapter 1

Introduction

Two of the most peculiar and attractive cellular solids are honeycombs and carbon nanotube networks. In this part, recent developments about the multifunctionality of thess two kinds of cellular solids are reviewed, which may inspire researchers to exploit the properties of honeycombs and carbon nanotube networks more deeply and broadly.

1.1 Introduction

As one common kind of cellular solids, periodic cellular metals are highly porous structures with 20% or less of their interior volume occupied by metals (Evans et al. 2001; Wadley et al. 2003). They are widely used for the cores of light weight sandwich panel structures. And one of the common periodic celluar solids is honeycombs. They have closed cell pores and are well suited for thermal protection while also providing efficient load support, see Fig. 1.1. For example, the hexagonal honeycomb is widely used to enable the design of light weight sandwich panel structures (Bitzer, 1997), for creating unidirectional fluid flows (Lu, 1999), for absorbing the energy of impacts (Zhang & Ashby, 1992), to impede thermal transport across the faces of sandwich panels and for acoustic damping.

Another kind of cellular solids is carbon nanotube networks. Due to the extreme mechanical and thermal properties related to the strong carbon–carbon bonding, and the interesting electronic properties related to the quantum confined structure, nowadays carbon based materials present an enormous variety of forms, such as graphite, diamond, fullerenes, and carbon nanotubes, and play an important role in the development of nanotechnology (Coluci et al., 2006).

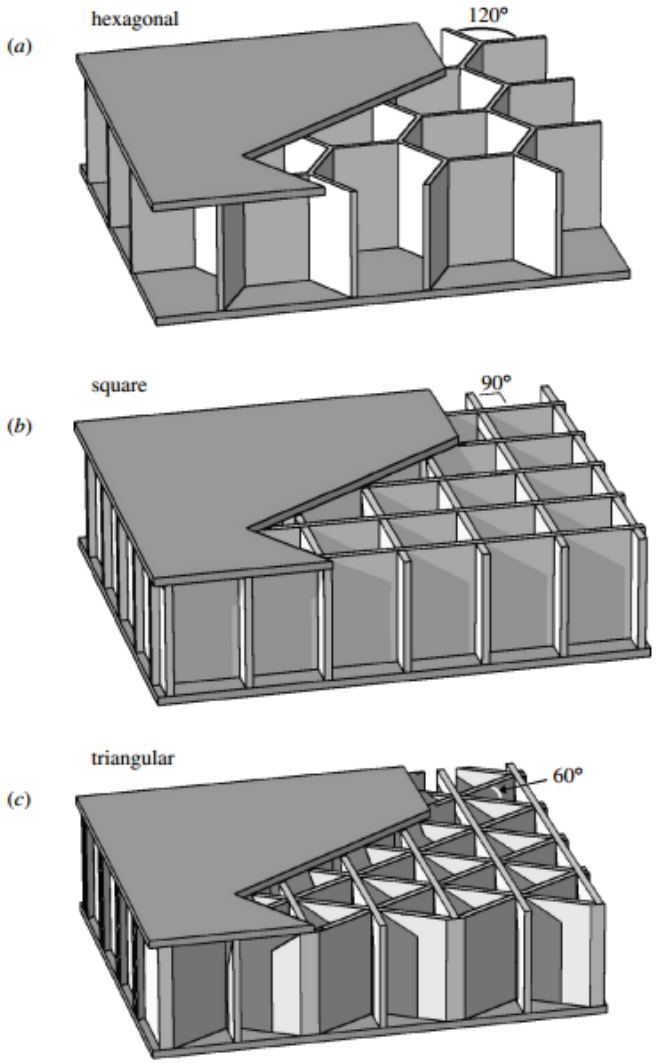

Fig 1.1 Examples of the three forms of honeycomb shown as core structures in sandwich panels: (a) hexagonal honeycomb, (b) square honeycomb and (c) triangular honeycomb. (Wadley, 2006)

In this part we aim to review some recent developments about the multifunctionality of honeycombs and carbon nanotube networks, which could be meaningful in inspiring us to exploit the properties of honeycombs and carbon nanotube based materials more deeply and broadly.

1.2 Honeycombs

With respect to their deformation properties under in-plane loads, honeycombs can be generally divided into two kinds, the regular honeycombs and the negative Poisson's ratio (NPR) honeycombs. Many review works have been done by the researches, in which the mechanical properties, multifunctionality and fabrication processes of the cellular metal systems are summarized (Evans et al., 1999, 2001; Wadley et al., 2003; Wadley, 2006). In this part, we mainly review the multifunctional properties of some of the common regular honeycombs and NPR honeycombs.

1.2.1 Conventional honeycombs

In this part, we simply summarize some properties of the regular honeycombs, mechanical, thermal and blast wave mitigation properties and the role of hierarchy may play on honeycombs.

Mechanical properties

Except the low density property, mechanical properties of honeyboms can be said to have drawn the first attentions in the theoretical and applied research fields. Therefore, they have been most widely and well studied. Gibson and Ashby (1999) systematically revealed the in-plane and out-of-plane structural and properties of honeycombs. Wang and McDowell (2004) investigated the in-plane stiffness and yield strength of different periodic metal honeycombs, and showed that the diamond, triangular and Kagome cells have superior in-plane mechanical properties to the hexagonal, rectangular and mixed square/triangular cells. Fleck and Qiu (2007) analyzed the damage tolerance property of 2D elastic-brittle isotropic honeycombs and reported that the Kagome cells have much higher fracture toughness than those of hexagonal and triangular cells.

Thermal properties

By treating the honeycombs as the core of the compact heat for cooling of multi-chip module by forced convection (Fig. 1.2), Lu (1999) and Gu et al. (2001)

reported that regular hexagonal metal cells, comparing with triangular and square cells, provide the highest level of heat dissipation (Fig 1.3), as comparable to that of open-cell metal foams.

Combining the experimental and numerical methods, Wen et al. (2006) revealed that the overall thermal performance of metal honeycomb structures are superior to other heat sink media, such as metal foams, lattice-frame materials, 3D Kagome structures and woven textile structures. Hyun and Torquato (2002), employing the topology optimization technique, showed that the effective conductivity of the regular hexagonal honeycomb is nearly approaching the Hashin-Shtrikman upper bounds and for the triangular and Kagome honeycombs, both the in-plane effective moduli and conductivity are approaching the Hashin-Shtrikman (H-S) upper bounds (Hashin and Shtrikman, 1962; Hashin and Shtrikman, 1963). Hayes et al. (2004) studied the mechanical and thermal properties of linear cellular alloys with square cells, and concluded that mechanical and heat transfer characteristics of the honeycomb materials outperformed those of open- and closed-cell metal foams with comparable relative density.

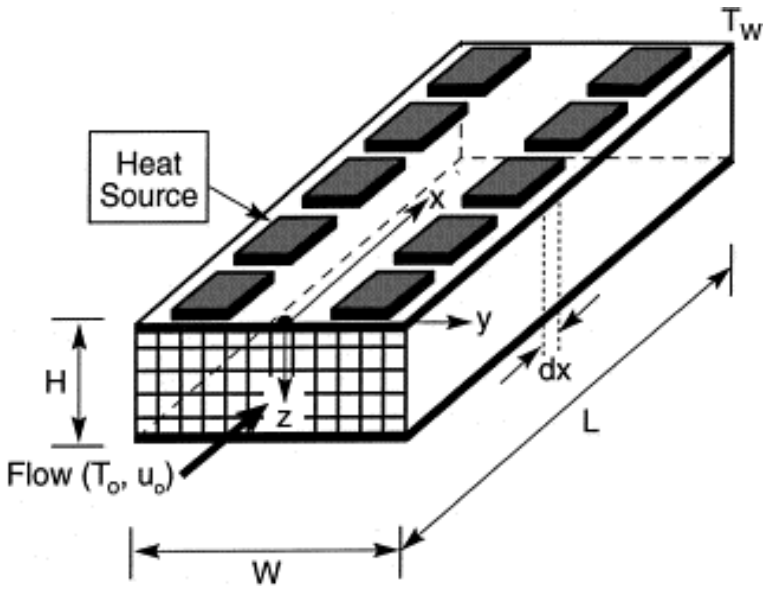

Fig. 1.2 Prototypical design of compact heat sink with two-di-mensional metal honeycombs for cooling of multi-chip module by forced convection (Gu et al., 2001).

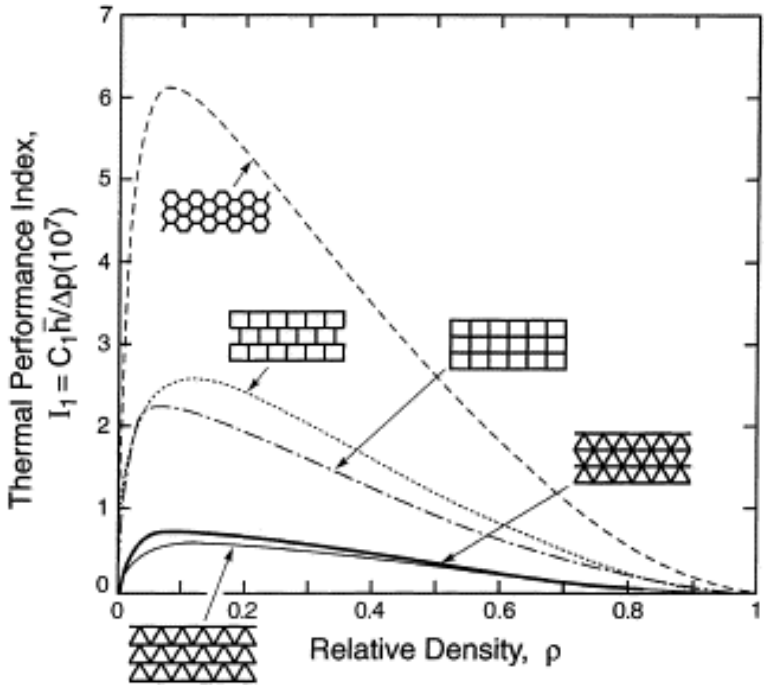

Fig. 1.3 Thermal performance index I_1 plotted as a function of relative density for triangular, square and hexagonal structures.

Blast wave mitigation

Another function of honeycombs is blast wave mitigation, i.e., using the sandwich panel concepts to disperse the mechanical impulse transmitted into structures thereby reducing the pressure applied to a protected structure located behind. A schematic illustration of this concept is shown in Fig. 1.4. Numerical and exprimental results show that significant performance improvements can be achieved through the use of periodical cellular materials (Xue and Hutchinson, 2003; Xue & Hutchinson 2004; Fleck and Deshpand, 2004; Qiu et al. 2004 ; Hutchinson & Xue 2005;Wadley, 2006). One example of a honeycomb core sandwich panel fabricated from high ductility stainless steel subjected to strong air blast shock loadings is shown in Fig. 1.5. The comparison between the sandwich panel and the response of solid plate is apparent.

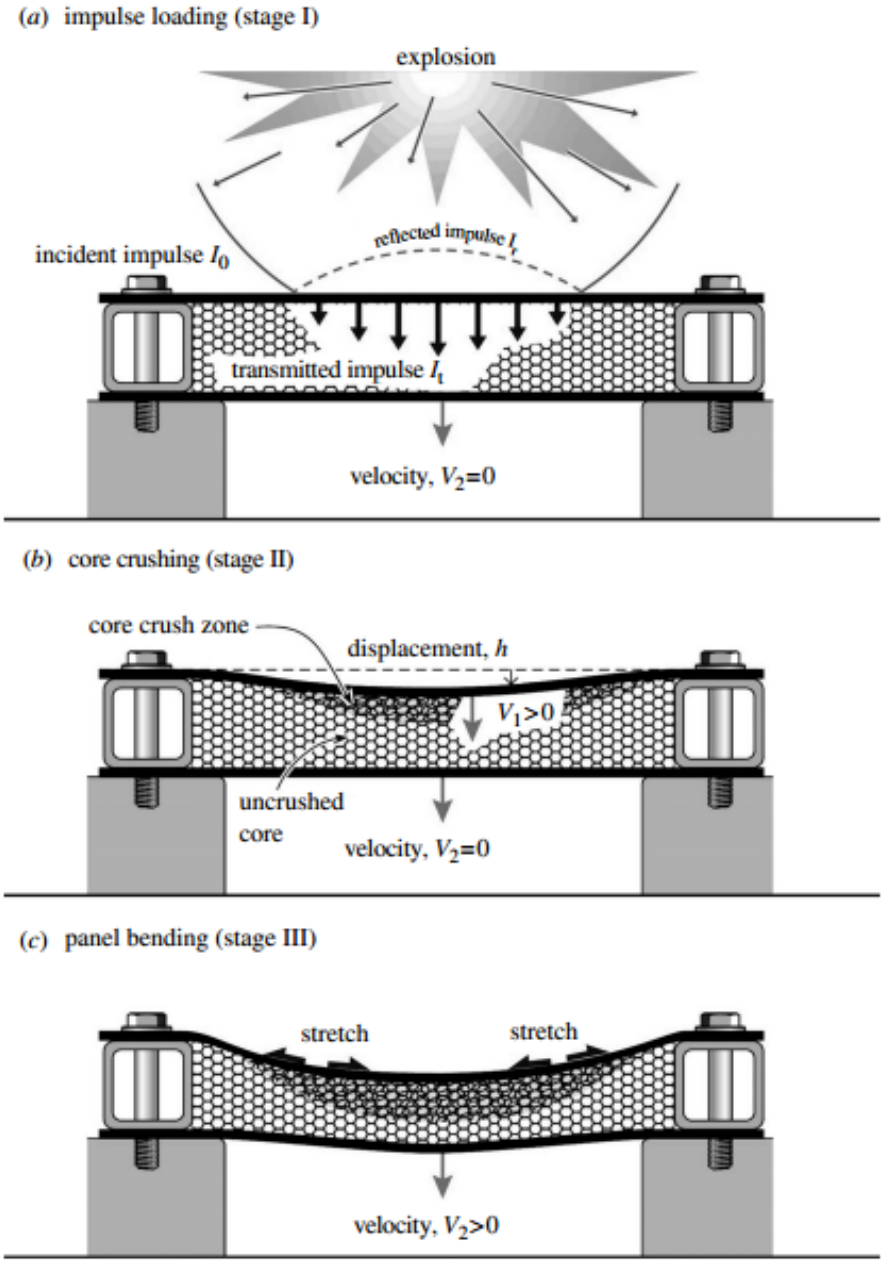

Fig. 1.4 Air blast mitigation concept using a sandwich panel and its response to blast loading (Wadley, 2006)

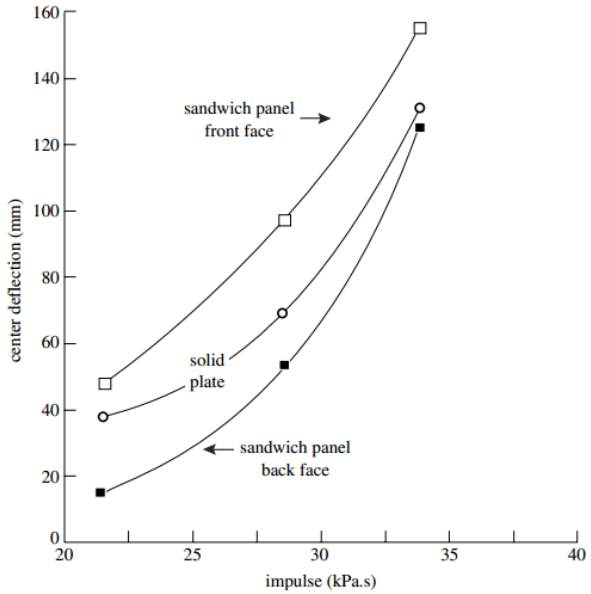

Fig. 1.5 Measurements of the sandwich panel front and back face deflections as a function ofapplied impulse compared with solid plate centre deflections(Wadley, 2006)

Hierarchical honeycombs

Low-density cellular materials widely exist in Nature and exhibit fascinating mechanical properties in the aspects of strength, stiffness, toughness, etc. One common characteristic among them is the hierarchical structures. Inspiring by natural materials, many researchers have tried to introduce the concept of hierarchy to improve the properties of honeybombs. And the results are appealing. Fratzl and Weinkamer (2007) reviewed the basic principles involved in designing hierarchical biological materials, such as cellular and composite architectures, adapative growth and as well as remodeling, and used wood, bone, tendon, and glass sponges as illustrations. Chen and Pugno (2012a) reviewed some well-studied and newly-studied natural materials, and summarize their hierarchical structures and mechanisms behind their mechanical properties, from animals (nacre, gecko feet, mussel, spider silk, crabs, armadillo and turtle shells) to plants (diatoms and plant stem). Introducing the concept of hierarchy and surface effects of nanoscale into honeycomb, our group studied the properties of the hierarchical honeycomb materials, in which the elasticity, in-plane buckling and

bending collapses are analyzed (Pugno and Chen, 2011; Chen and Pugno, 2012b,c). Taylor et al. (2011) introduced the functionally graded hierarchical honeycombs by performing a set of finite element analyses, and the results suggested that the elastic modulus of the functionally graded hierarchical honeycomb can be up to 1.75 times that of its equal-mass first-order hexagonal honeycomb if the structure was designed properly. Different from Taylor's work, Ajdari et al. (2012) developed a new hierarchical honeycomb structure by replacing every three-edge joint of a regular hexagonal lattice with a smaller hexagon, and showed that the elastic moduli of the hierarchical honeycombs with one level and two levels can be 2.0 and 3.5 times stiffer than their equal-mass regular hexagonal honeycomb, respectively.

1.2.2 Negative Poisson's ratio honeycombs

The Poisson's ratio of a material influences the transmission and reflection of stress waves, the decay of stress with distance according to Saint Venant's principle, and the distribution of stress around holes and cracks (Lakes, 1993). Negative Poisson's ratio honeycombs may be of use in new kinds of fasteners, due to the lateral deformation, and in sandwich panels for aircraft or automobiles, due to the convex shapes under bent.

Since many reviews have been done before, in this section, we only shortly summarize some developments about the NPR honeycombs, the re-entrant honeycombs and the chiral honeycombs.

Re-entrant honeycombs

Macroscopic auxetic cellular structures in the form of 2D re-entrant honeycombs were first reaized in 1982 (Fig. 1.6), deforming predominantly by flexure of the ribs of the honeycomb cells (Gibson, 1982; Evans et al., 2000). Compared with the conventional honeycombs, the re-entrant honeycombs can have increased compressive strength and shear stiffness, enhanced indentation resistance (toughness), self-adaptive vibration damping and shock absorption etc. For comprehensive reviews, many papers can be referred (Lakes, 1993; Evans and Alderson, 2000; Yang et al., 2004; Stavroulakis, 2005; Alderson and Alderson, 2007; Scarpa, 2008; Greaves, 2011).

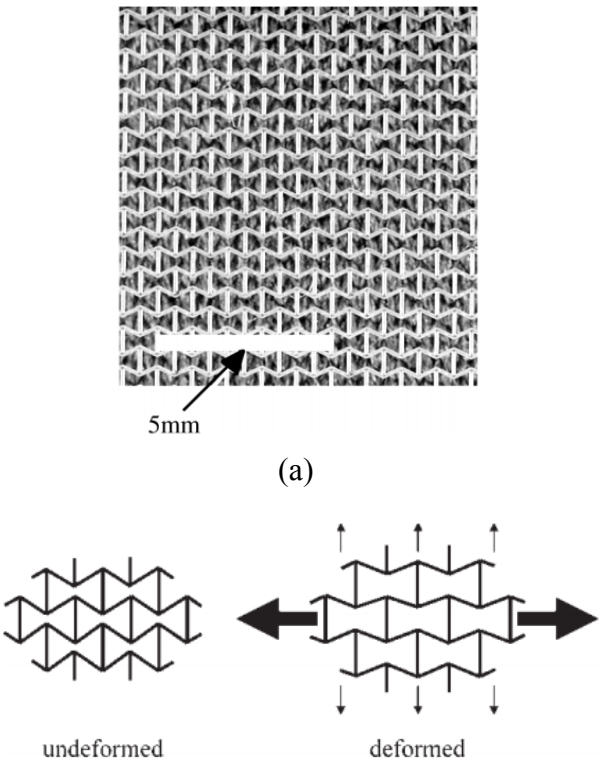

Fig. 1.6 (a) Polymeric re-entrant honeycomb membrane fabricated by femtosecond laser ablation. Pores are approximately 1 mm in width along the horizontal direction (Evans et al., 2000); (b) re-entrant honeycomb in the underformed and deformed states (Alderson and Alderson, 2007).

Chiral honeycombs

The hexachiral honeycomb (Fig. 1.7a) was first analyzed by Prall and Lakes (1996), it is isotropic in-plane and maintains a Possion's ratio -1 over a significant range of strain. Then other kinds of chiral honeycombs are also introduced (Figs. 1.7b-e). Chiral cellular solids could provide significant advantages over conventional hexagonal honeycombs, the compressive and shear strengths are partially decoupled between the cylinders and the ligaments and both the off axis deformations and the electromagnetic functionality of the honeycomb is tuneable through variation of honeycomb geometry (Lorato et al., 2010).

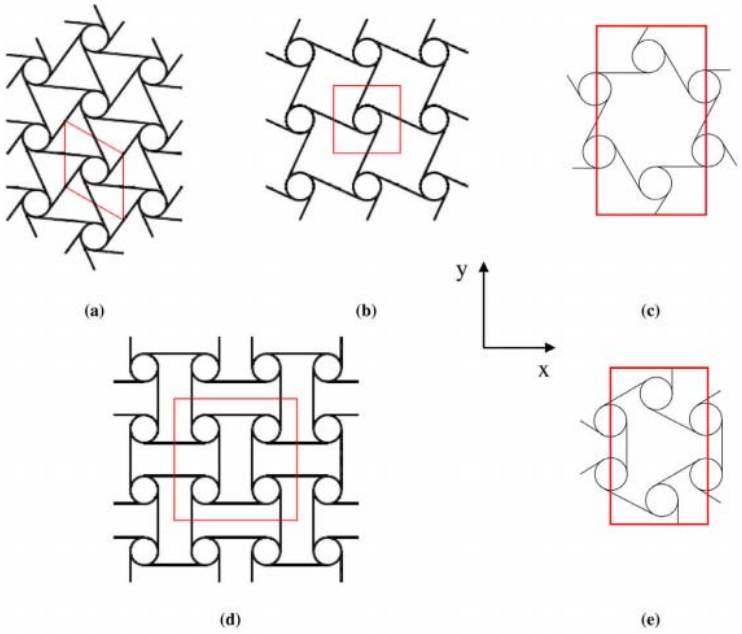

Fig. 1.7 Cell geometries for the auxetic chiral, anti-chiral, and conventional centre-symmetric and hexagonal structures: (a) hexachiral, (b) tetrachiral, (c) trichiral, (d) antitetra chiral, and (e) anti tri chiral(Lorato et al., 2010).

In the aspect of mechanical properties, through numerical and finite element methods, Spadoni et al. (2005) and Scarpa et al. (2007) analyzed the bulking behavior of the hexagonal chiral honeycombs. Miller et al. (2010) did the flatwise buckling optimization of hexachiral and tetrachiral honeycombs and implied that the ligaments act as mixed stiffeners-elastic foundations during flatwise compressive loading, providing different buckling mode shapes for them during deformations. Lorato et al. (2010) revealed the transverse elastic properties of chiral honeycombs shown in Fig. 1.7 and showed that the chiral honeycombs have two distinct upper and lower bounds for the different connectivities, while regular hexagonal honeycombs have coincident bounds. Spadoni and Ruzzene (2012) proved the elasto-static micropolar behavior of the chiral auxetic lattice.

In the aspect of multifunctionality, many attractive results are obtained. Combining numerical and experimental methods, Spadoni et al. (2006) investigated the dynamic behavior of a truss-core beam composed of a hexagonal chiral-honeycomb

core and constraining layers. Results showed that at specific excitation frequencies the resonance of the presented truss-core beam produces localized deformations far from the excitation region, which suggested using the hexagonal chiral honeycombs for the design of innovative lifting bodies, such as helicopter rotor blades or airplane wings. Then, they introduced the chiral truss-core airfoils and studied their static compliance properties. Numerical and experimental results confirmed the ability of chiral-core airfoils to sustain large deflections while not exceeding yield strain limits (Spadoni and Ruzzene, 2007a, b). After that, they developed a manufacturing process for composite chiral structures for morphing airfoils (Bettini et al., 2009). They also studied the phononic properties of hexagonal chiral honeycombs and suggest these cellular lattices as potential building blocks for the design of meta-materials of interest for acoustic wave-guiding applications (Spadoni et al., 2009). Kopyt et al. (2010) investigated the electromagnetic properties of mechanically chiral honeycomb structures and showed that higher order harmonics due to structure periodicity are attenuated away from the panel surface at frequencies up to several GHz, which covers a number of popular ISM bands, and demonstrated that the structural chirality does not translate into chiral electromagnetic behaviour.

1.3 Carbon nanotube networks

In the last few years, due to their special mechanical and electronical properties, hierarchical covalent 2D and 3D networks based on 1D nanostructures have attracted much research attention. One relevant example is carbon nanotube (CNT) networks, in which carbon nanotubes are covalently connected through different nanojunctions such as X-, Y-, T-shape (Terrones et al., 2002; Romo-Herrera et al. 2007; Dimitrakakis et al., 2008; Li et al., 2009a, b; Zsoldos, 2011) and the fractal ways (Yin et al., 2008; 2010). In this section, recent developments about the multifunctional 2D and 3D carbon nanotube networks are simply reviewed.

1.3.1 Super carbon nanotubes

One of the most attractive 2D and 3D carbon nanotube networks is the super carbon nanotubes (STs) (Fig. 1.8). The concept of the self-similar hierarchical super

carbon nanotubes (STs) is first proposed by Coluci et al. (2006). These structures are built from carbon nanotubes connected by Y-junctions forming a super-graphene that is then rolled to form a carbon ST. Such a procedure can be repeated several times, generating a hierarchical macroscopic tube. Through tight binding total energy and density of states calculations, Coluci et al. (2006) showed that these super-tubes can present either metallic or semiconducting behaviour, be prototypes for electromechanical actuators, and serve as hosts for large biomolecules. Li et al. (2008a) showed that the STs could be used to design the new generation of mass and strain sensors due to its high sensitivity and ultra-low density.

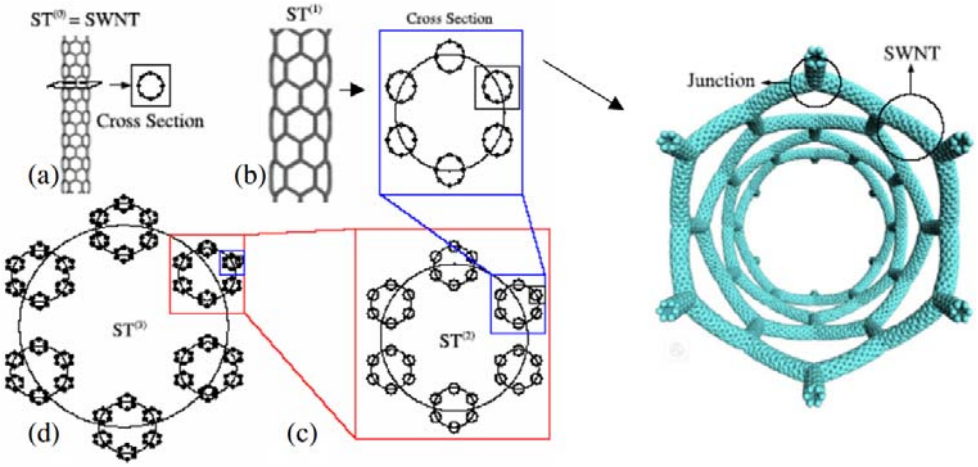

Fig. 1.8 Generation of STs (Pugno, 2006). A nanotube ($ST^{(0)}$) is considered as the fundamental unit (a); an $ST^{(1)}$ is generated by substituting the carbon bonds by entire nanotubes (see the schematic view on the right) (b); thus an $ST^{(2)}$ will present $ST^{(1)}$ bonds (c), and an $ST^{(3)}$ will present $ST^{(2)}$ bonds (d), and so on. After *N* iterations the hierarchical $ST^{(N)}$ is generated.

With respect to the mechanical proeperties, through the fractal method, Pugno (2006) evaluated the strength, toughness and stiffness of the STs-reinforced composites and revealed that the optimized number of hierarchical levels is 2, similar to the optimization done by Nature in nacre (Zhang et al., 2011) and in other biological or bio-inspired materials (Wang and Boyce, 2010). In addition, different numerical methods have been exploited, such as the continuum (Wang et al., 2007a, b), molecular dynamics (Coluci et al., 2007; Qin et al., 2008) and molecular structure mechanics (Li et al., 2008a, b) methods. These numerical simulations generally show that the moduli

of the STs were almost independent of the chirality of the ST, slightly affected by its arm tube chirality and determined mainly by the arm tube aspect ratio (Li et al., 2008c), and that with the increase of the hierarchical level the stiffness and modulus of the STs reduced significantly.

1.3.2 Other 2D and 3D carbon nanotube networks

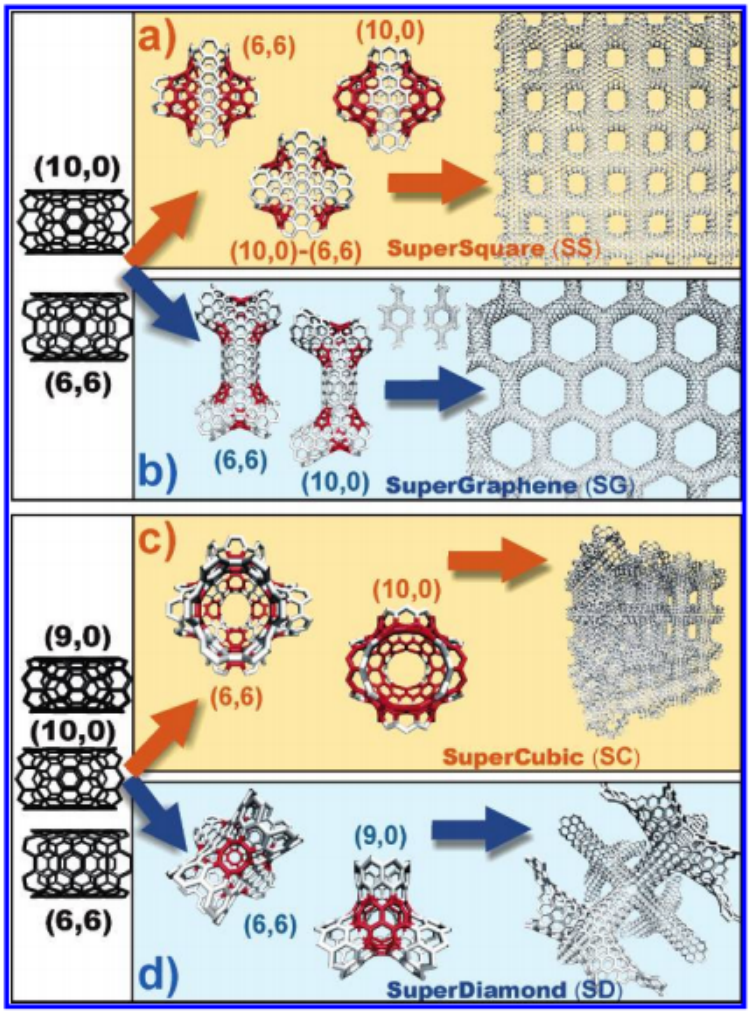

Fig. 1.9 Illustration of four different 2D or 3D CNT networks based on 1D nanostructures (CNTs) (Romo-Herrera et al., 2007). (a) 2D super square built by 'X' junction, (b) 2D super hexagon built by

'Y' junction, (c) 3D super cubic built by 4-terminal junction with cubic network node and (d) 3D super diamond built by 4-terminal junction with tetrahedral architecture.

Except the hierarchical STs, there are also many other kinds of 2D and 3D carbon nanotube networks. Romo-Herrera et al. (2007) experimently created 2D super square, hexagonal and 3D super cubic, diamond carbon nanotube networks (Fig. 1.9). They found that the mechanical and electronic characteristics of these ordered networks based on carbon nanotubes are dominated by their specific super-architecture. And they showed that charges follow specific paths through the nodes of the multi-terminal systems, which could result in complex integrated nanoelectronic circuits.

With respect to the mechanical properties, using the shell model of the finite element method Wang et al. (2007) analyzed the super hexagonal CNT networks and showed that they have great flexibility and outstanding capability in force transferring and the network configuration increases the ductility of the nanomaterials. Through the molecular structural mechanics method, li et al. (2009a; 2010) studied the tensile deformation mechanism and elastic bulking of the super square and hexagonal CNT networks. They showed that under uniaxial tensile loading in the principle direction, the super square could be regarded as a stretching-dominated network, while the super hexagon as a bending-dominated network. On the aspect of bulking, the super square and hexagonal CNT networks are more stable structures than the graphene structures with less carbon atoms. Through the same method Liu et al. (2009) explored the deformation and failure modes of the super square and hexagonal CNT networks, involving rotation, bending and stretching of the CNT arms.

With respect to the multifunctionality, Menon and Srivastava (1997) proposed the CNT "T Junctions" and suggested their potential applications in nanoscale metal-semiconductor-metal contact devices. By exerting chemically induced capillary forces upon the nanotubes Correa-Duarte et al. (2004) fabricated the multiwalled carbon nanotubes (MWCNTs) based thin film networks, which are in principle ideal candidates for scaffolds/matrices in tissue engineering. Day et al. (2005) proposed the use of single-walled carbon nanotube (SWNT) networks as templates for the electrodeposition of metal (Ag and Pt) nanostructures. Meng et al. (2009) suggested using carbon nanotube networks to synthesize nanocomposites with enhanced thermoelectric properties. Besides, using the quantized molecular structural mechanics method, Li et al. (2009b) predicted the thermal properties of the super square and

hexagonal CNT networks and revealed their potential applications in fabricating excellent loudspeakers.

1.4 Conclusions

In this part, recent developments about the multifunctionality of honeycombs and carbon nanotube networks are reviewed. With respect to different deformation mechanism, honeycombs are divided into two kinds, the conventional honeycombs and the negative Possion's ratio honeycombs. The mechanical properties and different multifunctional potential applications on these two kinds of honeycombs are summarized. At the same time, the multifunctional applications of different 2D and 3D carbon nanotube networks, such as STs, super square and hexagonal CNT networks etc., are also simply reviewed.

The following chapters of this thesis will involve more multifunctional applications of these two kinds of common cellular solids.

References

Ajdari, A., Jahromi, B.H., Papadopoulos, J., Nayeb-Hashemi, H., Vaziri, A., 2012. Hierarchical honeycombs with tailorable properties. International Journal of Solids and Structures, http://dx.doi.org/10.1016/j.ijsolstr.2012.02.029

Alderson, A., Alderson, K.L., 2007. Auxetic materials. Proceedings of the Institution of Mechanical Engineers, Part G: Journal of Aerospace Engineering 221, 565-575.

Bitzer, T., 1997. Honeycomb technology. London: Chapman & Hall.

Bettini, P., Airoldi, A., Sala, G., Di Landro, L., Ruzzene, M., Spadoni, A., 2009. Composite chiral structures for morphing airfoils: Numerical analyses and development of a manufacturing process. Composites: Part B (2009), doi:10.1016/j.compositesb.2009.10.005

Chen, Q., Pugno, N.M., 2012a. Bio-mimetic mechanisms of natural hierarchical materials: A review. Journal of the Mechanical Behavior of Biomedical Materials, http://dx.doi.org/10.1016/j.jmbbm.

2012 .10.012

Chen, Q., Pugno, N., 2012b. In-plane elastic buckling of hierarchical honeycomb materials, European Journal of Mechanics A/Solids 34, 120-129.

Chen, Q., Pugno, N., 2012c. Competition between in-plane buckling and bending collapses in nano-honeycombs. Europhysics Letters 98, 16005.

Coluci, V. R., Galvao D.S., Jorio, A., 2006. Geometric and electronic structure of carbon nanotube networks: 'super'-carbon nanotubes. Nanotechnology 17, 617-621.

Coluci, V.R., Pugno, N., Dantas, S.O., Galvao, D.S., Jorio, A., 2007. Atomistic simulations of the mechanical properties of 'super' carbon nanotubes. Nanotechnology 18, 335702.

Correa-Duarte, M.A., Wagner, N., Rojas-Chapana, J., Morsczeck, C., Thie, M., Giersig, M., 2004. Fabrication and biocompatibility of carbon nanotube-based 3D networks as scaffolds for cell seeding and growth. Nano Letters 4, 2233-2236.

Day, T.M., Unwin, P.R., Wilson, N.R., Macpherson, J.V., 2005. Electrochemical templating of metal nanoparticles and nanowires on single-walled carbon nanotube networks. JACS, 127, 10639-10647.

Dimitrakakis, G.K., Tylianakis, E., Froudakis, G.E., 2008. Pillared Graphene: A New 3-D Network Nanostructure for Enhanced Hydrogen Storage. Nano Letters 8, 3166-3170.

Evans, A.G., Hutchinson, J.W., Ashby, M.F., 1999. Multifunctional of cellular metal systems. Progress in Materials Science 43, 171-221.

Evans, K.E., Alderson, A., 2000. Auxetic Materials: Functional Materials and Structures from Lateral Thinking. Advanced Materials 12(9), 617-628.

Evans, A.G., Hutchinson, J. W., Fleck, N. A., Ashby, M. F. & Wadley, H. N. G. 2001.The topological design of multifunctional cellular metals. Progress in Materials Science 46, 309-327.

Fleck, N.A., Qiu, X.M., 2007. The damage tolerance of elastic–brittle, two-dimensional isotropic

lattices. Journal of the Mechanics and Physics of Solids, 55(3), 562-588.

Fleck, N.A., Deshpande, V.S., 2004. The resistance of clamped sandwich beams to shock loading. Journal of Applied Mechanics 71, 386-401.

Fratzl, P., Weinkamer, R., 2007. Nature's hierarchical materials. Progress in Materials Science 52, 1263-1334.

Gibson, L.J., Ashby, M.F., Schajer, G.S., Robertson, C.I., 1982. The Mechanics of two-dimensional cellular materials. Proceedings of the Royal Society A 382 (1782), 25-42.

Gibson, L.J., Ashby, M.F., 1997. Cellular Solids, Structures and Properties, second ed. Cambridge University Press.

Greaves G.N., Greer, A.L., Lakes, R.S., Rouxel, T., 2011. Poisson's ratio and modern materials. Nature Materials 10, 823-837.

Hashin, Z., Shtrikman, S., 1962. A variational approach to the theory of the effective magnetic permeability of multiphase materials. Journal of Applied Physics 33(10), 3125- 3131.

Hashin, Z., Shtrikman, S., 1963. A variational approach to the theory of the elastic behaviour of multiphase materials. Journal of the Mechanics and Physics of Solids 11(2), 127-140.

Hutchinson, J.W., Xue, Z., 2005. Metal sandwich plates optimized for pressure impulses. International Journal of Mechanical Sciences 47, 545-569.

Hayes, A.M., Wang, A., Dempsey, B.M., McDowell, D.L., 2004. Mechanics of linear cellular alloys. Mechanics of Materials 36, 691-713.

Hyun, S., Torquato, S., 2002. Optimal and manufacturable two-dimensional, Kagome-like cellular solids. Journal of Materials Research 17, 137-144.

Kopyt, P., Damian, R., Celuch, M., Ciobanu, R., 2010. Dielectric properties of chiral honeycombs-Modelling and experiment. Composites Science and Technology 70: 1080-1088.

Lakes, R., 1993. Advances in negative Poisson's ratio materials. Advanced Materials 5, 293-296.

Li, Y., Qiu, X.M., Yang, F., Wang, X.S., Yin, Y.J., 2008a. Ultra-high sensitivity of super carbon-nanotube-based mass and strain sensors. Nanotechnology 19, 165502.

Li, Y., Qiu, X.M., Yang, F., Wang, X.S., Yin, Y.J., 2008b. The effective modulus of super carbon nanotubes predicted by molecular structure mechanics. Nanotechnology 19, 225701.

Li, Y., Qiu, X.M., Yang, F., Wang, X.S., Yin, Y.J., Fan, Q.S., 2008c. A comprehensive study on the mechanical properties of super carbon nanotubes. Journal of Physics D: Applied Physics 41, 155423.

Li , Y., Qiu, X., Yang, F., Yin, Y., Fan, Q., 2009a. Stretching-dominated deformation mechanism in a super square carbon nanotube network. Carbon 47, 812-819.

Li , Y., Qiu, X., Yang, F., Yin, Y., Fan, Q., 2009b. The specific heat of carbon nanotube networks and their potential applications. Journal of Physics D: Applied Physics 42, 155405.

Li, Y., Qiu, X., Yang, F., Yin, Y., Fan, Q., 2010. The elastic buckling of super-graphene and super-square carbon nanotube networks. Physics Letters A 374, 1773-1778.

Liu, X., Yang, Q.S., He, X.Q., Mai, Y.W., 2011. Molecular mechanics modeling of deformation and failure of super carbon nanotube network. Nanotechnology 22, 475701.

Lorato, A., Innocenti, P., Scarpa, F., Alderson, A., Alderson, K.L., Zied, K.M., Ravirala, N., Miller, W., Smith, C.W., Evans, K.E., 2010. The transverse elastic properties of chiral honeycombs. Composites Science and Technology 70, 1057-1063.

Lu, T.J., 1999. Heat transfer efficiency of metal honeycombs. International Journal of Heat and Mass Transfer 42, 2031-2040.

Meng, C., Liu, C., Fan, S., 2010. A promising approach to enhanced thermoelectric properties using carbon nanotube networks. Advanced. Materials 22, 535-539.

Menon, M., Srivastava, D., 1997. Carbon Nanotube "T Junctions": Nanoscale

metal-semiconductor-metal contact devices. Physical Review Letters 79, 4453-445.

Miller, W., Smith, C.W., Scarpa, F., Evans, K.E., 2010. Flatwise buckling optimization of hexachiral and tetrachiral honeycombs. Composites Science and Technology 70, 1049-1056

Prall, D., Lakes, R. S., 1996. Properties of a chiral honeycomb with a Poisson's ratio -1. International Journal of Mechanical Sciences 39, 305-314.

Pugno, N.M., 2006. Mimicking nacre with super-nanotubes for producing optimized super-composites. Nanotechnology 17, 5480-5484.

Pugno, N., Chen, Q., 2011. In plane elastic properties of hierarchical cellular solids, Engineering Procedia, Physics Engineering 10, 3026-3031.

Qin, Z., Feng, X.Q., Zou, J., Yin, Y.J., Yu, S.W., 2008. Molecular Dynamics Simulations of Deformation and Rupture of Super Carbon Nanotubes Under Tension. Journal of Nanoscience and Nanotechnology 8, 6274-6282.

Qiu, X., Deshpande, V.S., Fleck, N.A., 2004. Dynamic response of a clamped circular sandwich plate subject to shock loading. Journal of Applied Mechanics 71, 637-645.

Romo-Herrera, J. M., Terrones, M., Terrones, H., Dag, S., Meunier, V., 2007. Covalent 2D and 3D Networks from 1D Nanostructures: Designing New Materials. Nano Letters 7, 570-576.

Scarpa, F., 2008. Auxetic Materials for Bioprostheses. Signal Processing Magazine, IEEE 25(5), 126-128

Scarpa, F., Blain, S., Lew, T., Perrott, D., Ruzzene, M., Yates, J.R., 2007. Elastic buckling of hexagonal chiral cell honeycombs. Composites: Part A 38, 280-289.

Spadoni A., M. Ruzzene, and F. Scarpa 2005. Global and local linear buckling behavior of a chiral cellular structure. Physica Status Solidi(b), 242(3), 695-709.

Spadoni, A., Ruzzene M., Scarpa, F., 2006. Dynamic response of chiral truss-core assemblies. Journal of Intelligent Material Systems and Structures 17, 941-952.

Spadoni, A., Ruzzene, M., 2007a. Numerical and experimental analysis of the static compliance of chiral truss-core airfoils. Journal of Mechanics of Materials and Structures 2, 965-981.

Spadoni, A., Ruzzene, M., 2007b. Static aeroelastic response of chiral-core airfoils. Journal of Intelligent Material Systems and Structures18, 1067-1075.

Spadoni A., Ruzzene M., Gonella S., Scarpa F., 2009. Phononic properties of hexagonal chiral lattices. Wave Motion 46, 435-450.

Spadoni, A., Ruzzene, M., 2012. Elasto-static micropolar behavior of a chiral auxetic lattice. Journal of the Mechanics and Physics of Solids 60:156-171.

Stavroulakis, G.E., 2005. Auxetic behaviour: appearance and engineering applications. Physica Status Solidi (b) 242(3), 710-720.

Taylor, C.M., Smith, C.W., Miller, W., Evans, K.E., 2011.The Effects of hierarchy on the in-plane elastic properties of honeycombs. International Journal of Solids and Structures 48, 1330-1339.

Terrones, M., Banhart, F., Grobert, N., Charlier, J.C., Terrones, H., Ajayan, P.M., 2002. Molecular Junctions by Joining Single-Walled Carbon Nanotubes. Physical Review Letters., 89, 075505.

Wadley, H.N.G., Fleck, N.A., Evans, A.G., 2003. Fabrication and structural performance of periodic cellular metal sandwich structures. Composites Science and Technology 63, 2331-2343.

Wadley, H.N.G., 2006. Multifunctional periodic cellular metals. Philosophical Transactions of the Royal Society A 364, 31-68.

Wang, A.J., McDowell, D.L., 2004. In-plane stiffness and yield strength of the periodic metal honeycombs. Journal of Engineering Materials and Technology 126, 137-156.

Wang, L., Boyce, M.C., 2010. Bioinspired structural material exhibiting post-yield lateral expansion and volumetric energy dissipation during tension.Advanced Functional Materials 20, 3025-3030.

Wang, M., Qiu, X.M., Zhang, X., 2007a. Mechanical properties of super honeycomb structures based on carbon nanotubes. Nanotechnology 18, 075711.

Wang, M., Qiu, X.M., Zhang, X., Yin, Y.J., 2007b. Equivalent parameter study of the mechanical properties of super carbon nanotubes. Nanotechnology 18, 295708.

Wen, T., Tian, J., Lu, T.J., Queheillalt, D.T., Wadley, H.N.G., 2006. Forced convection in metallic honeycomb structures. International Journal of Heat and Mass Transfer 49, 3313-3324.

Xue, Z., Hutchinson, J.W., 2003. Preliminary assessment of sandwich plates subject to blast loads. International Journal of Mechanical Sciences 45, 687-705.

Xue, Z., Hutchinson, J.W., 2004. A comparative study of impulse-resistant metal sandwich plates. International Journal of Impact Engineering 30, 1283-1305.

Yang, W., Li, Z.M., W., Shi, B.H., Xie, Yang, M.B., 2004. Review on auxetic materials. Journal of Materials Science 39, 3269-3279.

Yin, Y.J., Zhang, T., Yang, F., Qiu, X., 2008. Geometric conditions for fractal super carbon nanotubes with strict self-similarities. Chaos, Solitons and Fractals 37, 1257-1266.

Yin, Y.J., Fan, Q.S., Yang, F., Li, Y., 2010. Super carbon nanotubes, fractal super tubes and fractal super fibres. Materials Science and Technology 26, 1327-1331.

Zhang, J., Ashby, M.F., 1992. The out-of-plane properties of honeycombs. International Journal of Mechanical Sciences 34, 475-489.

Zhang, Z., Zhang, Y., Gao, H.,2011. On optimal hierarchy of load-bearing biological materials, Proceedings of the Royal Society B: Biological Sciences 278, 519-525.

Zsoldos, I., 2011. Planar trivalent polygonal networks constructed from carbon nanotube Y-junctions. Journal of Geometry and Physics 61, 37-45

Chapter 2

Optimized design of the two-dimensional metal honeycombs

In this chapter, through the effective media model, the thermal and thermomechanical performances of the two-dimensional metal honeycombs (with relative density less than 0.3), hexagonal, triangular, square and Kagome honeycombs, are systematically studied. Dry air and water are chosen as the cooling media, respectively. Results show that the heat transfer properties of the hexagonal, triangular, square honeycombs are independent of the input velocity of the forced convection but it has great influence to Kagome honeycombs. With respect to the overall thermal performance, regular hexagonal honeycombs are found to provide the highest level of heat dissipation. About the thermomechanical performance, i.e., when combined heat dissipation and structural load capacity are considered, the optimized structural morphology is related to the cooling media used. When dry air is chosen as the cooling fluid, for heat sinks with relatively thin cellular cores, the thermomechanical performance of triangular honeycombs outperforms those of hexagonal, square and Kagome honeycombs; for high heat flux scenarios, however, Kagome honeycombs are the best. When water is chosen as the cooling fluid, the thermomechanical performance of Kagome honeycombs generally outperforms those of the other three kinds of honeycombs greatly.

2.1 Introduction

As a kind of peculiar lightweight materials, the two-dimensional metal honeycombs have attracted much attention in the past years (Huang and Gibson, 1994; Masters and Evans, 1996; Gibson and Ashby, 1997; Wang and McDowell, 2004; Fleck and Qiu 2007). According to different requirments, in engineering structures there are mainly two arrangements for them. One is the core of sandwich panels, where the cell axis is perpendicular to the panel skins (Wilson, 1990; Bitzer, 1994; Thompson and Matthews, 1995; Price et al., 2001); the other one is the heat sink, where the cell axis is parallel to the panel skins (Lu, 1999; Gu et al. 2001; Wen et al., 2006). For the former one the structural load capacity, i.e., the high stiffness/strength at minimum weight, is essential; for the latter one, the combined heat dissipation and structural load capacity, i.e., the multifunctionalities, are predominated.

To investigate the multifunctionalities of the two-dimensional metal honeycombs, many methods have been exploited. Through the topology optimization technique Hyun and Torquato (2002) revealed that for the regular hexagonal honeycomb the effective conductivity is nearly approaching the Hashin-Shtrikman upper bounds and for the triangular and Kagome honeycombs both the in-plane effective moduli and conductivity are approaching the Hashin-Shtrikman (H-S) upper bounds (Hashin and Shtrikman, 1962; Hashin and Shtrikman, 1963). Through the experimental and numerical methods, Wen et al. (2006) revealed that the overall thermal performance of metal honeycomb structures are superior to other heat sink media, such as metal foams, lattice-frame materials, 3D Kagome structures and woven textile structures. In addition, Wen et al. (2007) employed the intersection-of-asymptotes method for structural optimization of two-dimensional cellular metals cooled by forced convection.

At the same time, the analytical methods are also developed. Through the corrugated wall model Lu (1999) studied the heat transfer efficiency of the hexagonal metal honeycombs and showed that the optimal cell morphology is not constant but dependent upon the geometry and heat transfer condition of the heat sink as well as the

type of convective cooling medium used. Comparing the corrugated wall model and the effective media model, Gu et al. (2001) investigated different types of cell shape and cell arrangement including regular hexagon, square with connectivity 4 or 3, and triangle with connectivity 6 or 4. They concluded that for high heat flux scenarios, hexagonal cells outperform triangular and square cells. We have carefully checked their results and did not arrive at this conclusion. Besides, using dry air as the cooling fluid, through the effective media model Wang et al. (2007) performed the multifunctional design of sandwich panels with Kagome-like cores. However, they did not consider the influence of the velocity of the input cooling fluid on the combined honeycombs (Kagome honeycombs) and also we did not arrive at the results they showed for Kagome honeycombs (Figs. 1-9 in their paper).

In this paper, through the effective media model the heat transfer efficiencies of the two-dimensional metal honeycombs (with relative density less than 0.3), hexagonal, triangular, square and Kagome honeycombs, are systematically studied. Dry air and water are chosen as the cooling fluids to show the effect of cooling media on the structural optimization. More systematic and complete conclusions for structural optimization of these multifunctional two-dimensional metal honeycombs are given.

2.2 Physical model

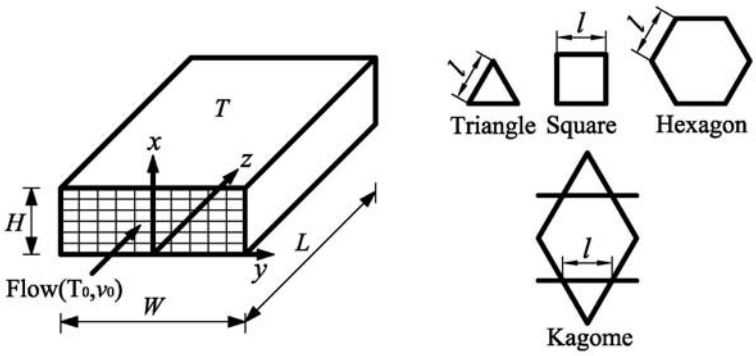

Fig. 2.1 Physical model of the heat sink with different two-dimensional metal cellular cores for

cooling by forced convection (Wang et al., 2007)

The physical model of the heat sink with the core of different two-dimensional metal honeycomb cells is shown in Fig. 2.1. The detailed description of this model has been done by Gu et al. (2001) and Wang et al. (2007), so here we only simply introduce it. Its thickness, width and length are *H*, *W* and *L*, respectively. The honeycomb cells, with cell size *l*, cell wall thickness *t* and relative density ρ , are uniformly distributed in the core. The bottom ($x = 0$) and top ($x = H$) surfaces are the heat sources with the high temperature *T*. The cooling fluid, with velocity v_0 and temperature T_0, is forced into the cellular core at the inlet $z = 0$. The width *W* is assumed to be much larger than the cell size *l* in order that both the thermal and hydraulic fields are independent of the *y*-coordinate. The steady-state flow and constant thermal/physical properties are assumed for both fluid and solid. In addition, the isothermal boundary conditions are assumed. And the process-induced geometrical imperfections for the cellular cores are neglected.

2.3 Indexes of the optimized design

The heat transfer performance of the heat sink is measured by the ratio of the overall heat transfer coefficient to the pumping power needed to force the fluid through (Gu et al. 2001; Wang et al., 2007) and the non-dimensional index, i.e., the thermal performance index, is:

$$I_1 = c\bar{h}/\Delta p \tag{2.1}$$

in which $c = \mu_f \rho_f v_0 / k_s$ (μ_f and ρ_f are the kinematic viscosity and density of the cooling fluid; k_s is the thermal conductivity of the metal), $\bar{h}$ is the overall heat transfer coefficient of the cellular core and Δp is the pressure drop of the laminar flow. The higher the value I_1 , the better the heat sink performance.

Furthermore, since it is important for the heat sink to sustain a defined structural load, another non-dimensional index, the thermomechanical index, for the combined

heat transfer performance and structural load capacity, is introduced:

$$I_2 = \frac{G}{E_s} I_1 = c \frac{G}{E_s} \frac{\bar{h}}{\Delta p} \tag{2.2}$$

in which G and E_s are the shear modulus of the cellualr core and the Young's modulus of the metal, respectively. The reason why here the non-dimensional shear stiffness G/E_s is used as a relevant measure of the structural utility is that the cellular core shear has a major influence on the minimum weights realized in practice (Budiansky, 1999; Gu et al. 2001).

The calculations of I_1 and I_2 for all the cellular cores shown in Fig. 2.1, i.e., the calculations of the overall heat transfer coefficient $\bar{h}$ and the pressure drop Δp, will be discussed in detail below.

2.4 The overall heat transfer coefficient

In this section, through the effective media model we calculate the overall heat transfer coefficient, $\bar{h}$, of the cellular cores given in Fig. 2.1. The effective media model is a model involving the volume-average method in which the properties of each phase are averaged separately within a representative unit element (i.e., individual cells) and correlated with bulk properties of the pure phases (Gu et al. 2001). The following concept in this section is translated from the paper of Wang et al. (2007) which is written in Chinese.

Let k_x be the effective thermal conductivity in the x-direction of the heat sink and $\alpha_A h$ be the heat source coefficient, where α_A and h stand for the surface area density and local heat transfer coefficient for each cell shape. And the nominal temperature of the fluid in cross section z is defined as $T_f(z)$. After reaching the steady-state, the governing equations and boundary conditions of the structural temperature, $\theta(x,z)$, can be expressed as:

$$\begin{cases} \dfrac{\partial^2\theta(x,z)}{\partial x^2}-\dfrac{\alpha_A h}{k_x}\left[\theta(x,z)-T_f(z)\right]=0 \\ \theta(0,z)=\theta(H,z)=T \end{cases} \tag{2.3}$$

in which the heat loss at the heat sink surfaces has been neglected and it has been assumed that $\left|\partial\theta/\partial x\right|\geq\left|\partial\theta/\partial z\right|$ (i.e., most of the heat flux through the solid is normal to the fluid flow). Defining $m_x^2=\alpha_A h/k_x$, from Eq. (2.3) we can get

$$\theta(x,z)=T_f(z)+\left[T-T_f(z)\right]\frac{\sinh\left[m_x(H-x)\right]+\sinh\left[m_x x\right]}{\sinh\left[m_x H\right]} \tag{2.4}$$

The heat transfers on the bottom and up surfaces of the heat sink are

$$\begin{cases} q_1=-k_x\int_0^W \left.\dfrac{\partial\theta(x,z)}{\partial x}\right|_{x=0}\mathrm{d}y \\ q_2=-k_x\int_0^W \left.\dfrac{\partial\theta(x,z)}{\partial x}\right|_{x=H}\mathrm{d}y \end{cases} \tag{2.5}$$

Then the total heat flowing into the heat sink is

$$Q=q_1-q_2=l_1+l_2T_f(z) \tag{2.6}$$

in which $l_1=2k_x m_x W\tanh\left(m_x H/2\right)T$ and $l_2=-l_1/T=-2k_x m_x W\tanh\left(m_x H/2\right)$. From the local energy balance, we get

$$c_p\rho_f v_f(1-\rho)HW\frac{dT_f(z)}{dz}=Q=l_1+l_2T_f(z) \tag{2.7}$$

where c_p , ρ_f and v_f are the heat capacity, density and average velocity (over the length L) of fluid. Solving Eq. (2.7) gives

$$T_f(z)=T+(T_0-T)\exp\left(l^* z\right) \tag{2.8}$$

in which $l^*=l_2\left/\left[c_p\rho_f v_f(1-\rho)HW\right]\right.$. Then, the averaged fluid temperature (over the length L), $\overline{T}_f$, and the outlet temperature (at $z=L$), $T_{f,out}$, can be expressed as

$$\overline{T}_f=\frac{1}{L}\int_0^L T_f(z)\mathrm{d}z=T+\frac{T_0-T}{l^*L}\left[\exp(l^*L)-1\right] \tag{2.9}$$

$$T_{f,out} = T_f(L) = (T_0 - T)\exp(l^* L) + T \tag{2.10}$$

Subsequently, the overall heat balance implies that

$$\bar{h}\left(T - \bar{T}_f\right) \times 2WL = c_p \rho_f v_f (1-\rho) HW \left(T_{f,out} - T_0\right) \tag{2.11}$$

Finally, combining Eqs. (2.8) to (2.11), the overall heat transfer coefficient, $\bar{h}$, is obtained

$$\bar{h} = -\frac{l_2}{2W} = k_x m_x \tanh\left(m_x H/2\right) \tag{2.12}$$

2.5 Pressure drop and other related effective coefficients

2.5.1 The traditional honeycombs

In this section, we talk about the pressure drop and other related effective coefficients for the heat sink with the core of hexagonal, square and triangular cells.

For laminar flow, the pressure drop, i.e., the pumping power needed to force the cooling fluid through the heat sink, is (Gu et al. 2001)

$$\Delta p = \frac{(f\,\mathrm{Re})c_a^2}{8l^2(1-\rho)^2} L \mu_f \rho_f v_0 \tag{2.13}$$

in which μ_f is the kinematic viscosity of the fluid; the frictional coefficient $f\,\mathrm{Re}$=13.3, 14.17, 15.07 and c_a = 6.93, 4.0, 2.31 for triangular, square and hexagonal cells, respectively.

The heat source coefficient, $\alpha_A h$, reflecting the heat change capacity between the cooling fluid and the cellular core, is expressed as (Gu et al. 2001)

$$\alpha_A h = \frac{c_a^2 Nuk_f}{4l^2} \tag{2.14}$$

where k_f is the thermal conductivity of the cooling fluid and the Nusselt number

$Nu = 3.0, 3.614, 4.021$ for triangular, square and hexagonal cells, respectively. In addition, the effective thermal conductivities, k_x, in the *x*-direction of the heat sink for the triangular, square and hexagonal cores are the same

$$k_x = 0.5\rho k_s \tag{2.15}$$

Besides, the in-plane shear moduli for the triangular, square and hexagonal cells are

$$G_{12} = 0.125\rho E_s, G_{12} = 0.0625\rho^3 E_s, \quad G_{12} = 0.375\rho^3 E_s \tag{2.16}$$

respectively.

Combining Eqs. (2.12-2.16) with Eqs. (2.1-2.2), we can obtain the optimized design indexes, I_1 and I_2, for the two-dimensional triangular, square and hexagonal metal honeycombs.

2.5.2 Kagome honeycombs

In this section, we talk about the pressure drop and other related effective coefficients for the heat sink with the core of Kagome honeycombs. Kagome honeycombs are a kind of combined honeycombs which contain multi-geometry honeycomb cells in parallel. The effective pressure drop and heat source coefficient for the heat sink with combined honeycombs, under fully developed laminar flow, have been studied by Shah and London (1978; 1980). Blow we firstly introduce the effective pressure drop and heat source coefficient for the heat sink with the core of general combined honeycombs and then consider those related to the specific Kagome honeycombs.

Effective pressure drop for the general combined honeycombs

Supposing there are *m* honeycombs cells in the heat sink core having *n* different shaped honeycombs in parallel and the total number of the *i*th shaped honeybombs is N_i, we have

$$N_1 + N_2 + \cdots + N_i + \cdots + N_n = m \tag{2.17}$$

Supposing the fluid properties are constant and the same for all honeycomb cells and

neglecting the pressure losses at the inlet and outlet, the effective pressure drop can be determined as follow.

Under fully developed laminar flow, the pressure drop for any one of the *i*th shaped honeybombs is

$$\Delta p = 2\mu_f L \frac{(f\,\mathrm{Re})_i}{A_i D_{h,i}^2} V_i \tag{2.18}$$

Defining $(f\,\mathrm{Re})_e$, P_e, V, A, D_h as the effective frictional coeffiecient, total wetted perimeter, total fluid flow rate, total flow cross section area and effective hydraulic diameter, respectively, then, for the *m*-cell combined honeycombs core

$$\Delta p = 2\mu_f L \frac{(f\,\mathrm{Re})_e}{A D_h^2} V \tag{2.19}$$

in which $A = \sum_{i=1}^{n} N_i A_i$, $P_e = \sum_{i=1}^{n} N_i P_i$, $D_h = \frac{4A}{P_e}$, $V = A v_f \rho_f$. From the continuity equation,

$$v_f = \frac{v_0}{1-\rho} \tag{2.20}$$

$$V = \sum_{i=1}^{n} N_i V_i \tag{2.21}$$

Substituting Eqs. (2.18) and (2.19) into Eq. (2.21) and rearranging it gives

$$\frac{1}{(f\,\mathrm{Re})_e} = \sum_{i=1}^{n} \frac{1}{(f\,\mathrm{Re})_i} \left(\frac{D_{h,i}}{D_h}\right)^2 \left(\frac{N_i A_i}{A}\right) \tag{2.22}$$

Then, equating Eqs. (2.18) and (2.19) yields the flow distribution for each honeycomb cell

$$\frac{V_i}{V} = \frac{(f\,\mathrm{Re})_e}{(f\,\mathrm{Re})_i} \left(\frac{D_{h,i}}{D_h}\right)^2 \left(\frac{A_i}{A}\right) \tag{2.23}$$

which will be used below for calculation of the effective heat source coefficient. Finally, substituting Eq. (2.22) into Eq. (2.19) results in the effective pressure drop

$$\Delta p = \frac{2\mu_f \rho_f L v_0}{(1-\rho) D_h^2} \left[\sum_{i=1}^{n} \frac{1}{(f\,\mathrm{Re})_i} \left(\frac{D_{h,i}}{D_h} \right)^2 \left(\frac{N_i A_i}{A} \right) \right]^{-1} \tag{2.24}$$

Effective heat source coefficient for the general combined honeycombs

Defining Nu_e as the effective Nusselt number of the combined honeycombs core under isothermal boundary conditions, the effective heat source coefficient can be expressed as

$$(\alpha_A h)_e = \frac{Nu_e k_f}{D_h} \alpha_A \tag{2.25}$$

in which α_A is the effective surface area density of the combined honeycomb cells. Nu_e can be calculated through the Shah and London's method (Shah and London, 1978). For the *i*th shaped honeycombs, the number of heat transfer units, $N_{tu,i}$, and the heat transfer effectiveness, ε_i, are given by

$$N_{tu,i} = \left(\frac{hA}{Wc_p} \right)_i = \left(\frac{4k_f L}{c_p \rho_f} \right) \left(\frac{Nu_i}{v_{f,i} D_{h,i}^2} \right) \tag{2.26}$$

$$\varepsilon_i = 1 - \exp\left(-N_{tu,i}\right) \tag{2.27}$$

$v_{f,i}$ is the averaged fluid velocity in the *i*th shaped honeycombs and can be derived from Eq. (2.23)

$$v_{f,i} = \frac{(f\,\mathrm{Re})_e}{(f\,\mathrm{Re})_i} \left(\frac{D_{h,i}}{D_h} \right)^2 v_f \tag{2.28}$$

From energy balance, the averaged heat transfer effectiveness, ε_{ave}, and the averaged number of heat transfer units, $N_{tu,e}$, can be obtained

$$\varepsilon_{ave} = \sum_{i=1}^{n} \frac{N_i W_i}{W} \varepsilon_i \tag{2.29}$$

$$N_{tu,e} = \ln\left(\frac{1}{1-\varepsilon_{ave}} \right) \tag{2.30}$$

Then, referring to Eq. (2.26) gives

$$Nu_e = \left(\frac{c_p \rho_f}{4 k_f L}\right)\left(v_f D_h^2 N_{tu,e}\right) \tag{2.31}$$

Finally, substituting Eq. (2.31) into Eq. (2.25) produces the effective heat source coefficient, $(\alpha_A h)_e$, for the general combined honeycombs.

The related coefficients for Kagome honeycombs

Since Kagome honeycombs is a kind of combined honeycombs, the effective pressure drop and heat source coefficient for Kagome honeycombs core can be obtained by substituting the specific parameters of Kagome honeycombs into the above equations for the general combined honeycombs.

A standard Kagome cell is constituted by 4 regular triangular cells and two regular hexagonal cells. The relative density, ρ, and the effective surface area density, α_A, of the Kagome honeycombs are

$$\rho = \sqrt{3}\frac{t}{l} - \left(\frac{t}{l}\right)^2 \tag{2.32}$$

$$\alpha_A = 4\sqrt{3/4 - \rho}/l \tag{2.33}$$

respectively. According to the heat balance in the *x*-direction, the effective thermal conductivity, k_x, is given by (Wang et al., 2007)

$$k_x = \frac{\sqrt{3}}{2}\frac{t}{l}k_s \approx 0.5\rho k_s \tag{2.34}$$

And the flow cross section area ratios for triangular and hexagonal cells are

$$\begin{cases} \dfrac{4A_T}{A} = \left(\dfrac{3}{2}\sqrt{1-\dfrac{4}{3}\rho} - \dfrac{1}{2}\right)^2 \Big/ \left[4(1-\rho)\right] \\ \dfrac{2A_H}{A} = 3\left(\dfrac{1}{2}\sqrt{1-\dfrac{4}{3}\rho} + \dfrac{1}{2}\right)^2 \Big/ \left[4(1-\rho)\right] \end{cases} \tag{2.35}$$

in which the subscript “T” stands for *Triangle* and “H” stands for *Hexagon*. The

effective hydraulic diameter of the Kagome honeycombs is

$$D_h = 4\frac{A}{P_e} = (1-\rho)l\Big/\sqrt{3/4-\rho} \tag{2.36}$$

The hydraulic diameters of the triangular and hexagonal cells in the Kagome cell are

$$\begin{cases} D_{h,T} = 4\dfrac{A_T}{P_{eT}} = \dfrac{\sqrt{3}}{2}\left(\sqrt{1-\dfrac{4}{3}\rho}-\dfrac{1}{3}\right)l \\ D_{h,H} = 4\dfrac{A_H}{P_{eH}} = \dfrac{\sqrt{3}}{2}\left(\sqrt{1-\dfrac{4}{3}\rho}+1\right)l \end{cases} \tag{2.37}$$

The in-plane stiffness of the Kagome honeycombs is

$$G_{12} = 0.125\rho E_s \tag{2.38}$$

After the properties of the cooling fluid are given, substituting the above parameters into the equations for the general combined honeycombs, we can obtain the optimized design indexes, I_1 and I_2, for the two-dimensional Kagome metal honeycombs.

2.6 Optimized design

In the section, we use some examples to perform the optimized design of the multifunctional two-dimensional metal honeycombs-hexagonal, triangular, square and Kagome honeycombs. The solid metal and the cooling fluids are chosen to be aluminum, the dry air (at 300 K) and water (at 293 K), respectively. The related parameters are $k_s = 200\,\mathrm{W/m\ K}$, $l = 1\,\mathrm{mm}$, $L = 100l$, $\rho = 0.01-0.3$. For the dry air $k_f = 0.026\,\mathrm{W/m\ K}$, c_p=1004.9 J/kg K, $\rho_f = 1.177\,\mathrm{kg/m^3}$, $\mu_f = 1.568\times10^{-5}\,\mathrm{m^2/s}$; for water $k_f = 0.6\,\mathrm{W/m\ K}$, c_p=4183 J/kg K, $\rho_f = 998.3\,\mathrm{kg/m^3}$, $\mu_f = 1.004\times10^{-6}\,\mathrm{m^2/s}$. The ratio, H/l, of the heat sink size, H, to the cell size, l, is a variable and is chosen to discuss the size scale effect of the heat sink. The inlet fluid velocity v_0 is also a variable.

2.6.1 Heat transfer optimization

For heat transfer optimization, the thermal performance index $I_1 = c\bar{h}/\Delta p$ given in Eq. (2.1) is used. $\bar{h}$ can be calculated from Eq. (2.12), Δp for hexagonal, triangular and square honeycombs and for Kagome honeycombs can be obtained from Eqs. (2.19) and (2.24), respectively. From Eqs. (2.1), (2.12) and (2.19) it is easy to see that for hexagonal, triangular and square honeycombs I_1 is independent of v_0. However, for Kagome honeycombs I_1 is dependent of v_0 (See Eqs. (2.1), (2.12) and (2.24)).

We start by using $H/l = 20$ and $v_0 = 1$, 10, 50, 100 m/s to the study the effects of ρ on I_1. The results are shown in Fig. 2.2. In Fig. 2.2 and the following figures, the red arrow represents that along the arrow direction the four lines for Kagome honeycombs correspond to $v_0 = 1$, 10, 50, 100 m/s, respectively. From Figs. 2.2a and 2.2b we can see that for both the cooling media, dry air and water, the thermal performance of hexagonal honeycombs outperforms those of the other three kinds. For all the four kinds of honeycombs there exists the maximum value of I_1, $I_{1\max}$. And the thermal performance of Kagome honeycombs increases with the increase of v_0. Using air as the cooling media, the thermal performance of Kagome honeycombs is generally inferior to that of triangular honeycombs (Fig. 2.2a). However, when using water as the cooling media, the thermal performance of Kagome honeycombs generally outperforms that of triangular honeycombs (Fig. 2.2b).

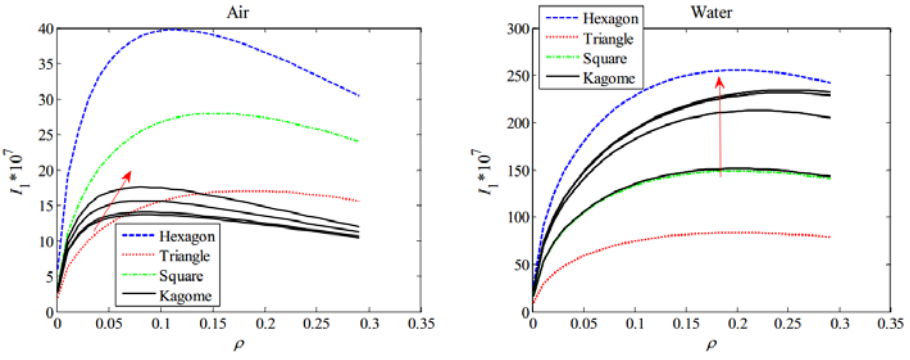

(a) (b)

Fig. 2.2 Thermal performance index I_1 vs ρ at $H/l = 20$ for (a) air; (b) water. (The red arrow here and in the following figures, represents that along the arrow direction the four lines for Kagome honeycombs correspond to $v_0 = 1$, 10, 50, 100 m/s, respectively.)

Defining the relative density corresponds to $I_{1\max}$ as the optimum relative density, ρ_{opt}, then different H/l will correspond to different $I_{1\max}$ and ρ_{opt}. Here we use $H/l = 1-200$ as examples to observe the trends of $I_{1\max}$ and ρ_{opt} with the increase of H/l. The results are reported in Figs. 2.3 and 2.4. From Figs. 2.3a and 2.3b we can see that with the increase of H/l, the thermal performance of hexagonal honeycombs still generally outperforms those of the other three kinds of honeycombs. One interesting phenomenon is that size scale effects exist for the four honeycombs, i.e., when H/l reaches a certain value, $I_{1\max}$ will be a constant. That is to say, after a certain value of

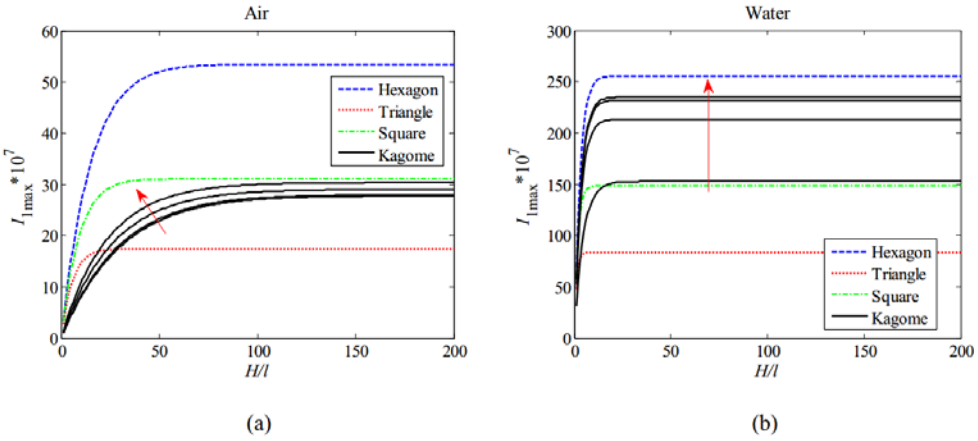

Fig. 2.3 Maximum thermal performance index $I_{1\max}$ vs H/l for (a) air; (b) water.

H/l, increasing H/l (the heat sink size) will not increase the thermal performance of these honeycombs. Figs. 2.4a and 2.4b shows that at first the optimum relative density ρ_{opt} increases with the increase of H/l, but after H/l reaches a certain value, ρ_{opt} will keep a constant. For hexagonal, triangular and Kagome honeycombs, this constant is 0.2. For Kagome honeycombs, this constant is larger than 0.2 and decreases with the increase of v_0. Comparing Fig. 2.3b with Fig. 2.3a it apparent that, using water as the cooling media, the heat sink thickness (H/l) needed to arrive at $I_{1\max}$ is much smaller than that of the dry air.

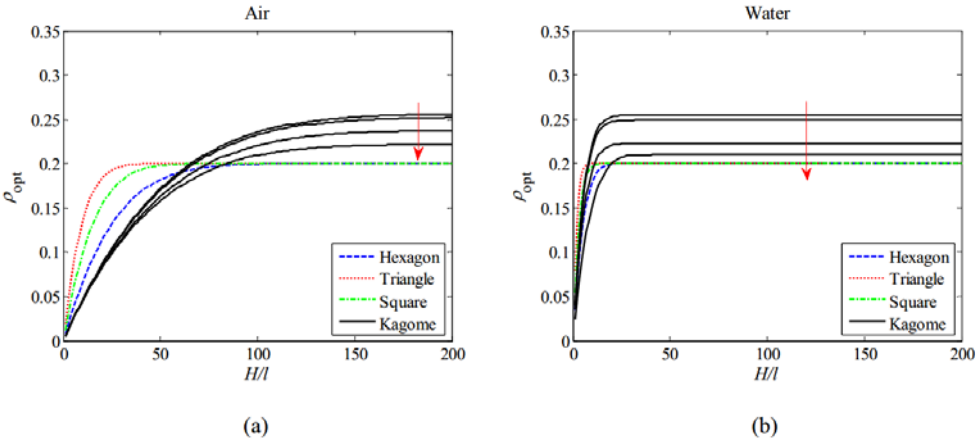

Fig. 2.4 The optimum relative density ρ_{opt} vs H/l for (a) air; (b) water.

2.6.2 Optimization for combined heat transfer and structural load capacity

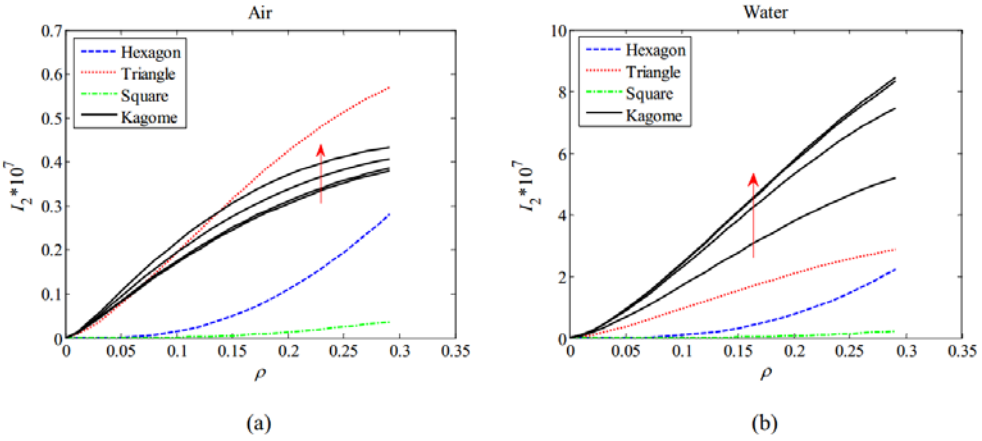

Fig. 2.5 Thermomechancial performance index I_2 vs ρ at $H/l = 20$ for (a) air; (b) water.

For optimization of combined heat transfer and structural load capacity, the thermomechanical index $I_2 = G/E_s\, I_1 = c\left(G/E_s\right)\bar{h}/\Delta p$ given in Eq. (2.2) is used. Still we use the parameter $H/l = 20$ and $v_0 = 1$, 10, 50, 100 m/s to study the effects of ρ

on I_2. The results are given in Fig. 2.5. It is apparent that for all the four kinds of honeycombs, I_2 increases with the increase of ρ. Like I_1, for Kagome honeycombs, I_2 also increases with the increase of v_0. And the thermomechanical performances of Kagome and triangular honeycombs outperform those of the hexagonal and square honeycombs. Using air as the cooling media, at relatively low density, Kagome honeycombs are better than triangular, square and hexagonal honeycombs; however, at relatively high density, triangular honeycombs are better than the other three kinds of honeycombs (Fig. 2.5a). Using water as the cooling media, Kagome honeycombs generally outperform triangular, square and hexagonal honeycombs.

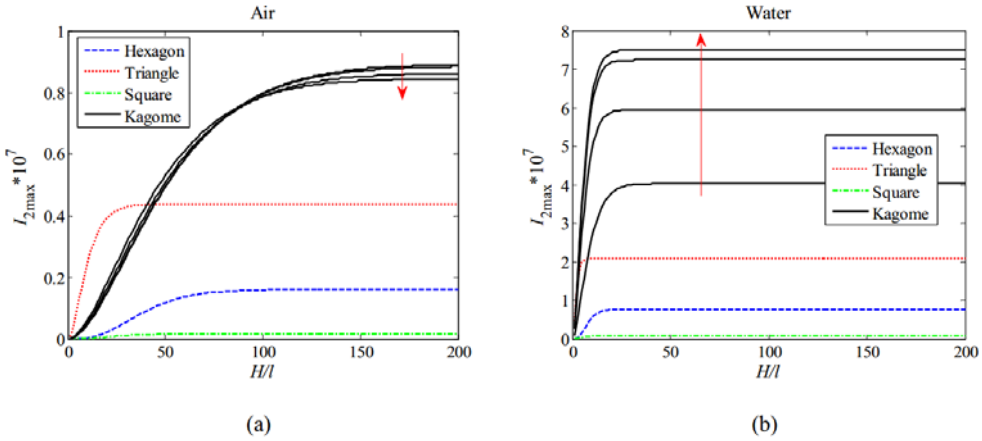

Fig. 2.6 Maximum thermomechancial performance index $I_{2\max}$ vs H/l for (a) air; (b) water.

Since there are no peak values for I_2 (Fig. 2.5), similar to the maximum thermal performance index $I_{1\max}$, the maximum thermomechanical performance index, $I_{2\max}$, is proposed as follow

$$I_2 = \left(\frac{G}{E_s} I_1\right)\Big|_{\max} = I_{1\max}\left(\frac{G}{E_s}\right)\Big|_{\rho_{opt}} \tag{2.39}$$

in which ρ_{opt} is the one corresponding to $I_{1\max}$ and is implicit in Fig. 2.4. The parameters $H/l = 1-200$ are used to the see the effects of heat sink size on $I_{2\max}$. The results are reported in Fig. 2.6. It is evident that the size scale effects also exist for $I_{2\max}$, i.e., when H/l increases to a certain value, the maximum thermomechanical

performance $I_{2\max}$ tends to be a constant.

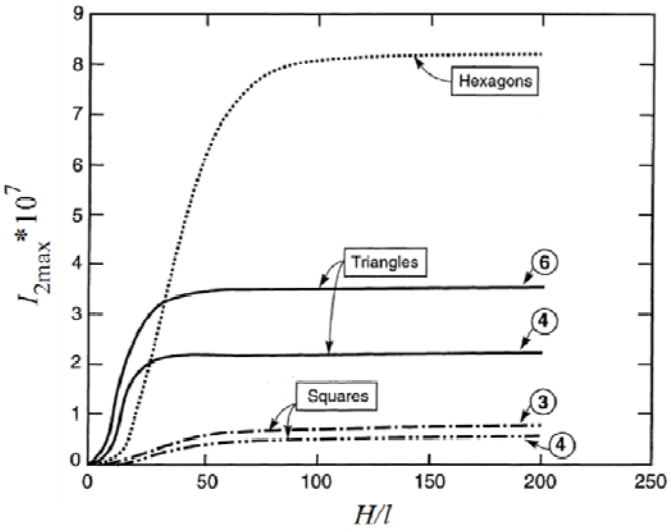

Fig. 2.7 Maximum thermomechancial performance index $I_{2\max}$ vs H/l by Gu et al. (2001)

When dry air is used as the cooling media (Fig. 2.6a), we can see that for heat sinks with relatively thin cores, triangular honeycombs outperform hexagonal, square and Kagome honeycombs. When the ratio, H/l, of the heat sink size to cell size is large than 40, Kagome honeycombs can greatly outperform the other three kinds of honeycombs. And as a whole triangular and Kagome honeycombs greatly outperform hexagonal and square honeycombs, which is different from the conclusion of Gu et al. (2001). Through the corrugated wall model they showed that for heat sink with thick cores, i.e., for high heat flux scenarios, the maximum thermomechanical performance of hexagonal honeycombs outperforms those of triangular and square honeycombs (Fig. 2.7). We have checked their results very carefully and found that it is impossible to arrive at this conclusion. In fact, it is apparent that the thermomechanical performance of hexagonal honeycombs cannot be larger than that of triangular honeycombs. The thermal performance of hexagonal honeycombs is larger than that of triangular honeycombs (Figs. 2.2a and 2.3a), but it is not much larger (less than 10). However, when the non-dimensional in-plane shear modulus is added for the thermomechanical

performance (Eq. (2.2)), the shear modulus of triangular honeycombs ($G_{12}/E_s = 0.125\rho$) are much larger than that of the hexagonal honeycombs ($G_{12}/E_s = 0.375\rho^3$), even when the optimized density of hexagonal honeycombs is larger than that of the triangular honeycombs. So with respect to the combined thermal performance index and the non-dimensional in-plane shear modulus, i.e., the thermomechanical performance, hexagonal honeycombs cannot outperform triangular honeycombs.

When water is used as the cooling media (Fig. 2.6b), generally the thermomechanical performance of Kagome honeycombs are much better than those of triangular, hexagonal and square honeycombs, different from the results of Fig. 2.6a where the dry air is used as the cooling fluid. This implies that the structural morphology optimization is related to the cooling media used.

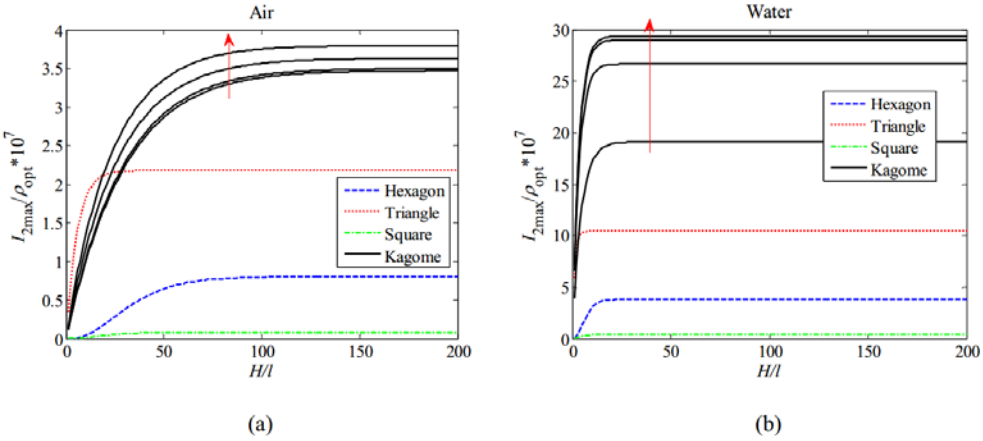

Fig. 2.8 $I_{2\max}/\rho_{\text{opt}}$ vs H/l for (a) air; (b) water.

Considering that when H/l is relative larger the optimum relative density ρ_{opt} for Kagome honeycombs are larger than that for triangular honeycombs (Fig. 2.4), to see the effect of ρ_{opt} on $I_{2\max}$ we plot the relationship between $I_{2\max}/\rho_{\text{opt}}$ and H/l in Fig. 2.8. It is easy to see that the results are similar to those shown in Fig. 2.6, here we do not repeat them any more.

Under the same structural mass, how will the maximum thermomechanical performances change for these four kinds of honeycombs? Defining M as the mass of the cellular core, we can obtain $M = \rho_{\text{opt}} \rho_s LWH$. Rearranging it gives the normalized structural mass of the cellular core of the heat sink

$$M/(\rho_s LWl) = \rho_{\text{opt}} (H/l) \tag{2.40}$$

The normalized structural mass against $I_{2\max}$ is plotted in Fig. 2.9. We can see that, when dry air is the cooling fluid (Fig. 2.9a), under relatively low normalized structural weight, triangular honeycombs are the best; under high normalized structural weight, Kagome honeycombs are the best. When water is the cooling media (Fig. 2.9b), the maximum thermomechanical performance index, $I_{2\max}$, of the Kagome honeycombs increases greatly with the increase of v_0. And under the same normalized structural mass, the thermomechanical performance of Kagome honeycombs generally outperforms hexagonal, triangular and square honeycombs greatly.

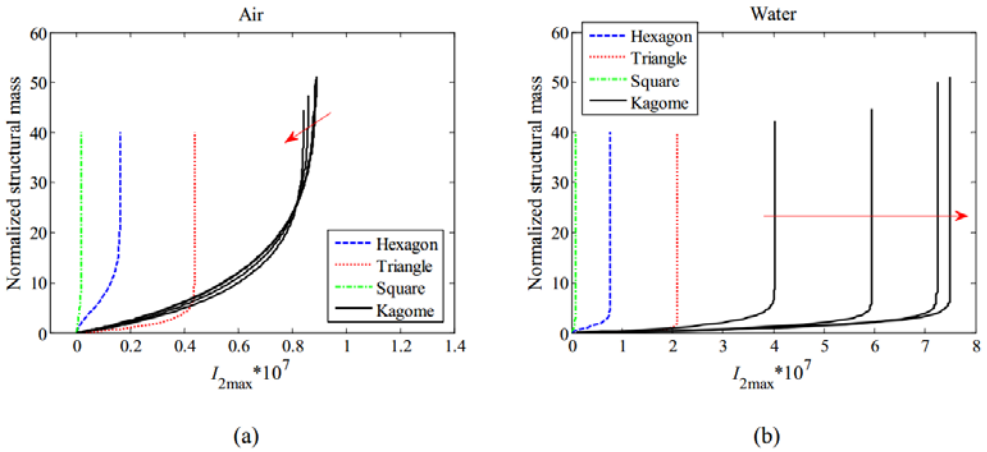

Fig. 2.9 Normalized structural mass vs $I_{2\max}$ (a) air; (b) water.

2.7 Conclusions

Through effective media model, in this chapter the thermal and thermomechanical performances of the hexagonal, triangular, square and Kagome metal honeycombs are

systematically studied. Dry air and water are chosen as the cooling media, respectively. Results show that the heat transfer properties of hexagonal, triangular and square honeycombs are independent of the input velocity of the forced convection but it has great influence to Kagome honeycombs. Considering the thermal performance alone, hexagonal honeycombs are the best. About the thermomechanical property, the optimized structural topology is related to the cooling media used. When dry air is used for the cooling media, for heat sinks with relatively thin cellular cores, triangular honeycombs outperform Kagome, square and hexagonal honeycombs. However, when the ratio between the heat sink size and cell size are relatively large, Kagome honeycombs are better than triangular, square and hexagonal honeycombs. When water is chosen as the cooling media, the thermomechanical performance of Kagome honeycombs generally is much better than the other three kinds of honeycombs, especially for the heat sink where thick cores are needed. This paper implies that for structural design of the heat transfer panels, the structural topology optimization should be performed based on the cooling media used.

References

Bitzer, T., 1994. Honeycomb marine applications. Journal of Reinforced Plastics and Composites 13, 355-360.

Budiansky, B., 1999. On the minimum weights of compression structures. International Journal of Solids and Structures 36, 3677-3708.

Fleck, N.A., Qiu, X., 2007. The damage tolerance of elastic-brittle, two dimensional isotropic lattices. Journal of the Mechanics and Physics of Solids 55, 562-588.

Gibson, L.J., Ashby, M.F., 1997. Cellular Solids, Structures and Properties, second ed. Cambridge University Press.

Gu, S., Lu, T.J., Evans, A.G., 2001. On the design of two-dimensional cellular metals for combined heat dissipation and structural load capacity. International Journal of Heat and Mass Transfer 44, 2163-2175.

Hashin, Z., Shtrikman, S., 1962. A variational approach to the theory of the effective magnetic permeability of multiphase materials. Journal of Applied Physics 33(10): 3125- 3131.

Hashin, Z., Shtrikman, S., 1963. A variational approach to the theory of the elastic behaviour of multiphase materials. Journal of the Mechanics and Physics of Solids 11(2): 127-140.

Huang, J.S., Gibson, L.J., 1994. Microstructural design of cellular materials—I: honeycomb beams and plates. Acta Metallurgica et Materialia 43, 1643-1650.

Hyun, S., Torquato, S., 2002. Optimal and manufacturable two-dimensional, Kagome-like cellular solids. Journal of Materials Research 17, 137-144.

Lu, T.J., 1999. Heat transfer efficiency of metal honeycombs. International Journal of Heat and Mass Transfer 42, 2031-2040.

Masters, I.G., Evans, K.E., 1996. Models for the elastic deformation of honeycombs. Composite Structures 35, 403-422.

Price, T., Timbrook, R.L., 2001, Structural honeycomb panel building system, Patent number US6, 253, 530 B1. 3 July.

Shah, R.K., London, A.L., 1978. Advances in heat transfer: Laminar flow forced convection in ducts. New York: Academic Press, 405-410.

Shah, R.K., London, A.L., 1980. Effects of nonuniform passages on compact heat exchanger performance. ASME, Journal of Engineering for Power 102, 653-659.

Thompson, R.W., Matthews, F.L., 1995. Load attachments for honeycomb panels in racing cars. Materials and Design 16, 131-150.

Wang, A.J., McDowell, D.L., 2004. In-plane stiffness and yield strength of the periodic metal honeycombs. Journal of Engineering Materials and Technology 126, 137-156.

Wang, B., Wang, B., Cheng, G., 2007. Multifunctional design of sandwich panels with Kagome-like cores. Acta Materiae Compositae Sinica 24, 109-115.

Wen, T., Tian, J., Lu, T.J., Queheillalt, D.T., Wadley, H.N.G., 2006. Forced convection in metallic honeycomb structures. International Journal of Heat and Mass Transfer 49, 3313-3324.

Wen, T., Xu, F., Lu, T.J., 2007. Structural optimization of two-dimensional cellular metals cooled by forced convection. International Journal of Heat and Mass Transfer 50, 2590-2604.

Wilson, S., 1990. A new face of aerospace honeycomb. Materials and Design 11, 323-326.

Chapter 3

Elastic and Transport Properties of the Tailorable Multifunctional Hierarchical Honeycombs

Compared with triangular, square and Kagome honeycombs, hexagonal honeycombs have lower in-plane stiffness, which restricts its multifunctional applications. Therefore, in this chapter, considering identical mass with an original regular hexagonal honeycomb (ORHH), we analytically study the in-plane elastic and transport properties of a new class of hexagonal honeycombs, i.e., multifunctional hierarchical honeycomb (MHH). The MHH structure is developed by replacing the solid cell walls of the ORHH with three kinds of isotropic honeycomb sub-structures possessing hexagonal, triangular and Kagome lattices. Formulas to derive the effective in-plane elastic properties of the regular hexagonal honeycombs at all densities are developed for analyzing the MHH structure. The results show that the hexagonal sub-structure is difficult to greatly improve the elastic properties of the MHH structure, however, its counterparts, the triangular or Kagome sub-structures, result in a substantial improvement by 1 magnitude or even 3 orders of magnitude on the Young's and shear moduli of the MHH structure, depending on the cell-wall thickness-to-length ratio of the ORHH. Besides, the effective in-plane conductivities (or dielectric constants) of the three different MHH structures are also studied, generally they are smaller than the ORHH structure except for some

cases of the MHH with Kagome structure. The presented theory could be used in designing new tailorable hierarchical honeycomb structures for multifunctional applications.

3.1 Introduction

Low-density cellular materials widely exist in Nature and exhibit fascinating mechanical properties in the aspects of strength, stiffness, toughness, etc. (Huang and Gibson, 1994; Masters and Evans, 1996; Gibson and Ashby, 1997). As one typical kind of low density cellular solids, honeycombs, which are mainly used as cores of the light-weight sandwich panel structures (Wilson, 1990; Bitzer, 1994; Thompson and Matthews, 1995; Price et al., 2001), have seen many applications in different fields, such as in aerospace and automotive industries. Apart from the fantastic low-density and mechanical properties, honeycombs also show other attractive functionalities, e.g., heat transfer, thermal protection, catalysis application and so on. In order to find optimal topologies for different multifunctional applications, varieties of prismatic honeycombs have been studied in recent years.

Up to date, from the point of view of multifunctionalities, Lu (1999) and Gu et al. (2001) reported that regular hexagonal metal cells, comparing with triangular and square cells, provide the highest level of heat dissipation, as comparable to that of open-cell metal foams. Combining the experimental and numerical methods, Wen et al. (2006) revealed that the overall thermal performance of metal honeycomb structures are superior to other heat sink media, such as metal foams, lattice-frame materials, 3D Kagome structures and woven textile structures. Hyun and Torquato (2002), employing the topology optimization technique, showed that the effective conductivity of the regular hexagonal honeycomb is nearly approaching the Hashin-Shtrikman upper bounds and for the triangular and Kagome honeycombs, both the in-plane effective moduli and conductivity are approaching the Hashin-Shtrikman (H-S) upper bounds (Hashin and Shtrikman, 1962; Hashin and Shtrikman, 1963). Besides, Evans et al. (2001), Wadley et al. (2003) and Wadley (2006) reviewed the multifunctionalities and the fabrication technologies of the multifunctional periodic cellular metals with different topological structures. Hayes et al. (2004) studied the mechanical and thermal properties of linear cellular alloys with square cells, and concluded that mechanical and

heat transfer characteristics of the honeycomb materials outperformed those of open- and closed-cell metal foams with comparable relative density.

More specifically, from the viewpoint of mechanics, Wang and McDowell (2004) investigated the in-plane stiffness and yield strength of different periodic metal honeycombs, and showed that the diamond, triangular and Kagome cells have superior in-plane mechanical properties to the hexagonal, rectangular and mixed square/triangular cells. Fleck and Qiu (2007) analyzed the damage tolerance property of 2D elastic-brittle isotropic honeycombs and reported that the Kagome cells have much higher fracture toughness than those of hexagonal and triangular cells.

On the other hand, structural hierarchy in natural materials, can result in significantly higher stiffness or strength efficiencies (i.e. stiffness- or strength-to-weight ratios), compared with their single length scale microstructure counterparts, and maintain flaw-tolerance or energy-absorbing property (Lakes, 1993; Pugno, 2006; Gao, 2006; Pugno and Carpinteri, 2008; Carpinteri and Pugno, 2008; Zhao, et al., 2009). Combining the low-weight property of cellular solids and the particular functions that natural hierarchical materials display, many researchers (Fratzl and Weinkamer, 2007; Pugno and Chen, 2011; Chen and Pugno, 2011; Chen and Pugno, 2012a, b, c) have focused on the mechanical properties of the hierarchical cellular structures. Burgueno et al. (2005) studied the hierarchical cellular designs for load-bearing bio-composite beams and plates. Kooistra et al. (2007) investigated hierarchical corrugated core sandwich panels and revealed that the second-order trusses could have much higher compressive and shear strengths than their equal-mass first-order counterparts if relative densities are less than 5%. Fan et al. (2008) studied two-dimensional cellular materials made up of sandwich struts and showed that the relevant mechanical properties of the materials were improved substantially by incorporating structural hierarchy. Also, inspired by diatom algae which contains nanoporous hierarchical silicified shells, Garcia et al. (2011) revealed the toughening mechanism in the superductile wavy silica nanostructures by performing a series of molecular dynamics simulations. Taylor et al. (2011) introduced the functionally graded hierarchical honeycombs by performing a set of finite element analyses, and the results suggested that the elastic modulus of the functionally graded hierarchical honeycomb is 1.75 times that of its equal-mass first-order hexagonal honeycomb if the structure was designed properly. Different from Taylor's work, Ajdari et al. (2012) developed a new hierarchical honeycomb structure by replacing every three-edge joint

of a regular hexagonal lattice with a smaller hexagon, and showed that the elastic moduli of the hierarchical honeycombs with one level and two levels can be 2.0 and 3.5 times stiffer than their equal-mass regular hexagonal honeycomb, respectively. And more, inspired by natural materials, Chen and Pugno (2012a, b) created another 2D hierarchical honeycomb and 3D hierarchical foam and presented the corresponding theories, then applied to the natural materials.

In this chapter, following the above works, we analytically study the in-plane elastic moduli and thermal conductivity of a new multifunctional hierarchical honeycomb (MHH), which is formed by replacing the solid cell walls of an original regular hexagonal honeycomb (ORHH) with three different isotropic honeycomb sub-structures possessing hexagonal, triangular or Kagome lattices. First, we derive the analytical formulas of the effective elastic moduli of the regular hexagonal honeycombs for all densities, then, the in-plane Young's, shear and bulk moduli of the three kinds of MHH structures are calculated. Besides, the effective in-plane conductivities of the three kinds of MHH structures are formulated through the Hashin-Shtrikman upper bounds.

3.2 The effective in-plane elastic moduli of the regular hexagonal honeycombs for all densities

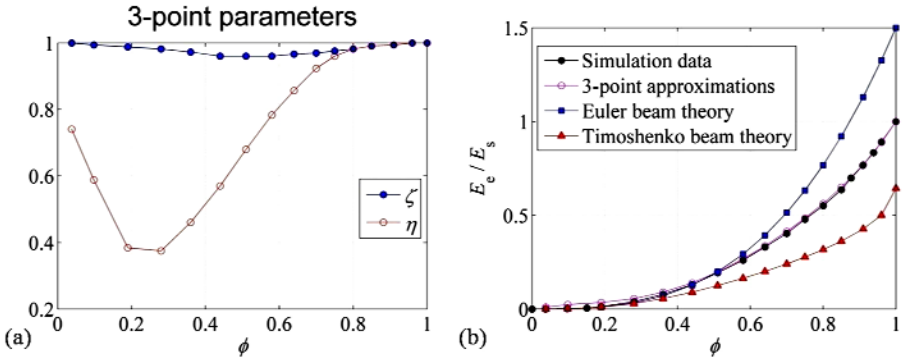

Fig. 3.1 (a) Three-point parameters ζ and η for the regular hexagonal honeycomb (Hyun and Torquato, 2000) *vs* the relative density ϕ; (b) Effective Young's modulus E_e/E_s of the regular hexagonal honeycomb *vs* the relative density ϕ predicted by different methods.

Hyun and Torquato (2000) analytically studied the effective in-plane properties of the regular hexagonal honeycomb for all densities via the three-point approximations and expressed the effective Young's modulus E_e as

$$\frac{E_e}{E_s}=\frac{\phi(2\zeta-1)(\zeta+\eta-1)}{\{3-2\phi-2(2-\phi)(1-\zeta)+(2-\zeta-\eta)[2\phi(1-\zeta)-1]\}} \tag{3.1}$$

in which ϕ is the relative density of the hexagonal honeycomb, E_s is the Young's modulus of the constituent solid, ζ and η are the three-point parameters (Fig. 3.1a). The simulation data of the effective Young's modulus E_e (Hyun and Torquato, 2000) are also provided in Fig. 3.1b. It is apparent that for the high density case (≥0.5), the three-point approximations method matches very well the simulation data, but the low density overestimates the results. In the very low density case, the overestimation is so large that the three-point approximations method is not suitable.

It is well-known that for the low-density regular hexagonal honeycombs, the Euler beam theory and the Timoshenko beam theory could be used to obtain very good analytical results for predicting elastic properties. Here, in order to get the analytical predictions for the in-plane elastic properties of the regular hexagonal honeycomb for all densities, we apply the Euler beam theory and the Timoshenko beam theory to the entire range of the relative density and compare the results with the three-point approximations. Under the Euler beam theory, Torquato et al. (1998) expressed the effective Young's modulus E_e as:

$$\frac{E_e}{E_s}=\frac{3}{2}\phi^3 \tag{3.2}$$

On the other hand, Gibson and Ashby (1997) studied the elastic properties of the low density honeycombs using the Timoshenko beam theory. For the regular hexagonal honeycombs, the effective Young's modulus is given by:

$$\frac{E_e}{E_s}=\frac{4}{\sqrt{3}}\left(\frac{t}{l}\right)^3\frac{1}{1+(5.4+1.5\nu_s)(t/l)^2} \tag{3.3}$$

in which ν_s is the Poisson's ratio of the constituent solid and $t/l=\sqrt{3}\left(1-\sqrt{1-\phi}\right)$ is

the cell-wall thickness-to-length ratio.

For honeycombs at all densities, the comparisons between the Euler beam theory, Timoshenko beam theory, three-point approximations method and the simulation data are plotted in Fig. 3.1b. We can see that when $\phi \le 0.5$ the results calculated by the Euler beam theory matches very well the simulation data, while the results are well predicted by the three-point approximations when $\phi > 0.5$. Therefore, the prediction of the effective Young's modulus of the regular hexagonal honeycombs for all densities can be expressed as:

$$\frac{E_e}{E_s} = \begin{cases} \dfrac{3}{2}\phi^3 & \phi \le 0.5 \\ \dfrac{\phi(2\zeta-1)(\zeta+\eta-1)}{\left\{3-2\phi-2(2-\phi)(1-\zeta)+(2-\zeta-\eta)\left[2\phi(1-\zeta)-1\right]\right\}} & \phi > 0.5 \end{cases} \tag{3.4}$$

Besides, through the three-point approximations, Hyun and Torquato (2000) also developed the expression for the effective in-plane bulk modulus k_e of the regular hexagonal honeycombs at all densities:

$$\frac{k_e}{k_s} = \frac{G_s\phi(2\zeta-1)}{k_s(1-\phi)+G_s\left[1+2\phi(\zeta-1)\right]} = \frac{G_s/k_s\,\phi(2\zeta-1)}{(1-\phi)+G_s/k_s\left[1+2\phi(\zeta-1)\right]} \tag{3.5}$$

where, k_s and G_s are the bulk and shear moduli of the constituent solid, respectively.

Because of the in-plane isotropic properties, k_s and E_s, k_e, G_e and E_e satisfy the following relationships:

$$k_s = \frac{E_s}{2(1-\nu_s)} \tag{3.6}$$

$$k_e = \frac{E_e}{2(1-\nu_e)} \tag{3.7}$$

$$G_e = \frac{E_e}{2(1+\nu_e)} \tag{3.8}$$

in which G_e and ν_e are the effective in-plane shear modulus and Poisson's ratio of the hexagonal honeycombs, respectively. Defining $E_e/E_s = A$ and $k_e/k_s = B$, Eqs.

(3.4)-(3.8) provide the prediction formula for G_e:

$$\frac{G_e}{E_s}=\frac{AB}{4B-2A(1-\nu_s)} \tag{3.9}$$

Then, the effective Poisson's ratio ν_e of the regular hexagonal honeycombs is derived through dividing Eq. (3.6) by Eq. (3.7):

$$\nu_e=1-\frac{A}{B}(1-\nu_s) \tag{3.10}$$

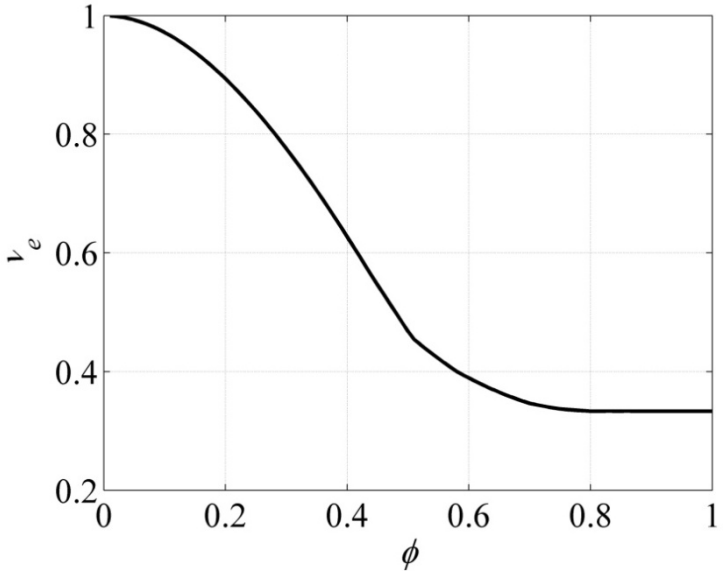

Fig. 3.2 The effective Poisson's ratio ν_e of the regular hexagonal honeycomb with $\nu_s=1/3$ *vs* the relative density ϕ.

To illustrate the correctness of the expressions of E_e, k_e and G_e, Eq. (10) is depicted in Fig. 3.2 for the honeycombs at all densities with $\nu_s=1/3$. Note that in the calculations, the three-point parameters ζ and η are interpolated from Fig. 3.1a and the relation $G_s=E_s/\left[2(1+\nu_s)\right]$ is used.

Fig. 3.2 shows excellent agreement with the existing results (see Jasiuk et al., 1994; Gibson and Ashby, 1997), that is to say, the 2D effective Poisson's ratio flows to a fixed point as the percolation threshold is reached. Here ν_e tends to 1 for the extreme low densities and tends to the Poisson's ratio of constituent solid $\nu_s=1/3$ for the

extreme high densities. This also illustrates the validations of Eqs. (3.4), (3.5) and (3.9). Here, it is worth to point out that different from the formula in Ref. Gibson and Ashby (1997), the Poisson's ratio is not a constant when the relative density is low.

3.3 MHH with isotropic hexagonal sub-structure

3.3.1 Basic theory

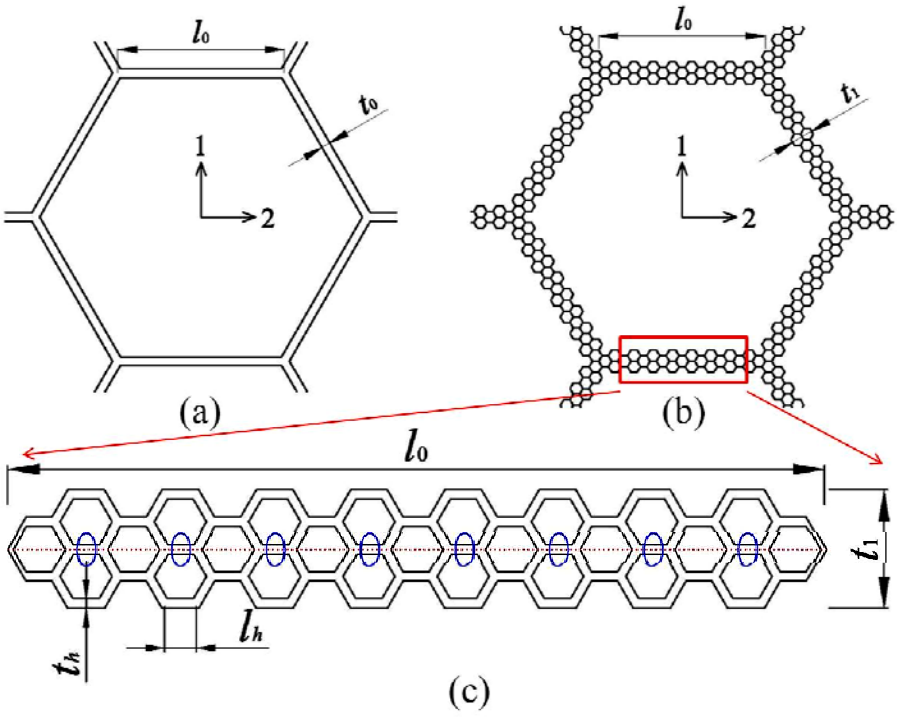

Fig. 3.3 (a) The original regular hexagonal honeycomb (ORHH); (b) the tailorable multifunctional hierarchical honeycomb (MHH) with hexagonal sub-structure; (c) amplification of a hexagonal lattice cell wall in (b) (the cell walls marked by blue circle suggest n=8 and the dash line denotes the middle line of the MHH cell wall).

First of all, we consider the MHH with isotropic hexagonal lattice sub-structure

(Fig. 3.3). Fig. 3.3a is an ORHH with the cell-wall thickness and length denoted by t_0 and l_0, respectively; Fig. 3.3b is an equal-mass MHH with the cell-wall thickness and length denoted by t_1 and l_0, respectively. We can see that the cell-wall lengths of the ORHH and the MHH are identical. In particular, one of the MHH cell walls in Fig. 3.3b is shown in Fig. 3.3c, and the cell-wall thickness and length for hexagonal cells are denoted by t_h and l_h, respectively. The out-of-plane depth is a constant and identical for both structures.

The geometry of Fig. 3.3c implies:

$$l_0 = nl_h + (n+1)(2l_h) = (3n+2)l_h \tag{3.11}$$

where, *n* is the number of the solid hexagonal cell walls lying on the middle line of the MHH cell walls (e.g., in Fig. 3.3c, *n*=8). Defining $\lambda = l_h / l_0$ as the hierarchical length ratio, then rearranging Eq. (3.11) provides,

$$\lambda = \frac{1}{3n+2} \tag{3.12}$$

Again, defining *N* as the number of hexagonal cells away from the middle line of the MHH cell walls (e.g., in Fig. 3.3c, *N*=1), and *M* the total number of half-thickness hexagonal cells in a MHH cell wall (see Fig. A in appendix A), then the relationship between *M* and *N* can be expressed as:

$$M = 2N(2n+1) + \frac{n}{3} - 4A_N \tag{3.13}$$

with $A_N = \left[(2N+1)(N-1)+1\right]/6$ (see Appendix A). Then, basing on the mass equivalence between cell walls of the MHH and the ORHH, we find $t_0 l_0 - 1/\left(2\sqrt{3}\right)t_0^2 = 6\times 1/2\left(t_h l_h - 1/\left(2\sqrt{3}\right)t_h^2\right)M$, which gives

$$\frac{t_h}{l_h} = \sqrt{3}\left[1 - \sqrt{1 - \frac{2}{3\sqrt{3}\lambda^2 M}\frac{t_0}{l_0}\left(1 - \frac{1}{2\sqrt{3}}\frac{t_0}{l_0}\right)}\right] \tag{3.14}$$

Besides, a geometrical analysis on Fig. 3.3c provides $N_{\max}$, the upper bound of N, and t_1, the thickness of the MHH cell walls：

$$N_{\max} = fl\left[\frac{1}{2\lambda}\right] = fl\left[\frac{3n+2}{2}\right] \tag{3.15}$$

$$t_1 = \begin{cases} 2N\left(\sqrt{3}l_h\right) + t_h & 1 \le N \le N_{\max} - 1 \\ 2 \times \dfrac{\sqrt{3}}{2} l_0 & N = N_{\max} \end{cases} \tag{3.16}$$

where, '*fl*[ ]' is the floor function, which denotes the largest integer not greater than the term in the brackets. Then, rearranging Eq. (3.16) gives:

$$\frac{t_1}{l_0} = \begin{cases} \left(2\sqrt{3}N + \dfrac{t_h}{l_h}\right)\lambda & 1 \le N \le N_{\max} - 1 \\ \sqrt{3} & N = N_{\max} \end{cases} \tag{3.17}$$

On the other hand, with respect to Eq. (3.14), a relation $1 - 2\Big/\left(3\sqrt{3}\lambda^2 M\right)t_0/l_0\left[1 - 1\Big/\left(2\sqrt{3}\right)t_0/l_0\right] \ge 0$ should be satisfied. Considering Eqs. (3.12) and (3.13), this relation provides $N_{\min}$, the lower bound of N:

$$N_{\min} = ce\left[\frac{3n+2-\sqrt{(3n+2)^2\left[1-\dfrac{2}{\sqrt{3}}\dfrac{t_0}{l_0}\left(1-\dfrac{1}{2\sqrt{3}}\dfrac{t_0}{l_0}\right)\right]+n}}{2}\right] \tag{3.18}$$

where, '*ce*[ ]' is the ceiling function, which denotes the smallest integer not less than the term in the brackets. Note that Eq. (3.18) may give $N_{\min} = 0$, in this case $N_{\min} = 1$.

Defining the in-plane Young's, shear and bulk moduli of the ORHH as E_O, G_O and k_O, then, from Eqs. (3.4), (3.5) and (3.9), we find:

$$\frac{E_O}{E_s} = A_O = \begin{cases} \dfrac{3}{2}\phi_O^3 & \phi_O \le 0.5 \\ \dfrac{\phi_O\left(2\zeta_O - 1\right)\left(\zeta_O + \eta_O - 1\right)}{\left\{3 - 2\phi_O - 2\left(2 - \phi_O\right)\left(1 - \zeta_O\right) + \left(2 - \zeta_O - \eta_O\right)\left[2\phi_O\left(1 - \zeta_O\right) - 1\right]\right\}} & \phi_O > 0.5 \end{cases} \tag{3.19}$$

$$\frac{k_O}{k_s} = B_O = \frac{G_s/k_s\,\phi_O\left(2\zeta_O - 1\right)}{\left(1 - \phi_O\right) + G_s/k_s\left[1 + 2\phi_O\left(\zeta_O - 1\right)\right]} \tag{3.20}$$

$$\frac{G_O}{E_s} = \frac{A_O B_O}{4B_O - 2A_O(1-\nu_s)} \tag{3.21}$$

where,

$$\phi_O = \frac{2}{\sqrt{3}}\frac{t_0}{l_0} - \frac{1}{3}\left(\frac{t_0}{l_0}\right)^2 \quad \left(\frac{t_0}{l_0} \le \sqrt{3}\right) \tag{3.22}$$

is the relative density of the ORHH, and ζ_O and η_O, interpolated from Fig. 3.1a, are the corresponding three-point parameters.

Besides, Hyun and Torquato (2000, 2002) showed that the effective thermal conductivity of the regular hexagonal honeycomb nearly approaches the H-S upper bounds. Thus, defining the thermal conductivities of the ORHH and the constituent solid as σ_O and σ_s, and using the H-S upper bounds, we approximately obtain:

$$\frac{\sigma_O}{\sigma_s} = \frac{\phi_O}{2-\phi_O} \tag{3.23}$$

Note that due to the mathematical analogy, results for the effective thermal conductivity translate immediately into equivalent results for the effective dielectric constant, electrical conductivity and magnetic permeability.

Similarly, defining the in-plane Young's, shear and bulk moduli and thermal conductivity of the hexagonal sub-structure as E_h, G_h, k_h and σ_h, we obtain:

$$\frac{E_h}{E_s} = A_h = \begin{cases} \dfrac{3}{2}\phi_h^3 & \phi_h \le 0.5 \\ \dfrac{\phi_h(2\zeta_h - 1)(\zeta_h + \eta_h - 1)}{\left\{3 - 2\phi_h - 2(2-\phi_h)(1-\zeta_h) + (2-\zeta_h-\eta_h)\left[2\phi_h(1-\zeta_h) - 1\right]\right\}} & \phi_h > 0.5 \end{cases} \tag{3.24}$$

$$\frac{k_h}{k_s} = B_h = \frac{G_s/k_s\,\phi_h(2\zeta_h - 1)}{(1-\phi_h) + G_s/k_s\left[1 + 2\phi_h(\zeta_h - 1)\right]} \tag{3.25}$$

$$\frac{G_h}{E_s} = \frac{A_h B_h}{4B_h - 2A_h(1-\nu_s)} \tag{3.26}$$

$$\frac{\sigma_h}{\sigma_s}=\frac{\phi_h}{2-\phi_h} \tag{3.27}$$

where,

$$\phi_h=\frac{2}{\sqrt{3}}\frac{t_h}{l_h}-\frac{1}{3}\left(\frac{t_h}{l_h}\right)^2 \quad \left(\frac{t_h}{l_h}\le\sqrt{3}\right) \tag{3.28}$$

is the relative density of the hexagonal sub-structure, and ζ_h and η_h, interpolated from Fig. 3.1a, are the corresponding three-point parameters. Denoting the effective Poisson's ratio of the hexagonal sub-structure by ν_h, the relation $G_h=E_h/\left[2(1+\nu_h)\right]$ is satisfied. Then, combining Eqs. (3.24) and (3.26) gives,

$$\nu_h=1-\frac{A_h}{B_h}(1-\nu_s) \tag{3.29}$$

Thus,

$$\frac{G_h}{k_h}=\frac{E_h/\left[2\left(1+\nu_h\right)\right]}{E_h/\left[2\left(1-\nu_h\right)\right]}=\frac{1-\nu_h}{1+\nu_h}=\frac{A_h(1-\nu_s)}{2B_h-A_h(1-\nu_s)} \tag{3.30}$$

At the same time, by treating the hexagonal sub-structure as a continuum and defining the in-plane Young's, shear and bulk moduli and thermal conductivity of the MHH as E_M, G_M, k_M and σ_M, it is easily to obtain:

$$\frac{E_M}{E_h}=A_M=\begin{cases}\dfrac{3}{2}\phi_M^3 & \phi_M\le 0.5\\ \dfrac{\phi_M\left(2\zeta_M-1\right)\left(\zeta_M+\eta_M-1\right)}{\left\{3-2\phi_M-2\left(2-\phi_M\right)\left(1-\zeta_M\right)+\left(2-\zeta_M-\eta_M\right)\left[2\phi_M\left(1-\zeta_M\right)-1\right]\right\}} & \phi_M>0.5\end{cases} \tag{3.31}$$

$$\frac{k_M}{k_h}=B_M=\frac{G_h/k_h\,\phi_M\left(2\zeta_M-1\right)}{\left(1-\phi_M\right)+G_h/k_h\left[1+2\phi_M\left(\zeta_M-1\right)\right]} \tag{3.32}$$

$$\frac{G_M}{E_h}=\frac{A_M B_M}{4B_M-2A_M\left(1-\nu_h\right)} \tag{3.33}$$

$$\frac{\sigma_M}{\sigma_h}=\frac{\phi_M}{2-\phi_M} \tag{3.34}$$

where,

$$\phi_M=\frac{2}{\sqrt{3}}\frac{t_1}{l_0}-\frac{1}{3}\left(\frac{t_1}{l_0}\right)^2 \quad \left(\frac{t_1}{l_0}\le\sqrt{3}\right) \tag{3.35}$$

and ζ_M and η_M , interpolated from Fig. 3.1a, are the three-point parameters corresponding to ϕ_M .

Combining Eqs. (3.19), (3.24) and (3.31) gives the relative Young's modulus E_M/E_O :

$$\frac{E_M}{E_O}=\frac{A_M A_h}{A_O} \tag{3.36}$$

Similarly, from Eqs. (3.20), (3.25) and (3.32), we can get the relative in plane bulk modulus k_M/k_O :

$$\frac{k_M}{k_O}=\frac{B_M B_h}{B_O} \tag{3.37}$$

And from Eqs. (3.21), (3.24) and (3.33), we obtain the relative shear modulus G_M/G_O :

$$\frac{G_M}{G_O}=\frac{A_M B_M A_h}{2B_M-A_M(1-\nu_h)}\frac{2B_O-A_O(1-\nu_s)}{A_O B_O} \tag{3.38}$$

Finally, from Eqs. (3.23), (3.27) and (3.34), we get the relative thermal conductivity σ_M/σ_O :

$$\frac{\sigma_M}{\sigma_O}=\frac{\phi_M\phi_h(2-\phi_O)}{\phi_O(2-\phi_M)(2-\phi_h)} \tag{3.39}$$

3.3.2 Effect of N on the relative elastic moduli and thermal conductivity of the MHH with hexagonal sub-structure

To investigate the influence of N on the relative elastic properties E_M/E_O , G_M/G_O , k_M/k_O and the relative thermal conductivity σ_M/σ_O , here, we discuss the

following examples with parameters $n=16$, $\lambda=1/(3n+2)=0.02$ and $t_0/l_0=0.01$, 0.05, 0.1, 0.2 and 0.3. Then, we can find $N_{\max}=25$ through Eq. (3.15), and $N_{\min}$ for each t_0/l_0 through Eq. (3.18). The results of the relative elastic properties E_M/E_O and G_M/G_O, k_M/k_O and the relative thermal conductivity σ_M/σ_O versus N are reported in Figs. 3.4-3.6, respectively.

From Figs. 3.4a, b, we can see that for all the t_0/l_0 ratios considered, the optimal E_M/E_O and G_M/G_O, which vary between 1 and 2, exist as N increases. Note that the optimal E_M/E_O and G_M/G_O may do not correspond to the same N. The reason is that E_O/E_s and E_M/E_h are independent of the Poisson's ratios ν_s and ν_h but G_O/G_s and G_M/G_h are dependent on them (Hyun and Torquato, 2000).

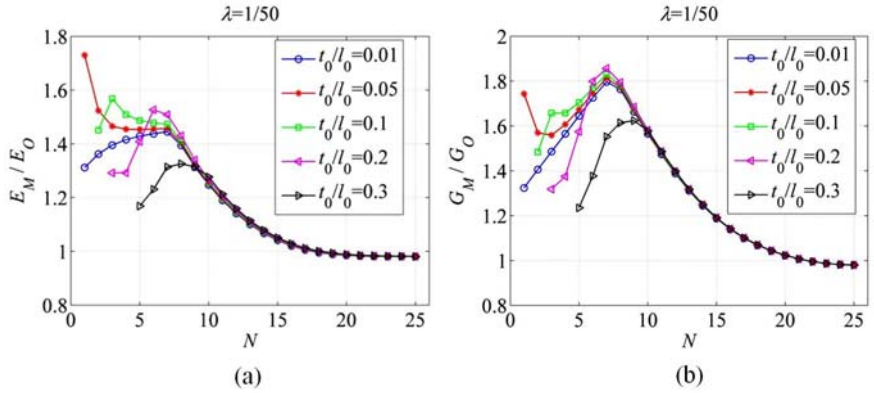

Fig. 3.4 (a) The relative Young's modulus E_M/E_O *vs* N for different t_0/l_0; (b) The relative shear modulus G_M/G_O *vs* N for different t_0/l_0.

Figs. 3.5 and 3.6 show that the relative bulk modulus k_M/k_O and the relative thermal conductivity σ_M/σ_O increase with the increasing t_0/l_0, but they are generally less than 1 for all the t_0/l_0 ratios considered. This means that the effective bulk modulus and thermal conductivity of the MHH with regular hexagonal sub-structure are smaller than those of the ORHH structure. Of particular interest, there is an optimal value for the thermal conductivity, and this could be used to design low heat conductivity materials with an optimal topology.

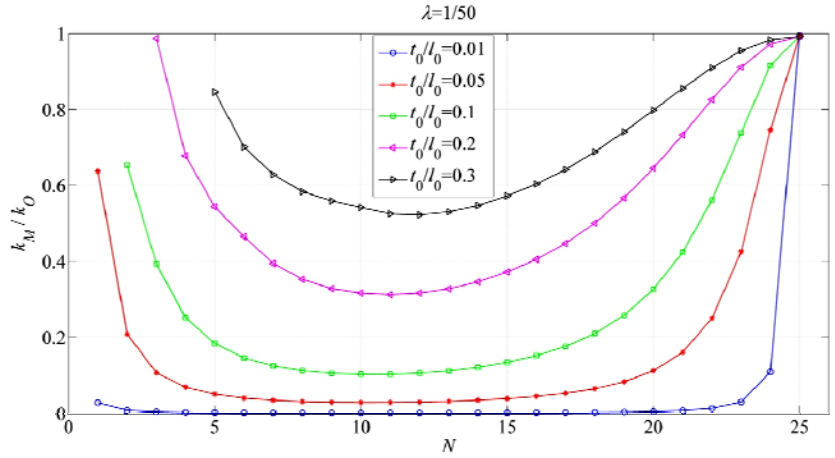

Fig. 3.5 The relative bulk modulus G_M/G_O *vs* N for different t_0 / l_0

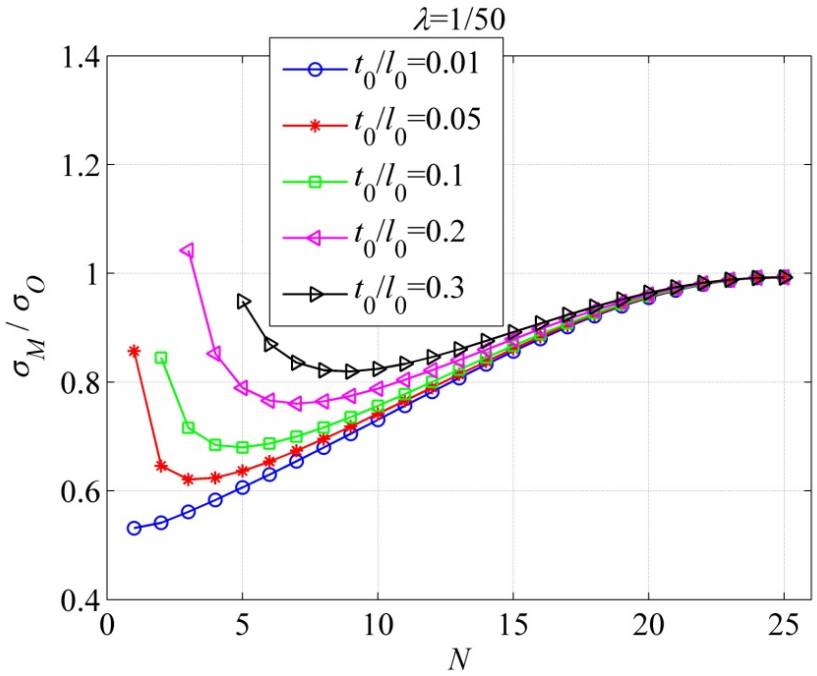

Fig. 3.6 The relative thermal conductivity G_M/G_O *vs* N for different t_0 / l_0 .

3.3.3 The effects of t_0/l_0 — the cell-wall thickness-to-length ratio of the ORHH

To investigate the effects of the cell-wall thickness-to-length ratio t_0/l_0 of the ORHH on the relative elastic properties and thermal conductivity of the MHH structure, again, we use the examples in Section 3.2 and we maintain $n=16$, $\lambda=0.02$ but change t_0/l_0 from 0.01 to 0.5 with incremental 0.01. In fact, under the same N, the value of G_M/G_O is in general weakly larger than E_M/E_O (Fig. 3.4a, b), so here we only consider the relative Young's modulus E_M/E_O against t_0/l_0. At the same time, σ_M/σ_O and k_M/k_O generally are smaller than 1 for all t_0/l_0 as shown in Figs. 3.5 and 3.6, thus, the discussion will not be treated in this section.

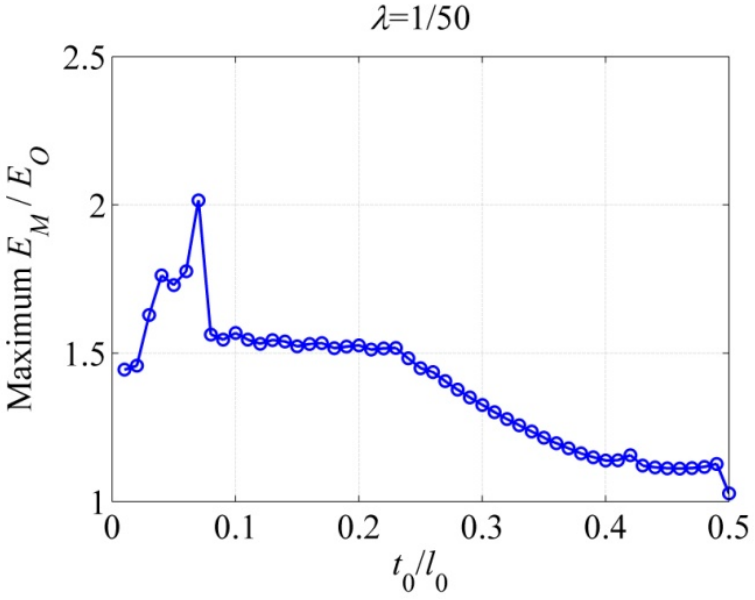

Fig. 3.7 The maximum E_M/E_O vs t_0/l_0

The analytical results are reported in Fig. 3.7. We can see that the maximum E_M/E_O increases before t_0/l_0 reaches 0.07 but after that it decreases. That is to say,

the optimal E_M/E_O of the MHH with hexagonal sub-structure exists at $t_0/l_0 = 0.07$, of which the value approximately equals 2. This result is comparable to the finite element result given by Taylor et al. (2011).

3.4 MHH with triangular sub-structure

3.4.1 Basic theory

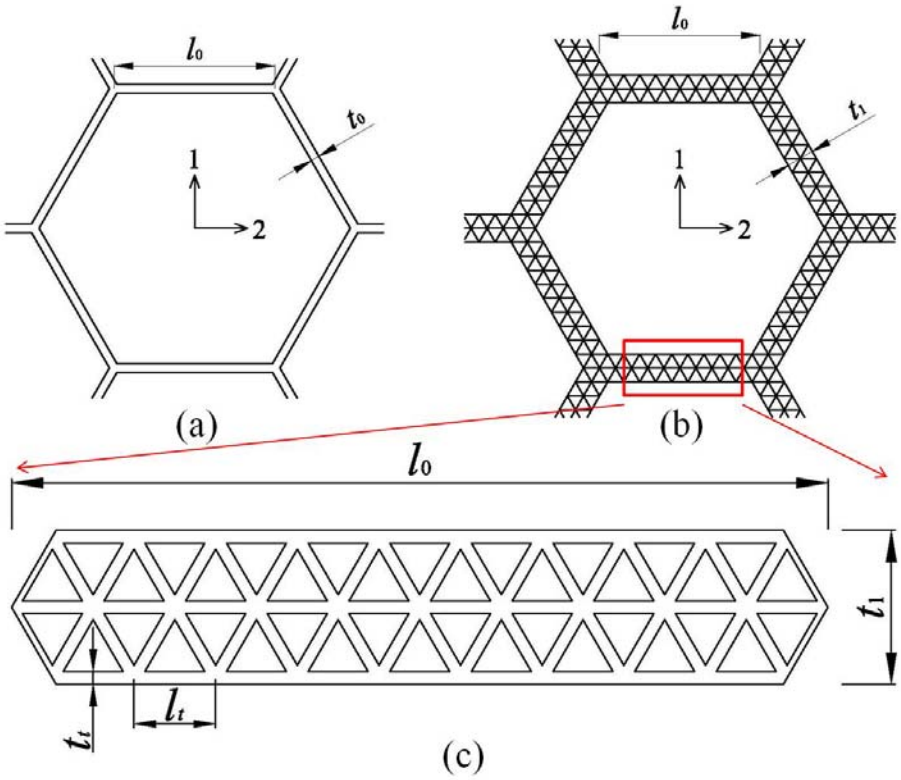

Fig. 3.8 Schematics of (a) the ORHH; (b) the tailorable MHH with triangular sub-structure; (c) amplification of a trianglar lattice cell wall in (b).

In this section, we substitute the ORHH cell walls with the equal-mass isotropic triangular sub-structure, see Fig. 3.8. As defined in Section 3, the hierarchical length

ratio is expressed as,

$$\lambda = \frac{l_t}{l_0} = \frac{1}{n} \quad (n \geq 1) \tag{3.40}$$

where, n is the number of solid triangular lattice cell walls lying on the middle line of the MHH cell walls. From Fig. 3.8c, according to the equal-mass principle, we can find $t_0 l_0 - \frac{1}{2\sqrt{3}} t_0^2 = 3 \times \frac{1}{2}\left(t_t l_t - \frac{\sqrt{3}}{2} t_t^2 \right) M$, which gives

$$\frac{t_t}{l_t} = \frac{1}{\sqrt{3}}\left[1 - \sqrt{1 - \frac{4\sqrt{3}}{3\lambda^2 M} \frac{t_0}{l_0}\left(1 - \frac{1}{2\sqrt{3}} \frac{t_0}{l_0} \right)} \right] \tag{3.41}$$

where, M is the total number of half thickness triangular lattice cells in a MHH cell wall and M has the following relationship with n and N (see Appendix B):

$$M = 2N(2n - N) + \frac{2}{3}(n - N) \quad (1 \leq N \leq n) \tag{3.42}$$

in which N is the number of triangular lattice cells away from the middle line of the MHH cell walls. Similarly as that in Section 3, a geometrical analysis on Fig. 3.8c provides $N_{\max}$, the upper bound of N , and t_1 , the thickness of the MHH cell walls:

$$N_{\max} = n \tag{3.43}$$

$$t_1 = \begin{cases} 2N\left(\frac{\sqrt{3}}{2} l_t \right) + t_t & 1 \leq N \leq N_{\max} - 1 \\ 2 \times \frac{\sqrt{3}}{2} l_0 & N = N_{\max} \end{cases} \tag{3.44}$$

Then, rearranging Eq. (3.44) gives,

$$\frac{t_1}{l_0} = \begin{cases} \left(\sqrt{3} N + \frac{t_t}{l_t} \right) \lambda & 1 \leq N \leq N_{\max} - 1 \\ \sqrt{3} & N = N_{\max} \end{cases} \tag{3.45}$$

On the other hand, with respect to Eq. (3.41), the relation $1 - 4\sqrt{3} / \left(3\lambda^2 M \right) t_0 / l_0 \left[1 - 1 / \left(2\sqrt{3} \right) t_0 / l_0 \right] \geq 0$ should be satisfied. In conjunction with Eqs. (3.40) and (3.42), this relation gives $N_{\min}$, the lower bound of N :

$$N_{\min} = ce\left[\frac{6n-1-\sqrt{(6n-1)^2-12n\left[2\sqrt{3}n\frac{t_0}{l_0}\left(1-\frac{1}{2\sqrt{3}}\frac{t_0}{l_0}\right)-1\right]}}{6}\right] \tag{3.46}$$

Note that Eq. (3.46) may give $N_{\min}=0$, in this case $N_{\min}=1$.

Like the discussion in Section 3, we would like to analyze the effective elastic properties and thermal conductivity of the triangular lattice sub-structure. As already mentioned in the introduction, Hyun and Torquato (2002) showed that for the triangular and Kagome honeycombs, both the in-plane effective moduli and conductivity (or dielectric constant) are approaching the H-S upper bounds (Hashin and Shtrikman, 1962; Hashin and Shtrikman, 1963). So, we approximately use the H-S upper bounds to calculate the effective elastic moduli and thermal conductivity of the triangular lattice sub-structure. Defining the in-plane Young's, shear and bulk moduli and thermal conductivity of the triangular sub-structure as E_t, G_t, k_t and σ_t, we obtain:

$$\frac{E_t}{E_s}=A_t=\frac{\phi_t}{3-2\phi_t} \tag{3.47}$$

$$\frac{k_t}{k_s}=B_t=\frac{\phi_t G_s/k_s}{1-\phi_t+G_s/k_s} \tag{3.48}$$

$$\frac{G_t}{E_s}=C_t=\frac{1}{2(1+\nu_s)}\frac{\phi_t}{(1-\phi_t)(1+2G_s/k_s)+1} \tag{3.49}$$

$$\frac{\sigma_t}{\sigma_s}=\frac{\phi_t}{2-\phi_t} \tag{3.50}$$

where,

$$\phi_t=2\sqrt{3}\frac{t_t}{l_t}-3\left(\frac{t_t}{l_t}\right)^2 \quad \left(\frac{t_t}{l_t}\le\frac{1}{\sqrt{3}}\right) \tag{3.51}$$

is the relative density of the triangular sub-structure. Denoting the effective Poisson's ratio of the triangular sub-structure by ν_t, the relation $G_t=E_t/[2(1+\nu_t)]$ holds. Then, combining Eqs. (3.47) and (3.49) gives,

$$\nu_t = \frac{1}{2}\frac{A_t}{C_t} - 1 \tag{3.52}$$

Thus,

$$\frac{G_t}{k_t} = \frac{E_t/\left[2\left(1+\nu_t\right)\right]}{E_t/\left[2\left(1-\nu_t\right)\right]} = \frac{1-\nu_t}{1+\nu_t} = 4\frac{C_t}{A_t} - 1 \tag{3.53}$$

At the same time, by treating the triangular sub-structure as a continuum and defining the in-plane Young's, shear and bulk moduli and thermal conductivity of the MHH with triangular sub-structure as E_M, G_M, k_M and σ_M, we have:

$$\frac{E_M}{E_t} = A_M = \begin{cases} \dfrac{3}{2}\phi_M^3 & \phi_M \le 0.5 \\ \dfrac{\phi_M\left(2\zeta_M - 1\right)\left(\zeta_M + \eta_M - 1\right)}{\left\{3 - 2\phi_M - 2\left(2-\phi_M\right)\left(1-\zeta_M\right) + \left(2-\zeta_M-\eta_M\right)\left[2\phi_M\left(1-\zeta_M\right)-1\right]\right\}} & \phi_M > 0.5 \end{cases} \tag{3.54}$$

$$\frac{k_M}{k_t} = B_M = \frac{G_t/k_t\,\phi_M\left(2\zeta_M - 1\right)}{\left(1-\phi_M\right) + G_t/k_t\left[1 + 2\phi_M\left(\zeta_M - 1\right)\right]} \tag{3.55}$$

$$\frac{G_M}{E_t} = \frac{A_M B_M}{4B_M - 2A_M\left(1-\nu_t\right)} \tag{3.56}$$

$$\frac{\sigma_M}{\sigma_t} = \frac{\phi_M}{2-\phi_M} \tag{3.57}$$

where,

$$\phi_M = \frac{2}{\sqrt{3}}\frac{t_1}{l_0} - \frac{1}{3}\left(\frac{t_1}{l_0}\right)^2 \quad \left(\frac{t_1}{l_0} \le \sqrt{3}\right) \tag{3.58}$$

and ζ_M and η_M, interpolated from Fig. 3.1a, are the three-point parameters corresponding to ϕ_M.

Combining Eqs. (3.19), (3.47) and (3.54) gives the relative Young's modulus E_M/E_O:

$$\frac{E_M}{E_O} = \frac{A_M A_t}{A_O} \tag{3.59}$$

Similarly, from Eqs. (3.20), (3.48) and (3.55), we can find the relative bulk modulus k_M/k_O :

$$\frac{k_M}{k_O}=\frac{B_M B_t}{B_O} \tag{3.60}$$

And from Eqs. (3.21), (3.47) and (3.56), we obtain the relative shear modulus G_M/G_O :

$$\frac{G_M}{G_O}=\frac{A_M B_M A_t}{2B_M-A_M(1-\nu_t)}\frac{2B_O-A_O(1-\nu_s)}{A_O B_O} \tag{3.61}$$

Finally, from Eqs. (3.23), (3.50) and (3.57), the relative thermal conductivity σ_M/σ_O is derived:

$$\frac{\sigma_M}{\sigma_O}=\frac{\phi_M\phi_t(2-\phi_O)}{\phi_O(2-\phi_M)(2-\phi_t)} \tag{3.62}$$

3.4.2 Effects of N on the relative elastic moduli and thermal conductivity of the MHH with triangular sub-structure

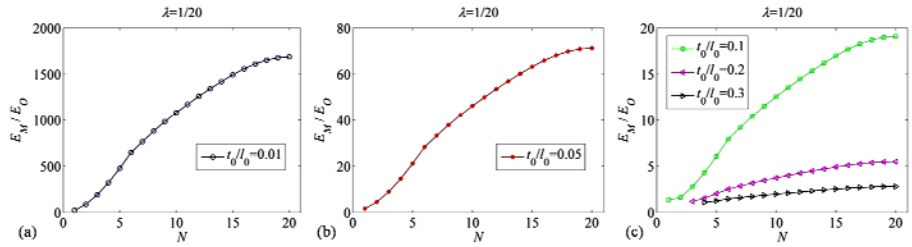

Fig. 3.9 The relative Young's modulus E_M/E_O *vs* N for different t_0/l_0 : (a) $t_0/l_0=0.01$; (b) $t_0/l_0=0.05$; (c) $t_0/l_0=0.1, 0.2, 0.3$.

As discussed in Section 3, the influence of N on the effective elastic properties and thermal conductivity of the MHH with triangular sub-structure are studied, here we consider other examples with parameters $n=20$, $\lambda=1/n=0.05$, $t_0/l_0=0.01$, 0.05, 0.1,

0.2 and 0.3. Then, we immediately obtain $N_{\max}=20$ by Eq. (3.23) and the lower bounds $N_{\min}$ for each t_0/l_0 by Eq. (3.46). The results of the relative elastic moduli E_M/E_O, G_M/G_O, k_M/k_O and the relative thermal conductivity σ_M/σ_O versus N are reported in Figs. 3.9-3.12, respectively.

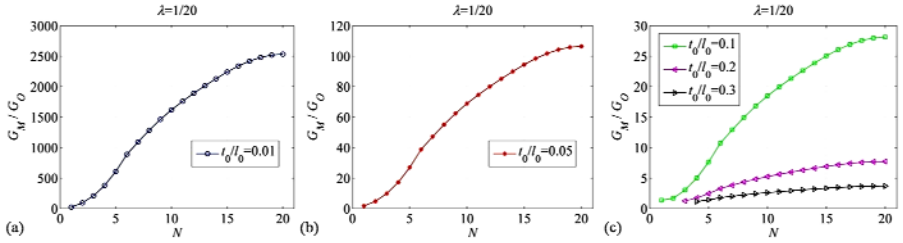

Fig. 3.10 The relative Young's modulus G_M/G_O *vs* N for different t_0/l_0 : (a) $t_0/l_0=0.01$; (b) $t_0/l_0=0.05$; (c) $t_0/l_0=0.1, 0.2, 0.3$.

From Figs. 3.9 and 3.10, we can also see that the relative Young's modulus E_M/E_O and the effective shear modulus G_M/G_O increase with the increase of N, and the thickness-to-length ratio t_0/l_0 has a strong influence on them. With respect to its equal-mass ORHH, the enhancements of the relative Young's and shear moduli of the MHH with triangular sub-structure can be 1 (Figs. 3.9c and 3.10c) or even 3 orders of magnitude(Figs. 3.9a and 3.10a). Although the enhancement on Young's modulus of the MHH with triangular sub-structure decreases with the increase of t_0/l_0, for a relatively small t_0/l_0 (less than 0.3), its stiffening effect (Figs. 3.9 and 3.10) by the triangular sub-structure is much larger than that of the hexagonal sub-structure (Figs. 3.4a, b).

The relative bulk modulus k_M/k_O and the relative thermal conductivity σ_M/σ_O shown in Figs. 3.11 and 3.12 have the same varying trends with those of the MHH with hexagonal sub-structure reported in Section 3.2. The discussion is the same as before.

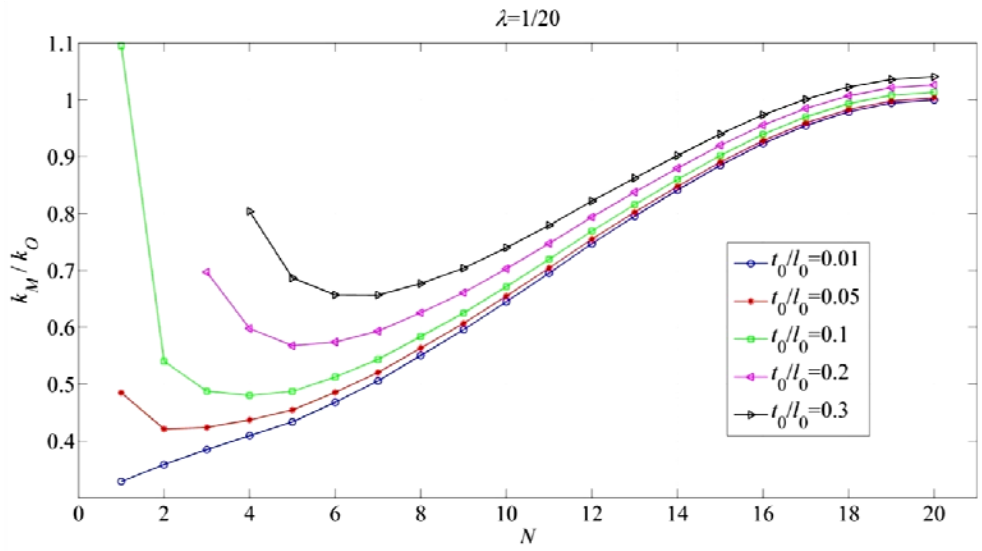

Fig. 3.11 The relative bulk modulus k_M/k_O *vs* N for different t_0 / l_0

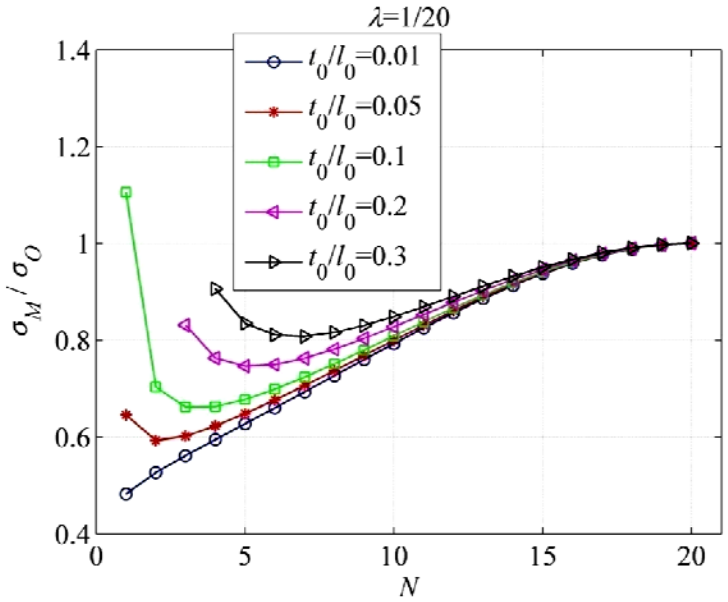

Fig. 3.12 The relative thermal conductivity σ_M/σ_O *vs* N for different t_0 / l_0

3.5 MHH with isotropic Kagome sub-structure

3.5.1 Basic theory

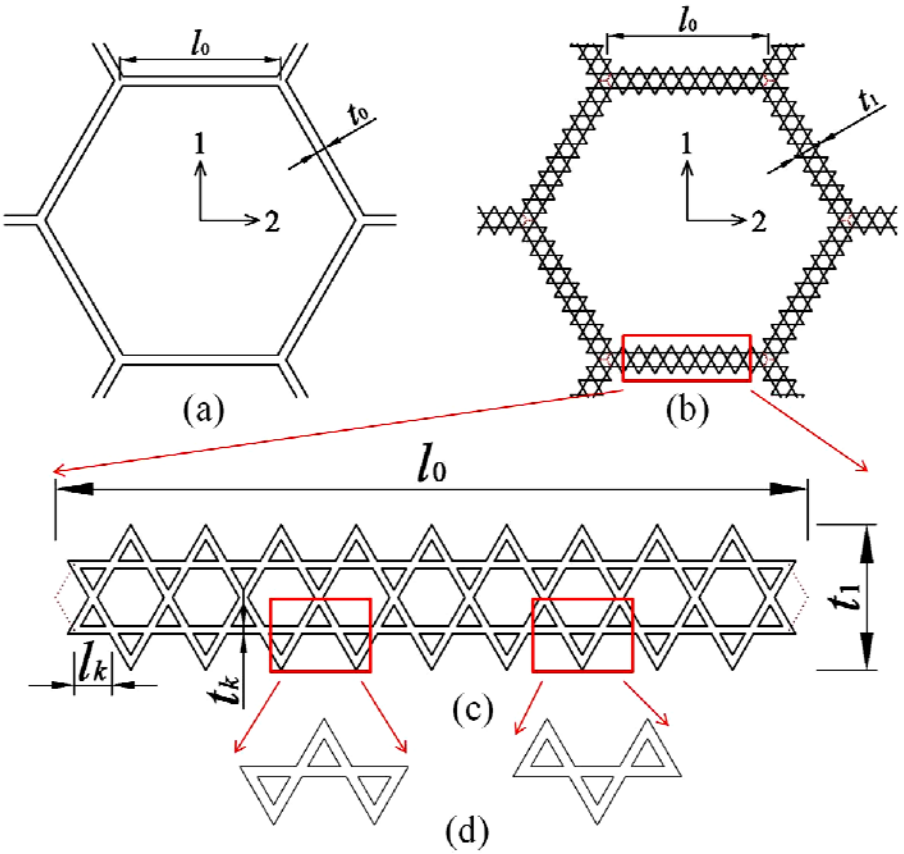

Fig. 3.13 Schematics of (a) the ORHH; (b) the tailorable MHH with Kagome sub-structure (in this thesis the red dashline is for the convenience of linear dimension); (c) amplication of a Kagome sub-structure cell wall in (b); (d)the representative cells for the Kagome honeycomb.

Kagome honeycomb has been revealed to have pronounced higher fracture toughness (Fleck and Qiu, 2007) and better thermal-mechanical performance than the triangular honeycombs (Wang et al., 2007). Therefore, in this Section, we will consider

the third topology of the MHH, namely, substituting the ORHH cell walls with their equal-mass Kagome sub-structure (Fig. 3.13), and study its effective elastic properties and thermal conductivity. In this case, the hierarchical length ratio is expressed as:

$$\lambda = \frac{l_k}{l_0} = \frac{1}{n} \quad n = 4,\ 6,\ 8,\ 10\ \cdots \tag{3.63}$$

where, l_k is the side length of triangles in Kagome cells and n is the number of sides of the effective triangles on the middle line of the MHH cell walls. As discussed before, here, the equal-mass principle provides $t_0 l_0 - 1/\left(2\sqrt{3}\right) t_0^2 = 3 \times \left(t_k l_k - \sqrt{3}/2 t_k^2\right) M$, and t_k / l_k is derived as:

$$\frac{t_k}{l_k} = \frac{1}{\sqrt{3}} \left[1 - \sqrt{1 - \frac{2\sqrt{3}}{3\lambda^2 M} \frac{t_0}{l_0} \left(1 - \frac{1}{2\sqrt{3}} \frac{t_0}{l_0} \right)} \right] \tag{3.64}$$

where, M is the total number of triangles in a MHH cell wall, and it is expressed with n and N as (see Appendix C):

$$M = 2N\left(n - N\right) \quad \left(1 \le N \le \frac{n}{2}\right) \tag{3.65}$$

where, N is the number of the Kagome representative cells (e.g., in Fig. 3.13c, $N = 1$) away from the middle line of the MHH cell walls. Similarly to that in Sections 3 and 4, a geometrical analysis on Fig. 3.13c provides $N_{\max}$, the upper bound of N, and t_1, the thickness of the MHH cell walls:

$$N_{\max} = \frac{n}{2} \tag{3.66}$$

$$t_1 = \begin{cases} 2N\left(\sqrt{3} l_k\right) + 2t_k & 1 \le N \le N_{\max} - 1 \\ 2 \times \dfrac{\sqrt{3}}{2} l_0 & N = N_{\max} \end{cases} \tag{3.67}$$

Then, rearranging Eq. (3.67) gives

$$\frac{t_1}{l_0} = \begin{cases} 2\left(\sqrt{3}N + \dfrac{t_k}{l_k}\right)\lambda & 1 \le N \le N_{\max} - 1 \\ \sqrt{3} & N = N_{\max} \end{cases} \tag{3.68}$$

On the other hand, with respect to Eq. (3.64), the relation $1-2\sqrt{3}\Big/\left(3\lambda^2 M\right)t_0/l_0\left[1-1\Big/\left(2\sqrt{3}\right)t_0/l_0\right]\geq 0$ holds. In conjunction with Eqs. (3.63) and (3.65), this relation gives $N_{\min}$, the lower bound of N:

$$N_{\min}=ce\left[\frac{n-n\sqrt{1-\dfrac{4\sqrt{3}}{3}\dfrac{t_0}{l_0}\left(1-\dfrac{1}{2\sqrt{3}}\dfrac{t_0}{l_0}\right)}}{2}\right] \tag{3.69}$$

Also, it should be note that Eq. (3.69) may give $N_{\min}=0$, for this case $N_{\min}=1$.

Here, we again approximately use the H-S upper bounds to analyze the effective elastic properties and thermal conductivity of the Kagome lattice sub-structure. Defining the in-plane Young's, shear and bulk moduli and thermal conductivity of the Kagome sub-structure as E_k, G_k, k_k and σ_k, we obtain:

$$\frac{E_k}{E_s}=A_k=\frac{\phi_k}{3-2\phi_k} \tag{3.70}$$

$$\frac{k_k}{k_s}=B_k=\frac{\phi_k\, G_s/k_s}{1-\phi_k+G_s/k_s} \tag{3.71}$$

$$\frac{G_k}{E_s}=C_k=\frac{1}{2\left(1+\nu_s\right)}\frac{\phi_k}{\left(1-\phi_k\right)\left(1+2\,G_s/k_s\right)+1} \tag{3.72}$$

$$\frac{\sigma_k}{\sigma_s}=\frac{\phi_k}{2-\phi_k} \tag{3.73}$$

where,

$$\phi_k=\sqrt{3}\frac{t_k}{l_k}-\left(\frac{t_k}{l_k}\right)^2\quad\left(\frac{t_k}{l_k}\leq\frac{1}{\sqrt{3}}\right) \tag{3.74}$$

is the relative density of the Kagome sub-structure. Denoting the effective Poisson's ratio of the Kagome sub-structure by ν_k, employing $G_k=E_k/\left[2(1+\nu_k)\right]$ and combining Eqs. (3.70) and (3.72) give

$$\nu_k=\frac{1}{2}\frac{A_k}{C_k}-1 \tag{3.75}$$

Thus,

$$\frac{G_k}{k_k}=\frac{E_k/\left[2\left(1+\nu_k\right)\right]}{E_k/\left[2\left(1-\nu_k\right)\right]}=\frac{1-\nu_k}{1+\nu_k}=4\frac{C_k}{A_k}-1 \tag{3.76}$$

Again, by treating the Kagome sub-structure as a continuum and defining the in-plane Young's, shear and bulk moduli and thermal conductivity of the MHH with Kagome sub-structure as E_M, G_M, k_M and σ_M, we have:

$$\frac{E_M}{E_k}=A_M=\begin{cases}\dfrac{3}{2}\phi_M^3 & \phi_M\le 0.5\\ \dfrac{\phi_M\left(2\zeta_M-1\right)\left(\zeta_M+\eta_M-1\right)}{\left\{3-2\phi_M-2\left(2-\phi_M\right)\left(1-\zeta_M\right)+\left(2-\zeta_M-\eta_M\right)\left[2\phi_M\left(1-\zeta_M\right)-1\right]\right\}} & \phi_M>0.5\end{cases} \tag{3.77}$$

$$\frac{k_M}{k_k}=B_M=\frac{G_k/k_k\,\phi_M\left(2\zeta_M-1\right)}{\left(1-\phi_M\right)+G_k/k_k\left[1+2\phi_M\left(\zeta_M-1\right)\right]} \tag{3.78}$$

$$\frac{G_M}{E_k}=\frac{A_M B_M}{4B_M-2A_M\left(1-\nu_k\right)} \tag{3.79}$$

$$\frac{\sigma_M}{\sigma_k}=\frac{\phi_M}{2-\phi_M} \tag{3.80}$$

where,

$$\phi_M=\frac{2}{\sqrt{3}}\frac{t_1}{l_0}-\frac{1}{3}\left(\frac{t_1}{l_0}\right)^2\quad\left(\frac{t_1}{l_0}\le\sqrt{3}\right) \tag{3.81}$$

and ζ_M and η_M interpolated from Fig. 3.1a are the three-point parameters corresponding to ϕ_M.

Combining Eqs. (3.19), (3.70) and (3.77) gives the relative Young's modulus E_M/E_O:

$$\frac{E_M}{E_O}=\frac{A_M A_k}{A_O} \tag{3.82}$$

Similarly, from Eqs. (3.20), (3.71) and (3.78) we can get the relative bulk modulus k_M/k_O:

$$\frac{k_M}{k_O}=\frac{B_M B_k}{B_O} \tag{3.83}$$

And from Eqs. (3.21), (3.70) and (3.79) we obtain the relative shear modulus G_M/G_O :

$$\frac{G_M}{G_O}=\frac{A_M B_M A_k}{2B_M-A_M(1-\nu_k)}\frac{2B_O-A_O(1-\nu_s)}{A_O B_O} \tag{3.84}$$

Finally, from Eqs. (3.23), (3.50) and (3.57), we find the relative thermal conductivity σ_M/σ_O :

$$\frac{\sigma_M}{\sigma_O}=\frac{\phi_M\phi_k(2-\phi_O)}{\phi_O(2-\phi_M)(2-\phi_k)} \tag{3.85}$$

3.5.2 Effects of N on the relative elastic moduli and thermal conductivity of the MHH with Kagome sub-structure

In this section, we consider the examples with parameters $n=20$, $\lambda=1/n=0.05$, $t_0/l_0=0.01$, 0.05, 0.1, 0.2 and 0.3. Then, Eq. (3.66) provides $N_{\max}=10$ and Eq. (3.69) the lower bound $N_{\min}$ for each t_0/l_0 . The results of the relative elastic moduli E_M/E_O , G_M/G_O , k_M/k_O and the relative thermal conductivity σ_M/σ_O versus N are shown in Figs. 3.14-17, respectively.

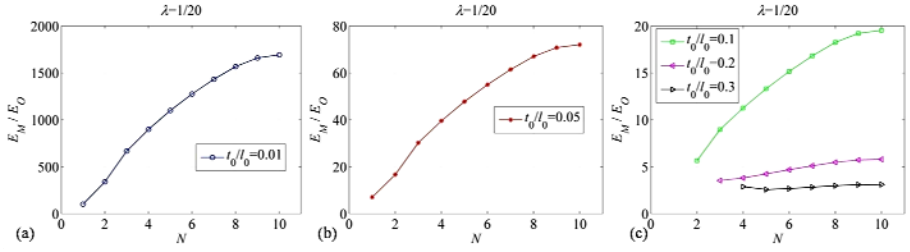

Fig. 3.14 The relative Young's modulus E_M/E_O *vs* N for different t_0/l_0 : (a) $t_0/l_0=0.01$; (b) $t_0/l_0=0.05$; (c) $t_0/l_0=0.1$, 0.2, 0.3 .

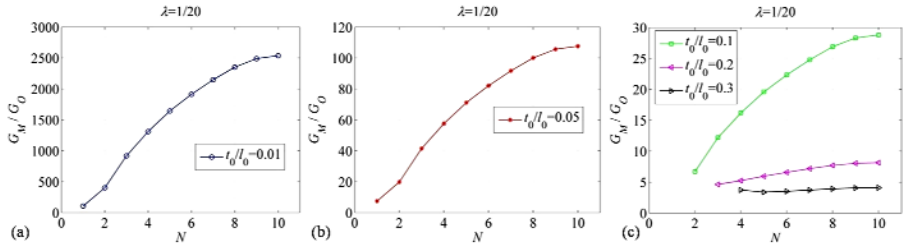

Fig. 3.15 The relative shear modulus G_M/G_O *vs* N for different t_0/l_0 : (a) $t_0/l_0 = 0.01$; (b) $t_0/l_0 = 0.05$; (c) $t_0/l_0 = 0.1, 0.2, 0.3$.

Comparing Figs. 3.14 and 3.15 with Figs. 3.9 and 3.10, we can see that the Young's and shear moduli of the MHH with Kagome sub-structure are similar to that of the MHH with triangular sub-structure, so the discussion is the same as before.

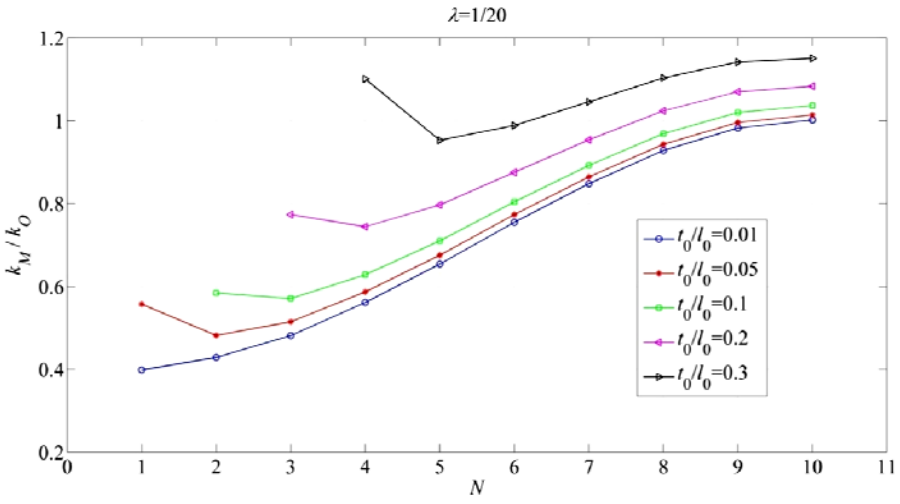

Fig. 3.16 The relative bulk modulus k_M/k_O *vs* N for different t_0/l_0

However, it is worth to say that, different from the MHH with hexagonal and triangular sub-structures, the relative bulk modulus k_M/k_O and the relative thermal conductivity σ_M/σ_O of the MHH with Kagome sub-structure become larger than 1 with the increase of t_0/l_0 (Figs. 3.16 and 3.17). This is to say, when t_0/l_0 is large enough, the effective bulk modulus and thermal conductivity of the MHH with

Kagome sub-structure could be greater than those of the ORHH structures.

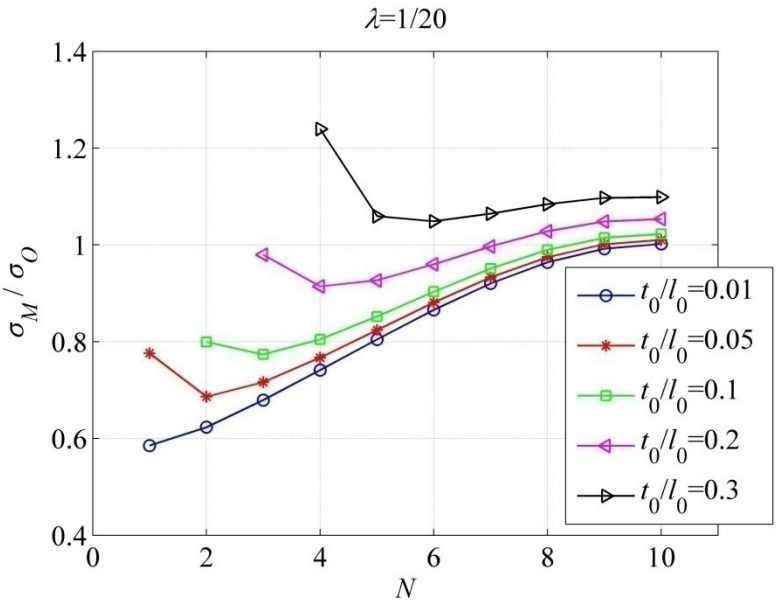

Fig. 3.17 The relative thermal conductivity σ_M/σ_O *vs* N for different t_0/l_0

3.6 Comparisons of hexagonal, triangular and Kagome sub-structures

Comparing the examples discussed in Sections 3 to 5, it is apparent that for an identical ORHH, the in-plane stiffness enhancements of the MHH with triangular and Kagome sub-structures could be much greater than that with the hexagonal sub-structure. To illustrate this point clearly, one more example with the parameters $t_0/l_0 = 0.1$ and $\lambda = 1/20$ is analyzed, and the result is plotted in Fig. 3.18, in which the relative Young's modulus E_M/E_O against N for the MHH with the above three sub-structures are depicted. Interestingly, we find that the relative Young's moduli of the MHH with triangular and Kagome sub-structures increase as N increases, but it is inverse for the MHH with hexagonal sub-structure, and more, the Young's modulus of

the MHH with Kagome sub-structure is improved most with respect to the ORHH.

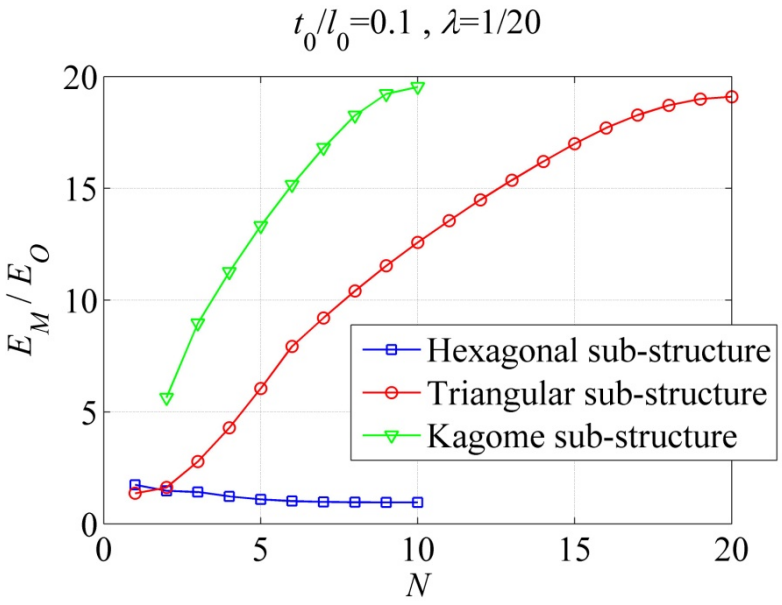

Fig. 3.18 The relative Young's modulus E_M/E_O *vs* N for different sub-structures with the same parameters $t_0/l_0 = 0.1$ and $\lambda = 1/20$.

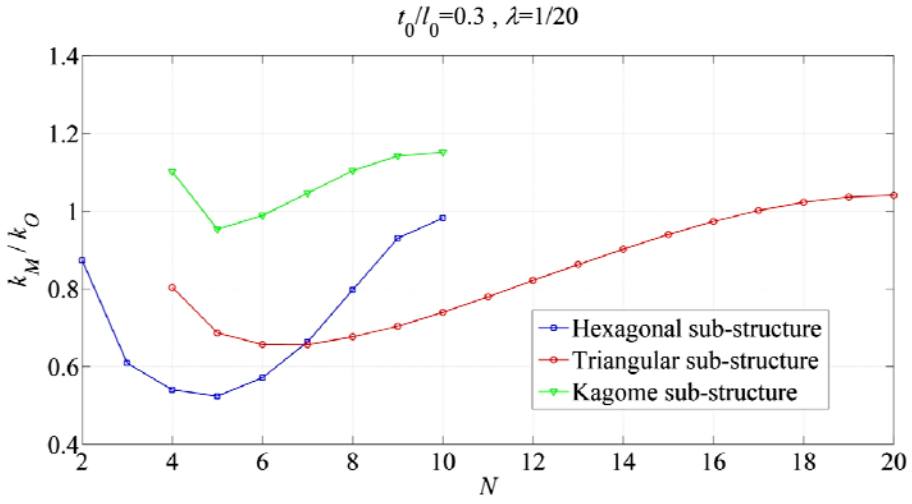

Fig. 3.19 The relative bulk modulus k_M/k_O *vs* N for different sub-structures with the same parameters $t_0/l_0 = 0.3$ and $\lambda = 1/20$.

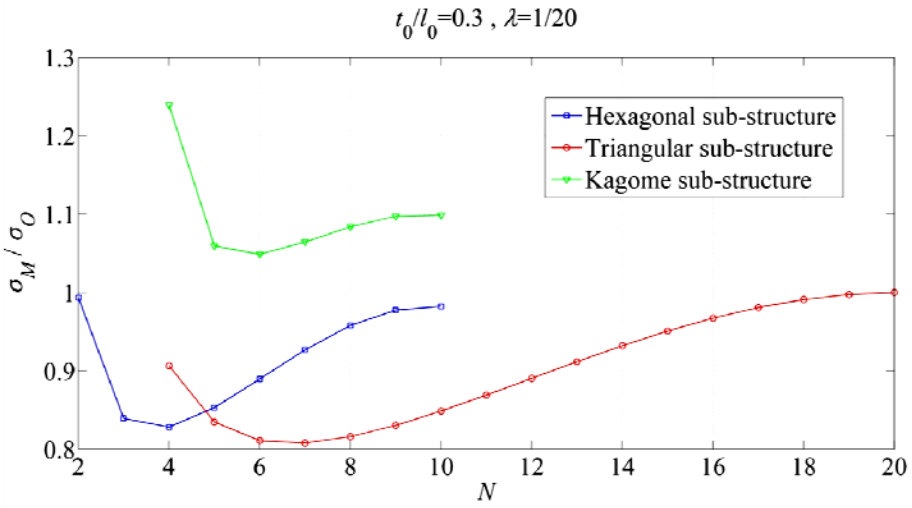

Fig. 3.20 The relative thermal conductivity σ_M/σ_O *vs* N for different sub-structures with the same parameters $t_0/l_0 = 0.3$ and $\lambda = 1/20$.

For the comparisons on bulk modulus and thermal conductivity of the three MHHs, the parameters $t_0/l_0 = 0.3$ and $\lambda = 1/20$ are employed, and the results are depicted in Figs. 3.19 and 3.20. From the two figures, we can say that the MHH with Kagome sub-structure is the optimal structure to design the elastic moduli and transport properties of the multifunctional regular hexagonal honeycomb.

3.7 Conclusions

In this chapter, we have studied the in-plane elastic properties and transport properties of a new class of MHH, which are formed by replacing the ORHH solid cell walls with three types of equal-mass isotropic honeycomb sub-structures. The analytical results show that with the hexagonal sub-structure it is difficult to greatly increase the elastic and shear moduli of the MHH. Different from the hexagonal sub-structure, the triangular and Kagome sub-structures share a similar improvement on the MHH Young's and shear moduli, and the improvement is substantial, i.e., from 1

to 3 orders of magnitude, depending on the cell-wall thickness-to-length ratio t_0/l_0 of the ORHH. At the same time, if t_0/l_0 is large enough, the effective bulk modulus and transport ability of the MHH with Kagome sub-structure can be larger than those of the ORHH structure. These interesting results show a possibility to design new hierarchical honeycombs for multifunctional applications, e.g., the metal MHH can be used as the light weight sandwich panels in electronic packages and airborne devices, where both the structural and thermal characteristics are desirable.

Appendix A: MHH cell wall with hexagonal sub-structures

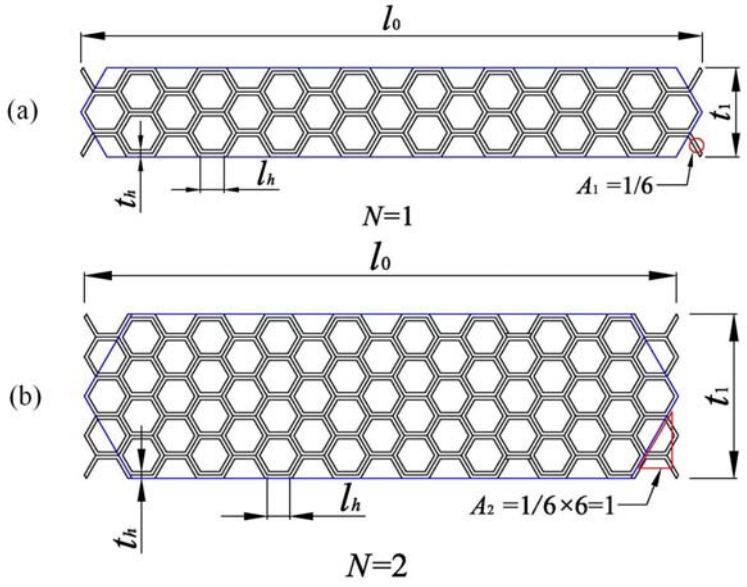

Fig. A Schematics of MHH cell walls in Fig. 1b: (a) $N=1$; (b) $N=2$.

Fig. A shows the representative cell walls of the MHH with regular hexagonal sub-structures shown in Fig. 3.3b. The mass of the sub-structure is distributed uniformly among the half-thickness hexagonal sub-structure cells within the blue hexagon.

From Fig. A, we can see that the number of the half-thickness hexagonal sub-structure cells M can be determined by n and N as the following form:

$$M = 2N\left[n+(n+1)\right]+\frac{1}{6}(2n)-4A_N = 2N(2n+1)+\frac{n}{3}-4A_N \tag{A1}$$

in which $A_1 = 1/6$ and $A_2 = 1$.

Here, A_N depends on N, so we find A_N generally expressed as:

$$A_N = \frac{(2N+1)(N-1)+1}{6} \quad (N \geq 1) \tag{A2}$$

Appendix B: MHH cell wall with triangular sub-structures

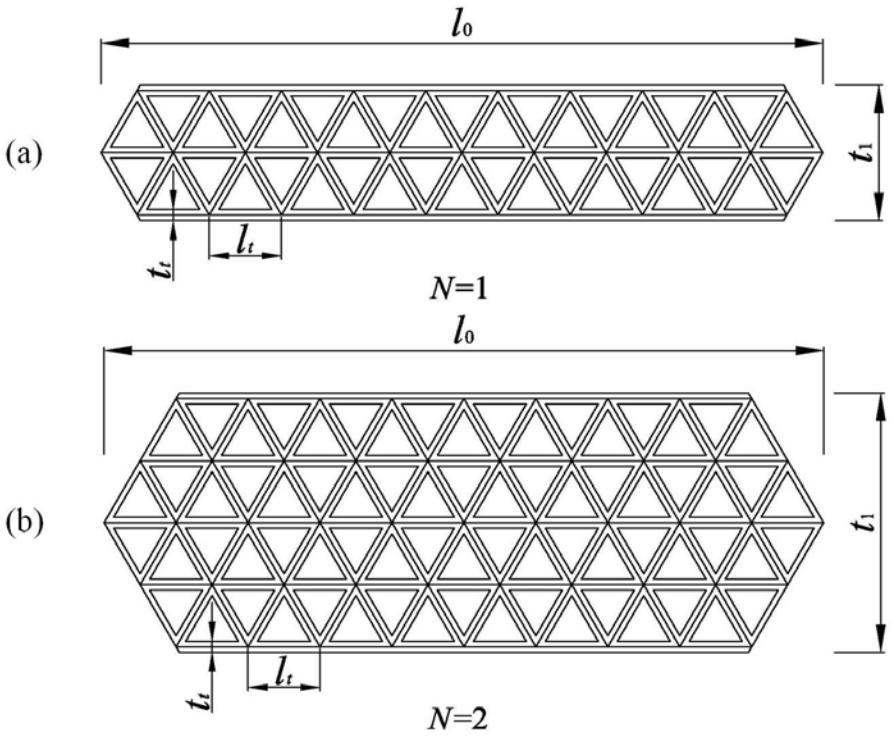

Fig. B Schematics for the representative cell walls of the MHH with triangular sub-structures: (a) $N=1$; (b) $N=2$.

Fig. B schematically shows the cell walls of the MHH with triangular sub-structures (Fig. 3.8b).The hierarchical length ratio is $\lambda = 1/n$. M is the total number of the half-thickness triangular cells in one sub-structure cell wall. It is easy to get the following relation between M, N and n:

$$\begin{aligned} &N=1:\ M=2\left(2n\times 1-1\right)+\frac{2}{3}\left(n-1\right)\\ &N=2:\ M=2\left(2n\times 2-1-1-2\right)+\frac{2}{3}\left(n-2\right)\\ &N=3:\ M=2\left(2n\times 3-1-1-2-2-3\right)+\frac{2}{3}\left(n-3\right) \end{aligned} \tag{B1}$$

Then, by inductive method, we find:

$$M=2\left(2n\times N-B_N\right)+\frac{2}{3}\left(n-N\right)\quad 1\le N\le n \tag{B2}$$

with

$$B_N=N^2 \tag{B3}$$

Substituting Eq. (B3) into Eq. (B2) gives:

$$M=2N\left(2n-N\right)+\frac{2}{3}\left(n-N\right)\quad (1\le N\le n) \tag{B4}$$

Appendix C: MHH cell wall with Kagome sub-structures

Fig. C schematically shows the cell walls of the MHH with Kagome sub-structures. The hierarchical length ratio is $\lambda = 1/n$. M is the total number of the triangular cells contained in one Kagome sub-structure cell wall. Then, the relationship between M, N and n are expressed as:

$$\begin{aligned} &N=1:\ M=2\left[\left(n-1\right)-0\right]\\ &N=2:\ M=2\left[2\left(n-1\right)-2\right]\\ &N=3:\ M=2\left[3\left(n-1\right)-2-4\right] \end{aligned} \tag{C1}$$

Then, by inductive method, we find:

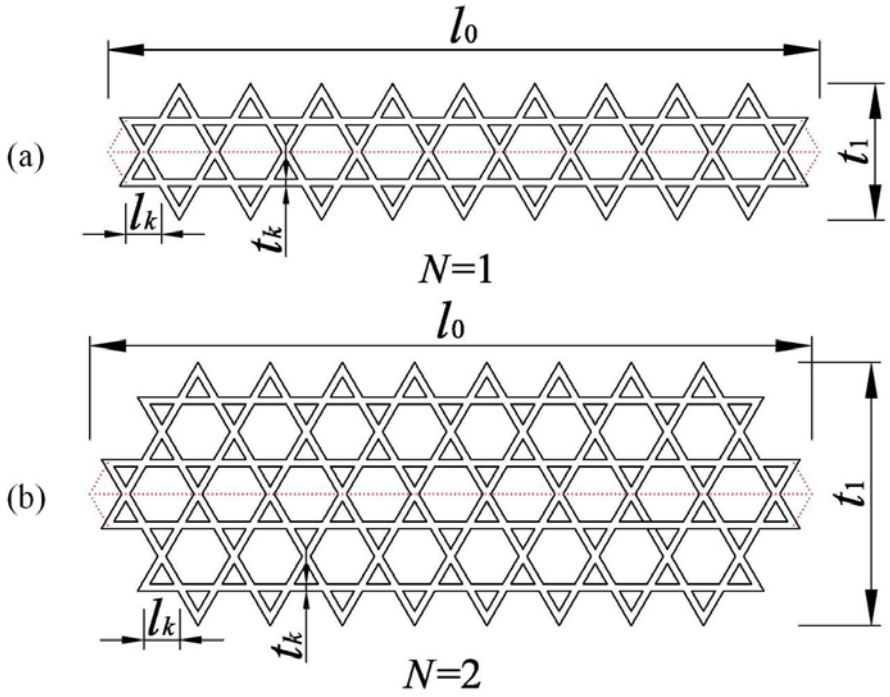

Fig. C Schematics for the representative cell walls of the MHH with Kagome sub-structures: (a) $N=1$; (b) $N=2$.

$$M = 2\left[N\left(n-1\right)-C_N\right] \quad 1 \le N \le \frac{n}{2} \tag{C2}$$

with

$$C_N = N\left(N-1\right) \tag{C3}$$

Substituting Eq. (C3) into Eq. (C2), M is derived:

$$M = 2N\left(n-N\right) \quad (1 \le N \le \frac{n}{2}) \tag{C4}$$

References

Ajdari, A., Jahromi, B.H., Papadopoulos, J., Nayeb-Hashemi, H., Vaziri, A., 2012.Hierarchical honeycombs with tailorable properties. International Journal of Solids and Structures 49, 1413-1419.

Bitzer, T., 1994. Honeycomb marine applications. Journal of Reinforced Plastics and Composites 13, 355-360.

Burgueno, R., Quagliata, M.J., Mohanty, A.K., Mehtad, G., Drzale, L.T., Misraf, M., 2005. Hierarchical cellular designs for load-bearing biocomposite beams and plates. Materials Science and Engineering A 390, 178-187.

Carpinteri, A., Pugno, N., 2008. Mechanics of hierarchical materials. International Journal of Fracture 150, 221-226.

Chen, Q., Pugno, N., 2011. Modeling the elastic anisotropy of woven hierarchical tissues. Composites Part B: Engineering 42, 2030-2037.

Chen, Q., Pugno, N., 2012a. Mechanics of hierarchical 3-D nanofoams. Europhysics Letters 97, 26002.

Chen, Q., Pugno, N., 2012b. In-plane elastic buckling of hierarchical honeycomb materials, European Journal of Mechanics A/Solids 34, 120-129.

Chen, Q., Pugno, N., 2012c. Competition between in-plane buckling and bending collapses in nano-honeycombs. Europhysics Letters 98, 16005.

Evans, A.G., Hutchinson, J.W., Fleck, N.A., Ashby, M.F., Wadley, H.N.G., 2001. The topology design of multifunctional cellular metals. Progress in Materials Science 46, 309-327.

Fan, H.L., Jin, F.N., Fang, D.N., 2008. Mechanical properties of hierarchical cellular materials. Part I: Analysis. Composite Science and Technology 68, 3380-3387.

Fratzl, P., Weinkamer, R., 2007. Nature's hierarchical materials. Progress in Materials Science 52, 1263-1334.

Garcia, A.P., Pugno, N., Buehler, M.J., 2011. Superductile, wavy silica nanostructures inspired by diatom algae. Advanced Engineering Materials 13, B405-B414.

Gao, H., 2006. Application of fracture mechanics concepts to hierarchical biomechanics of bone and bone-like materials. International Journal of Fracture 138, 101-137.

Gibson, L.J., Ashby, M.F., 1997. Cellular Solids, Structures and Properties, second ed. Cambridge University Press.

Gu, S., Lu, T.J., Evans, A.G., 2001. On the design of two-dimensional cellular metals for combined heat dissipation and structural load capacity. International Journal of Heat and Mass Transfer 44, 2163-2175.

Hashin, Z., Shtrikman, S., 1962. A variational approach to the theory of the effective magnetic permeability of multiphase materials. Journal of Applied Physics 33(10): 3125- 3131.

Hashin, Z., Shtrikman, S., 1963. A variational approach to the theory of the elastic behaviour of multiphase materials. Journal of the Mechanics and Physics of Solids 11(2): 127-140.

Hayes, A.M., Wang, A., Dempsey, B.M., McDowell, D.L., 2004. Mechanics of linear cellular alloys. Mechanics of Materials 36, 691-713.

Huang, J.S., Gibson, L.J., 1994. Microstructural design of cellular materials—I: honeycomb beams and plates. Acta Metallurgica et Materialia 43, 1643-1650.

Hyun, S., Torquato, S., 2000. Effective and transport properties of regular honeycombs for all densities. Journal of Materials Research 15, 1985-1993.

Hyun, S., Torquato, S., 2002. Optimal and manufacturable two-dimensional, Kagome-like cellular solids. Journal of Materials Research 17, 137-144.

Jasiuk, I., Chen, J., Thorpe., M.F., 1994. Elastic moduli of two dimensional materials with polygonal and elliptical holes. Applied Mechanics Reviews 47 (1), part 2, S18-S28.

Kooistra, G.W., Deshpande, V., Wadley, H.N.G., 2007. Hierarchical corrugated core sandwich panel concepts. Journal of Applied Mechanics 74, 259-268.

Lakes, R., 1993. Materials with structural hierarchy. Nature 361, 511-515.

Lu, T.J., 1999. Heat transfer efficiency of metal honeycombs. International Journal of Heat and Mass Transfer 42, 2031-2040.

Masters, I.G., Evans, K.E., 1996. Models for the elastic deformation of honeycombs. Composite Structures 35, 403-422.

Price, T., Timbrook, R.L., 2001, Structural honeycomb panel building system, Patent number US6, 253, 530 B1. 3 July.

Pugno, N., 2006. Mimicking nacre with super-nanotubes for producing optimized super-composites. Nanotechnology 17, 5480-5484.

Pugno, N., Carpinteri, A., 2008. Design of micro-nanoscale bio-inspired hierarchical materials. Philosophical Magazine Letters 88, 397-405.

Pugno, N., Chen, Q., 2011. In plane elastic properties of hierarchical cellular solids, Engineering Procedia, Physics Engineering 10, 3026-3031.

Taylor, C.M., Smith, C.W., Miller, W., Evans, K.E., 2011.The Effects of hierarchy on the in-plane elastic properties of honeycombs. International Journal of Solids and Structures 48, 1330-1339.

Thompson, R.W., Matthews, F.L., 1995. Load attachments for honeycomb panels in racing cars. Materials and Design 16, 131-150.

Wadley, H.N.G., 2006. Multifunctional periodic cellular metals. Philosophical Transactions of the Royal Society A 364, 31-68.

Wadley, H.N.G., Fleck, N.A., Evans, A.G., 2003. Fabrication and structural performance of periodic cellular metal sandwich structures. Composites Science and Technology 63, 2331-2343.

Wang, A.J., McDowell, D.L., 2004. In-plane stiffness and yield strength of the periodic metal honeycombs. Journal of Engineering Materials and Technology 126, 137-156.

Wang, B., Wang, B., Cheng, G., 2007. Multifunctional design of sandwich panels with Kagome-like cores. Acta Materiae Compositae Sinica 24, 109-115.

Wen, T., Tian, J., Lu, T.J., Queheillalt, D.T., Wadley, H.N.G., 2006. Forced convection in metallic honeycomb structures. International Journal of Heat and Mass Transfer 49, 3313-3324.

Wilson, S., 1990. A new face of aerospace honeycomb. Materials and Design 11, 323-326.

Zhao, Q., Kreplak, L., Buehler, M.J., 2009. Hierarchical Structure Controls Nanomechanical Properties of Vimentin Intermediate Filaments. PLoS ONE, 4, e7294. doi:10.1371/journal.pone.00072

Chapter 4

In plane stiffness of multifunctional hierarchical honeycombs with negative Poisson's ratio sub-structures

Compared with triangular, square and Kagome honeycombs, hexagonal honeycomb has superior heat dissipation capabilities, but its lower in-plane stiffness hinders its multifunctional applications. In this chapter, comparing it with an original regular hexagonal honeycomb (ORHH) of identical mass, we propose a multifunctional hierarchical honeycomb (MHH) with negative Poisson's ratio (NPR) sub-structures. This MHH is constructed by replacing the solid cell walls of the ORHH with two kinds of NPR honeycombs, the anisotropic re-entrant honeycomb or the isotropic chiral honeycomb. Based on the Euler beam theory, formulas for the Young's moduli of these two kinds of MHH structures are derived. Results show that by appropriately adjusting the geometrical parameters both the re-entrant honeycomb (when the cell-wall thickness-to-length ratio of the ORHH is less than 0.045) and the chiral honeycomb (when the cell-wall thickness-to-length ratio of the ORHH is less than 0.75) can greatly tune the in-plane stiffness of the MHH structure. The presented theory could thus be used in designing new tailorable hierarchical honeycomb structures for multifunctional applications.

4.1 Introduction

As one typical kind of low density cellular solids, honeycomb structures have been applied in many fields such as aerospace and automotive industries in which they are mainly used as cores of the light-weight sandwich panel structures (Wilson, 1990; Bitzer, 1994; Thompson and Matthews, 1995; Price et al., 2001). In addition to the appealing low-density and specific mechanical properties, honeycombs also have other attractive functionalities, e.g., heat transfer, thermal protection, catalysis application, and so on (Lu, 1999; Gu et al., 2001; Hyun and Torquato, 2002; Wen et al., 2006). Referring to the heat transfer properties, comparing with the triangular, square and Kagome honeycombs, the regular hexagonal metal honeycombs provide the highest level of heat dissipation when used as heat sink media (Lu 1999; Gu et al., 2001; Wang et al. 2007). However, the regular hexagonal honeycombs have much lower in plane stiffness which greatly restricts their multifunctional applications. To improve the in plane stiffness of regular hexagonal honeycombs, the crucial role on stiffness, strength and toughness that hierarchy plays in both natural and bio-inspired materials has been exploited (Lakes, 1993; Pugno, 2006; Gao, 2006; Pugno and Carpinteri, 2008; Carpinteri and Pugno, 2008; Zhao, et al., 2009, Fratzl and Weinkamer, 2007; Pugno and Chen, 2011; Chen and Pugno, 2011; Chen and Pugno, 2012a, b, c; Burgueno et al., 2005; Fan et al., 2008; Garcia et al., 2011). In the previous chapter we (Sun et al., in submission) proposed multifunctional hierarchical honeycombs (MHH), which are formed by replacing the solid cell walls of an original regular hexagonal honeycomb (ORHH) with three different isotropic honeycomb sub-structures possessing hexagonal, triangular or Kagome lattices respectively. Analytical results show that, when compared with the ORHH, triangular and Kagome sub-structures could greatly increase the in plane Young's modulus of the MHH structure, up to 3 orders of magnitude depending on the cell wall thickness-to-length ratio of the ORHH.

The concept of negative Poisson's ratio (NPR) can also be explored to improve the elastic moduli of regular hexagonal honeycombs. One of the two interesting NPR cellular solids are the anisotropic re-entrant honeycomb (Masters and Evans, 1996; Gibson and Ashby, 1997) and the isotropic (Poisson's ratio -1) chiral honeycomb (Prall and Lakes, 1996). The multifunctionality of these two kinds of honeycombs has been widely studied. Scarpa and Tomlinson (2000) studied the vibration of a sandwich plate

with re-entrant honeycomb cores and suggested that the dynamic performance of a sandwich structure could be significantly improved using the re-entrant cell cores. Ruzzene (2004) analyzed the vibration and sound radiation of sandwich beams with re-entrant honeycomb truss cores and indicate that re-entrant configurations are generally more effective for vibration and sound transmission reduction applications. Innocenti and Scarpa (2009) studied the thermal conductivity and heat transfer properties of the multi-re-entrant honeycomb structures and showed that this auxetic honeycomb configurations show higher out-of-plane conductivity, strong in-plane thermal anisotropy and the lowest peak temperatures during heat transfer between the bottom and top faces of honeycomb panels. Besides, numerical and experimental simulations showed that chiral honeycombs have attractive dynamic properties when used as the core of airfoils (Spadoni et al., 2006; Spadoni and Ruzzene, 2007a; Bettini et al., 2009). At the same time, Spadoni et al. (2009) studied the phononic properties of the hexagonal chiral lattices and suggested this kind of cellular lattices as potential building blocks for the design of meta-materials of interest for acoustic wave-guiding applications.

In this chapter, by substituting the solid cell wall of a ORHH with anisotropic re-entrant honeycombs or isotropic chiral honeycombs, two new kinds of MHH structures with NPR sub-structures are introduced. Based on the Euler beam theory, formulas for the in-plane Young's moduli of these two kinds of MHH structures are finally derived. The presented theory could be used in designing new tailorable hierarchical multifunctional honeycombs.

4.2 MHH with re-entrant honeycomb sub-structures

4.2.1 Basic theory

At first, we consider the MHH with anisotropic re-entrant honeycomb sub-structures (Fig. 4.1). Fig. 4.1a is a ORHH with cell-wall thickness and length denoted by t_0 and l_0, respectively; Fig. 4.1b is an equal-mass MHH with the cell-wall thickness and length denoted by t_1 and l_0, respectively. We can see that the cell-wall lengths of the ORHH and the MHH are identical. In particular, one of the

MHH cell walls in Fig. 4.1b is shown in Fig. 4.1c. The cell-wall thickness, lengths parallel and inclined to the local direction 2 for re-entrant hexagonal cells are denoted by t_r, h_r and l_r respectively. The angle between the inclined cell wall and the local direction 1 is denoted by θ ($\theta < 0^\circ$). The out-of-plane depth is a constant and identical for both structures.

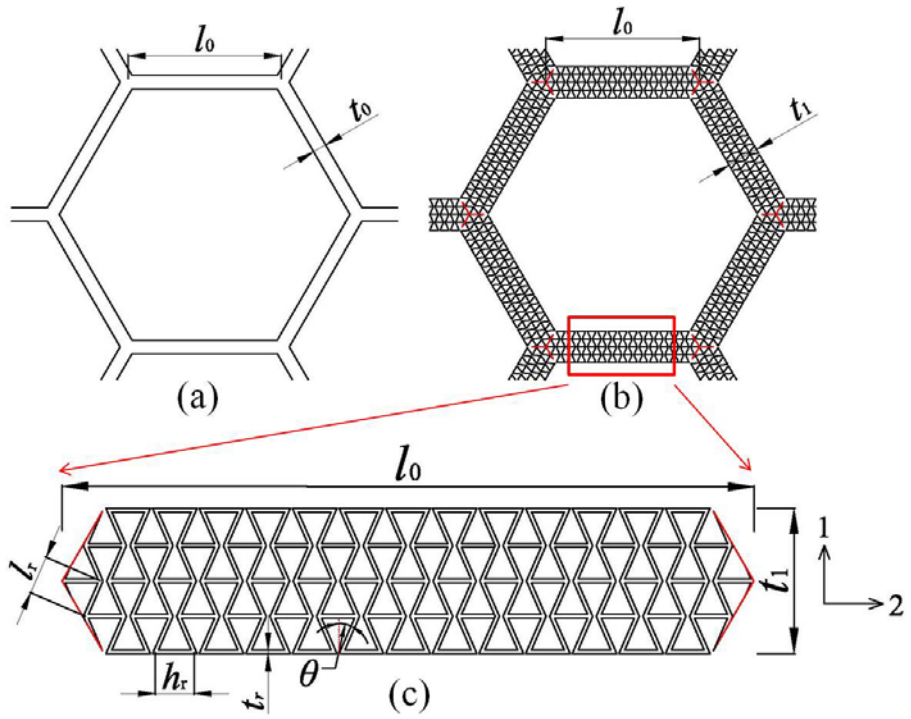

Fig. 4.1 (a) The original regular hexagonal honeycomb (ORHH); (b) the tailorable multifunctional hierarchical honeycomb (MHH) with re-entrant honeycomb sub-structures; (c) amplification of a re-entrant hexagonal lattice cell wall in (b).

For simplicity of the calculation we suppose that both the cell walls of the MHH structure and re-entrant honeycomb substructures are Euler beams. That is to say, under small deformations we only consider the bending of the cell walls of the MHH structure and re-entrant honeycomb sub-structures, which requires that $t_1/l_0 < 0.25$, $t_r/h_r < 0.25$ and $t_r/l_r < 0.25$ (Gibson and Ashby, 1997). Under the above assumptions

we can approximately treat this MHH structure as isotropic, even though its cell walls are constituted by anisotropic re-entrant honeycomb substructures.

Here we define $h_r/l_r=\alpha$ and $t_r/l_r=\beta$. The geometry of Fig. 4.1c implies that:

$$l_0=n\left(h_r+2l_r\sin\theta\right)+\left(n+1\right)h_r=n\left(\alpha+2\sin\theta\right)l_r+\left(n+1\right)\alpha l_r \tag{4.1}$$

where, $n+1$ is the number of solid re-entrant hexagonal cell walls lying on the middle line of the MHH cell wall (e.g., in Fig. 4.1c, n=15). Defining $\lambda=l_r/l_0$ as the hierarchical length ratio and rearranging Eq. (4.1) provides

$$\lambda=\frac{l_r}{l_0}=\frac{1}{n\left(\alpha+2\sin\theta\right)+\left(n+1\right)\alpha} \tag{4.2}$$

Then, defining N as the number of re-entrant hexagonal cells away from the middle line of the MHH cell walls (e.g., in Fig. 4.1c, N=1), from the geometric analysis we get the cell wall thickness of the MHH structure:

$$t_1=2l_r\cos\theta\times 2N+\frac{t_r}{2}\times 2=\left(4N\cos\theta+\beta\right)l_r=\left(4N\cos\theta+\beta\right)\lambda l_0 \tag{4.3}$$

that is

$$\frac{t_1}{l_0}=\lambda\left(4N\cos\theta+\beta\right) \tag{4.4}$$

Then from the precondition $t_1/l_0<0.25$ we obtain $N_{\max}$, the upper bound of N:

$$N_{\max}=fl\left[\frac{1}{16\lambda\cos\theta}\right] \tag{4.5}$$

where, '*fl*[ ]' is the floor function, which denotes the largest integer not greater than the term in the brackets.

The mass equivalence between the cell wall of the ORHH and that of the MHH structure gives the following relationship (see Appendix A):

$$BD\beta^3+\left(AD+BC\right)\beta^2+AC\beta-E=0 \tag{4.6}$$

in which $A=2N\left(2n+1\right)\left(\alpha+2\right)+\alpha\left(n+1\right)$, $B=\left[2N\left(2n+1\right)-\left(n+1\right)\right]\left(\frac{1}{2}\tan\theta-\frac{1}{\cos\theta}\right)$,

$C=1-\frac{2}{\sqrt{3}}N\lambda\cos\theta$, $D=-\frac{1}{2\sqrt{3}}\lambda$, $E=\frac{1}{\lambda^2}\left[\frac{t_0}{l_0}-\frac{1}{2\sqrt{3}}\left(\frac{t_0}{l_0}\right)^2\right]$. Through Newton's method we solve Eq. (4.6) and get the solutions for β. Then, through the precondition $\beta<0.25$, we can obtain $N_{\min}$, the lower bound of N.

Defining E_O, E_M and E_{r2} as the in plane Young's moduli of the ORHH, MHH and the re-entrant honeycomb sub-structure in the local direction 2, we find (Gibson and Ashby, 1997):

$$\frac{E_O}{E_s}=2.3\left(\frac{t_0}{l_0}\right)^3 \tag{4.7}$$

$$\frac{E_M}{E_{r2}}=2.3\left(\frac{t_1}{l_0}\right)^3 \tag{4.8}$$

$$\frac{E_{r2}}{E_s}=\left(\frac{t_r}{l_r}\right)^3\frac{h_r/l_r+\sin\theta}{\cos^3\theta}=\beta^3\frac{\alpha+\sin\theta}{\cos^3\theta} \tag{4.9}$$

Combining Eqs. (4.7) to (4.9) gives the relative Young's modulus E_M/E_O:

$$\frac{E_M}{E_O}=\frac{\left(t_1/l_0\right)^3\beta^3\left(\alpha+\sin\theta\right)}{\left(t_0/l_0\right)^3\cos^3\theta} \tag{4.10}$$

4.2.2 Effects of α, N, t_0/l_0 *and* λ on the relative Young's moduli

To investigate the influence of N on the relative elastic moduli E_M/E_O, here we consider the following examples with parameters $n=30$, $\theta=-5^\circ$, $t_0/l_0=0.01$, 0.02, 0.03, 0.04, 0.045 and $\alpha=1$, 1.5, 2 and 3. The results of E_M/E_O vs N for different t_0/l_0 are shown in Fig. 4.2. It is easy to see from Fig. 4.2 that in general E_M/E_O increases with the increases of N and α.

Comparing Eqs. 4.2(a) to 4.2(d) shows that the parameter α has a vital influence on E_M/E_O, which can also be seen from Eq. (4.10). When $\alpha \le 1.5$ the relative elastic moduli $E_M/E_O < 1$ (Figs. 4.2(a) and 4.2(b)), which means that for $\alpha \le 1.5$ the Young's modulus of the MHH structure with re-entrant honeycomb sub-structures is smaller than that of the ORHH. Note that when $t_0/l_0 > 0.045$ the assumptions in section 3.1 are not satisfied. So we only consider the case of $t_0/l_0 \le 0.045$.

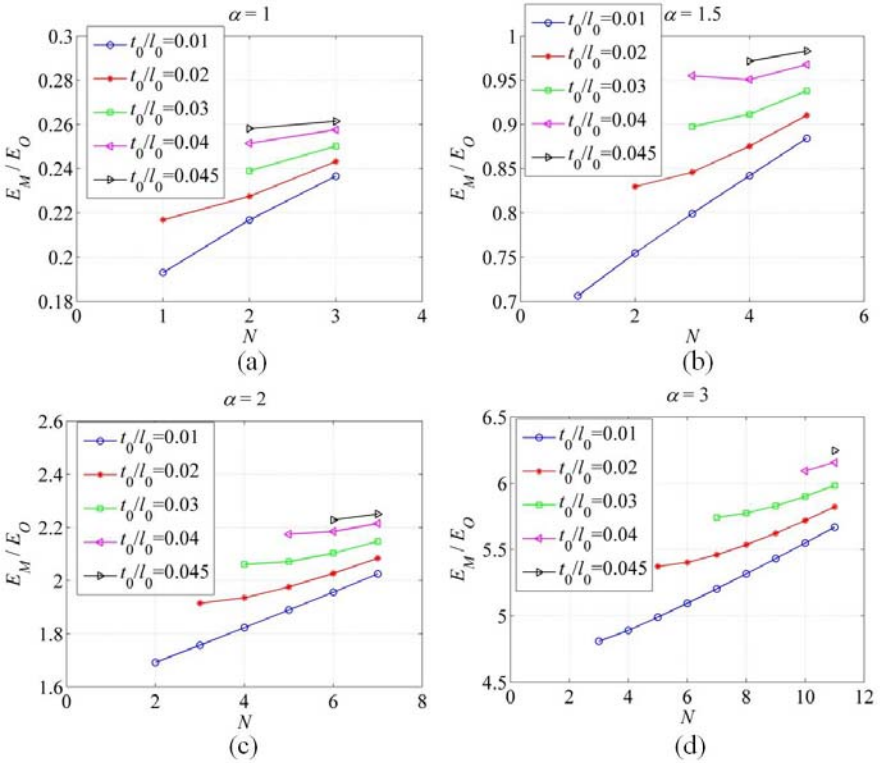

Fig. 4.2 The relative Young's modulus E_M/E_O *vs* N for different t_0/l_0 with (a) $\alpha = 1$; (b) $\alpha = 1.5$; (c) $\alpha = 2$; (d) $\alpha = 3$.

To see the effect of θ on E_M/E_O, we use the parameters $n = 30$, $\alpha = 3$, $t_0/l_0 = 0.01$, 0.02, 0.03, 0.04, $\theta = -60^\circ \sim -5^\circ$. The results involving the maximum E_M/E_O and θ are given in Fig. 4.3. It is apparent that the maximum E_M/E_O decreases with the decrease of θ. At the same time, to see the effects of λ, i.e., n, on E_M/E_O, we

study the parameters $\alpha = 4$, $\theta = -5^{\circ}$, $t_0/l_0 = 0.01$, 0.03 and $n = 10-50$. The results are shown in Fig. 4.4(a) which shows that with the increase of n the maximum E_M/E_O increases in a sawtooth shape. The reason is due to the change of $N_{\max}$ with the increase of n (Fig. 4.4(b)).

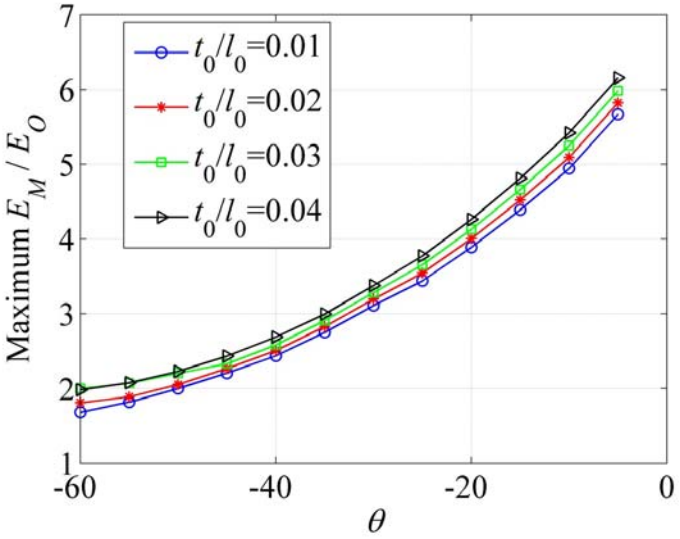

Fig. 4.3 The maximum E_M/E_O vs θ for different t_0/l_0

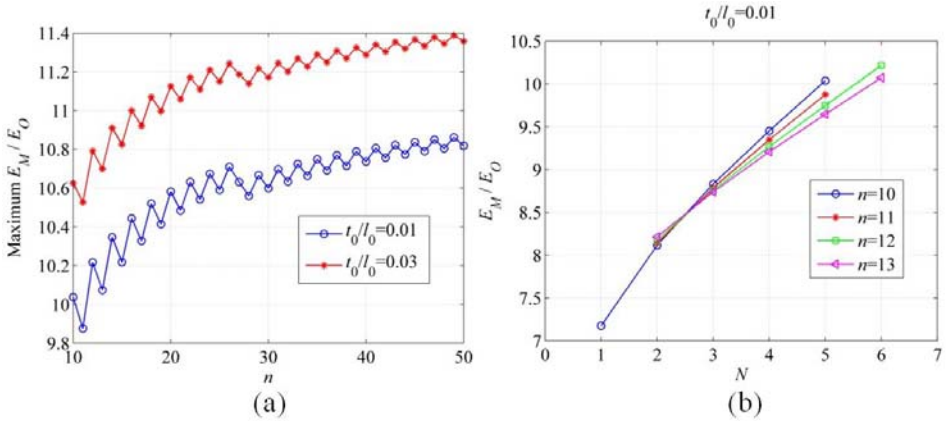

Fig. 4.4 (a) The maximum E_M/E_O vs n for different t_0/l_0; (b) E_M/E_O vs N for different n with $t_0/l_0 = 0.01$

4.3 MHH with isotropic chiral honeycomb sub-structures

4.3.1 Basic theory

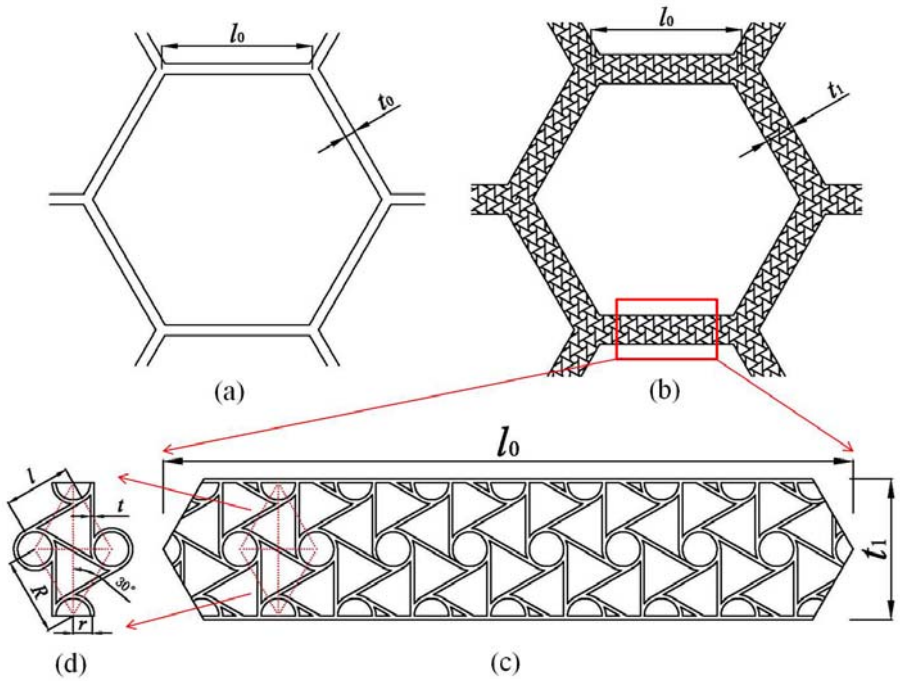

Fig. 4.5 Schematics of (a) the ORHH; (b) the tailorable MHH with chiral honeycomb sub-structures; (c) amplification of a chiral lattice cell wall in (b); (d) geometrical parameters of the chiral honeycomb cell in (c).

In this section, we substitute the ORHH cell walls with equal-mass isotropic chiral honeycomb sub-structures, see Fig. 4.5. The cell wall thickness, the circular node radius, the distance between the centers of the adjacent circular cells and the length of the ligaments in the chiral honeycomb are denoted by t, r, R and l, respectively (Fig. 4.5d). Then the geometrical relation $r^2 + l^2/4 = R^2/4$ holds. We suppose $t/l < 0.25$ so

that the Euler beam theory can be applied, i.e., only the bending of ligaments is considered (Prall and Lakes, 1996; Gibson and Ashby, 1997).

As defined in Section 3, here the hierarchical length ratio is expressed as

$$\lambda = \frac{R}{l_0} = \frac{1}{n} \quad (n \geq 1) \tag{4.11}$$

where, n is the number of the distance R lying on the middle line of the MHH cell walls. Supposing

$$\frac{R}{r} = k \tag{4.12}$$

and combining it with the relation $r^2 + l^2/4 = R^2/4$, gives:

$$\begin{cases} \dfrac{r}{l} = A = \dfrac{1}{\sqrt{k^2 - 4}} \\ \dfrac{l}{l_0} = B = \dfrac{\sqrt{k^2 - 4}}{nk} \\ \dfrac{R}{l} = C = \dfrac{k}{\sqrt{k^2 - 4}} \end{cases} \tag{4.13}$$

Defining N as the number of circular cells in the thickness direction of the cell wall of the MHH structure, similarly as done in Section 2, a geometrical analysis on Fig. 4.5c provides $N_{\max}$, the upper bound of N, and t_1, the thickness of the MHH cell walls:

$$N_{\max} = n \tag{4.14}$$

$$t_1 = \begin{cases} \sqrt{3}NR + 2t & 1 \leq N < N_{\max} \\ \sqrt{3}l_0 & N = N_{\max} \end{cases} \tag{4.15}$$

Then, rearranging Eq. (4.15) gives

$$\frac{t_1}{l_0} = \begin{cases} \dfrac{\sqrt{3}N}{n} + 2B\beta & 1 \leq N < N_{\max} \\ \sqrt{3} & N = N_{\max} \end{cases} \tag{4.16}$$

in which $\beta = t/l$ is the thickness-to-length ratio of the ligaments.

If $N < N_{\max}$, from Fig. 4.5c, according to the equal-mass principle, we can find

$$t_0 l_0 - \frac{1}{2\sqrt{3}} t_0^2 = MQ + 2\left(l_0 - NR\right)t = MQ + 2\left(\frac{1}{B} - NC\right)tl \tag{4.17}$$

where, M is the total number of the circular cells in one cell wall of the MHH structure and Q is the in-plane areas of one circular cell and six half-length ligaments. In fact, one circular cell in the MHH cell wall corresponds to six half-length ligaments. M has the following relationship with n and N (see Appendix B):

$$M = N\left(2n - N\right) \quad (1 \le N \le n) \tag{4.18}$$

and

$$\begin{aligned} Q &= \pi\left[\left(r + \frac{t}{2}\right)^2 + \left(r - \frac{t}{2}\right)^2\right] + 6\left\{\frac{1}{2}tl - \left(\left(\frac{\pi}{2} - \tan^{-1}\sqrt{\frac{2r}{t}}\right)\left(r + \frac{t}{2}\right)^2 - \frac{1}{2}\left(r - \frac{t}{2}\right)\sqrt{2tr}\right)\right\} \\ &= 2\pi rt + 3tl - 6\left(\frac{\pi}{2} - \tan^{-1}\sqrt{\frac{2r}{t}}\right)\left(r + \frac{t}{2}\right)^2 + 3\left(r - \frac{t}{2}\right)\sqrt{2tr} \end{aligned} \tag{4.19}$$

Then, rearranging Eq. (4.17) gives

$$\begin{aligned} &\left(2\pi A + 3 + \frac{2}{BM} - \frac{2NC}{M}\right)\beta - 6\left(\frac{\pi}{2} - \tan^{-1}\sqrt{\frac{2A}{\beta}}\right)\left(A + \frac{1}{2}\beta\right)^2 + 3\left(A - \frac{1}{2}\beta\right)\sqrt{2A\beta} \\ &= \frac{1}{B^2 M}\left[\frac{t_0}{l_0} - \frac{1}{2\sqrt{3}}\left(\frac{t_0}{l_0}\right)^2\right] \end{aligned} \tag{4.20}$$

When $N = N_{\max}$, it gives

$$t_0 l_0 - \frac{1}{2\sqrt{3}} t_0^2 = MQ + 2\left(l_0 - NR\right)t = MQ \tag{4.21}$$

and rearranging Eq. (4.21) we obtain

$$\begin{aligned} &\left(2\pi A + 3\right)\beta - 6\left(\frac{\pi}{2} - \tan^{-1}\sqrt{\frac{2A}{\beta}}\right)\left(A + \frac{1}{2}\beta\right)^2 + 3\left(A - \frac{1}{2}\beta\right)\sqrt{2A\beta} \\ &= \frac{1}{B^2 M}\left[\frac{t_0}{l_0} - \frac{1}{2\sqrt{3}}\left(\frac{t_0}{l_0}\right)^2\right] \end{aligned} \tag{4.22}$$

Through Newton's method we can solve Eqs. (4.20) and (4.22) and get the solutions

for β. Then from the precondition $\beta < 0.25$ we can obtain $N_{\min}$, the lower bound of N.

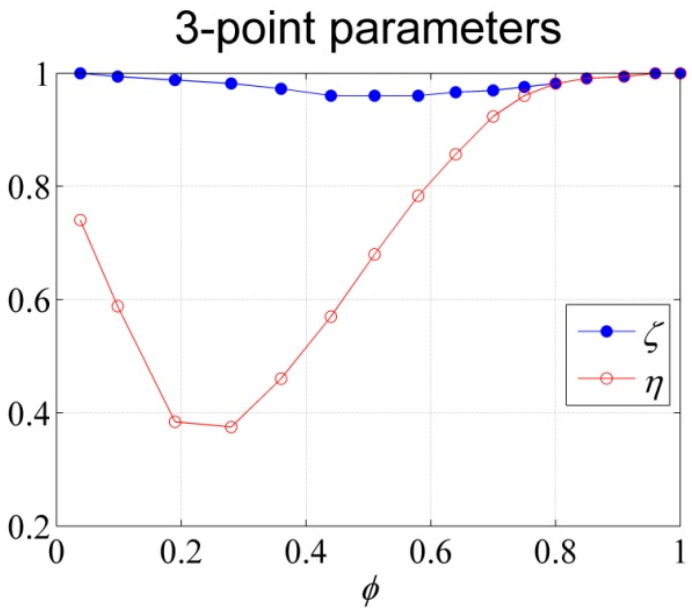

Fig. 4.6 Three-point parameters ζ and η for the regular hexagonal honeycomb (Hyun and Torquato, 2000) *vs* the relative density ϕ

In the previous chapter we derived analytical formulas for the Young's modulus of the regular hexagonal honeycomb at all densities (Sun et al., in submission). Defining E_O, E_M and E_C as the in plane Young's moduli of the ORHH, MHH and the chiral honeycomb sub-structures, using our previous results and referring to the results of Prall and Lakes (1996), we find:

$$\frac{E_O}{E_s} = A_O = \begin{cases} \dfrac{3}{2}\phi_O^3 & \phi_O \le 0.5 \\ \dfrac{\phi_O(2\zeta_O - 1)(\zeta_O + \eta_O - 1)}{\left\{3 - 2\phi_O - 2(2-\phi_O)(1-\zeta_O) + (2-\zeta_O-\eta_O)\left[2\phi_O(1-\zeta_O)-1\right]\right\}} & \phi_O > 0.5 \end{cases} \tag{4.23}$$

$$\frac{E_M}{E_C} = A_M = \begin{cases} \dfrac{3}{2}\phi_M^3 & \phi_M \le 0.5 \\ \dfrac{\phi_M\left(2\zeta_M - 1\right)\left(\zeta_M + \eta_M - 1\right)}{\left\{3 - 2\phi_M - 2\left(2 - \phi_M\right)\left(1 - \zeta_M\right) + \left(2 - \zeta_M - \eta_M\right)\left[2\phi_M\left(1 - \zeta_M\right) - 1\right]\right\}} & \phi_M > 0.5 \end{cases} \tag{4.24}$$

$$\frac{E_C}{E_s} = A_c = \sqrt{3}\left(\frac{t}{l}\right)^3\left(\frac{l}{r}\right)^2 = \sqrt{3}\beta^3\frac{1}{A^2} \tag{4.25}$$

in which

$$\phi_O = \frac{2}{\sqrt{3}}\frac{t_0}{l_0} - \frac{1}{3}\left(\frac{t_0}{l_0}\right)^2 \quad \left(\frac{t_0}{l_0} \le \sqrt{3}\right), \tag{4.26}$$

$$\phi_M = \frac{2}{\sqrt{3}}\frac{t_1}{l_0} - \frac{1}{3}\left(\frac{t_1}{l_0}\right)^2 \quad \left(\frac{t_1}{l_0} \le \sqrt{3}\right), \tag{4.27}$$

ζ_O and η_O, ζ_M and η_M, interpolated from Fig. 4.6, are the three-point parameters corresponding to ϕ_O and ϕ_M respectively; E_s is the Young's modulus of the solid of which the ORHH is made. Combining Eqs. (4.22) to (4.25) gives the relative Young's modulus E_M/E_O:

$$\frac{E_M}{E_O} = \frac{A_M A_c}{A_O} \tag{4.28}$$

4.3.2 Effects of N, t_0/l_0, k and λ on the relative Young's moduli

To see the effect of t_0/l_0 on E_M/E_O, we use the parameters $n = 20$, $k = 20$ and $t_0/l_0 = 0.01 - 0.3$. The results involving the maximum E_M/E_O and t_0/l_0 are shown in Fig. 4.8(a), which indicates that with the increase of n the maximum E_M/E_O increases in a sawtooth shape. The reason of this kind of increasing trend is the change of the range of N with the increase of t_0/l_0 (Fig. 4.8(b)).

To see the effect of k on E_M/E_O, we consider the parameters $n=20$, $t_0/l_0=0.1$ and $k=5$, 10, 20. The results are shown in Fig. 4.9. Apparently E_M/E_O increases with the increase of k. Finally, to see the effects of λ, i.e., n, on E_M/E_O, we investigate the parameters $k=20$, $t_0/l_0=0.1$, 0.2 and $n=10-100$. The related results are shown in Fig. 4.10. We can see that the maximum E_M/E_O also increases in a sawtooth shape with the increase of n. The reason is again the change of the range of N with the increase of n.

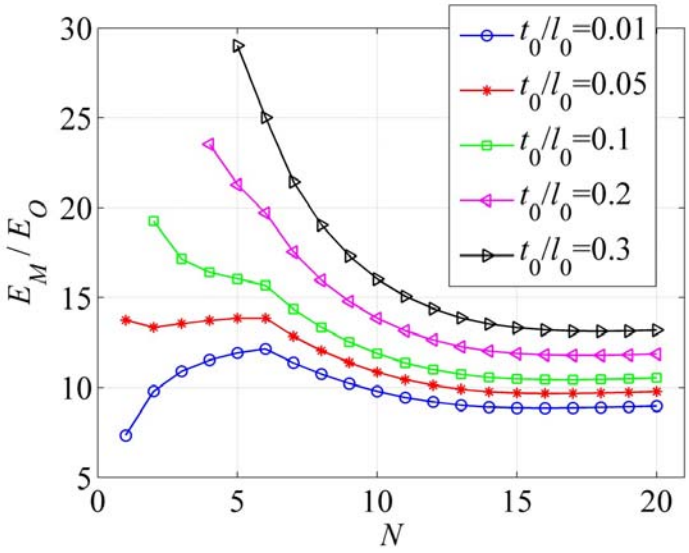

Fig. 4.7 The relative Young's modulus E_M/E_O *vs* N for different t_0/l_0

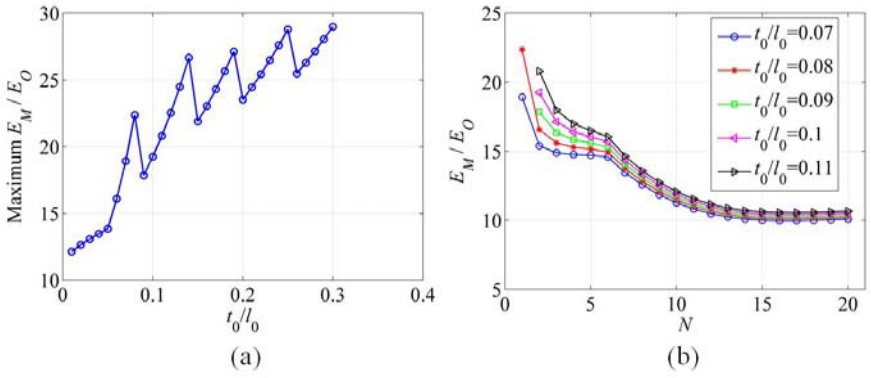

Fig. 4.8 (a)The maximum E_M/E_O *vs* t_0/l_0; (b) E_M/E_O *vs* N for different t_0/l_0

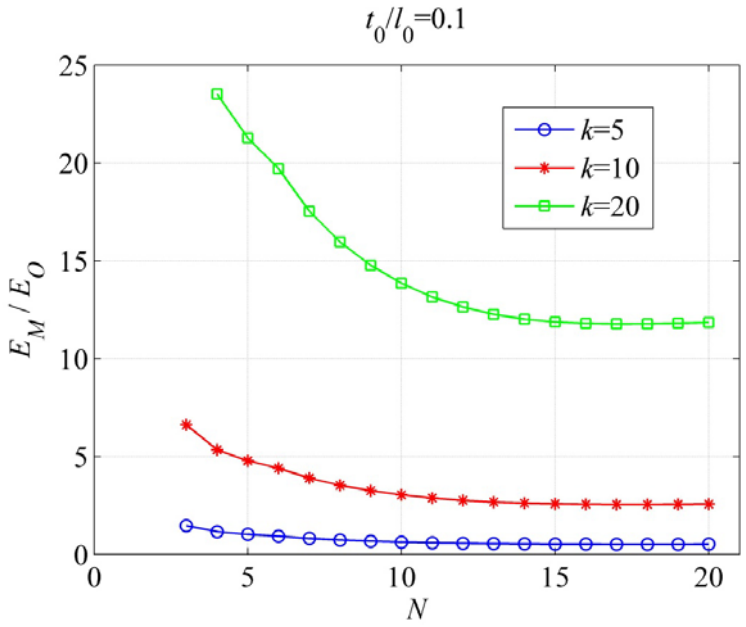

Fig. 4.9 E_M/E_O *vs* N for different k

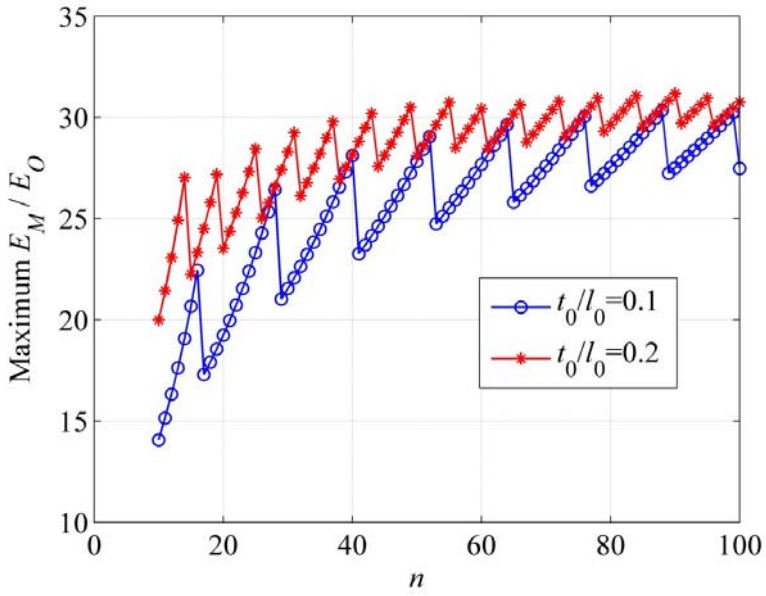

Fig. 4.10 The maximum E_M/E_O *vs* n for different t_0 / l_0

4.4 Conclusions

In this chapter, by substituting the solid cell walls of the original regular hexagonal honeycomb (ORHH) with two equal mass NPR honeycombs, the re-entrant honeycomb and the isotropic chiral honeycomb, two new kinds of multifunctional hierarchical honeycombs are proposed. Based on the Euler beam theory, the analytical formulas for the Young's moduli of these two new MHH structures are derived. Analytical analysis indicates that both the re-entrant honeycomb sub-structures and the chiral honeycomb substructures can greatly increase the in-plane stiffness of the MHH by appropriately designing its geometry. This chapter shows the possibility to design new hexagonal honeycombs for multifunctional applications, which combine the advantages of hierarchical and NPR materials.

Appendix A: MHH cell wall with re-entrant honeycomb sub-structures

In this appendix the mass equivalence between the cell walls of the ORHH and the MHH with re-entrant honeycomb sub-structures is derived. As shown in Fig. A(a), the cell walls of the MHH with re-entrant honeycomb sub-structures are fabricated by cutting the rectangular re-entrant honeycomb beams at the four red lines. The angles between the four red lines and the local direction 2 are all 60°. So the cell wall mass of the ORHH is equal to the mass encased by the four red lines (Fig. A(a)).

Supposing the density of the solid of which the ORHH is made and the out-of-plane depth of the MHH structure are both 1, from geometrical analysis it is easy to obtain the following parameters and the mass of half-thickness re-entrant honeycombs cell

$$\begin{aligned} A' &= 2t_r l_r + \left[h_r + \left(\frac{1}{2}\tan\theta - \frac{1}{\cos\theta} \right) t_r \right] t_r = \left(h_r + 2l_r \right) t_r + \left(\frac{1}{2}\tan\theta - \frac{1}{\cos\theta} \right) t_r^2 \\ &= \left(\alpha + 2 \right) t_r l_r + \left(\frac{1}{2}\tan\theta - \frac{1}{\cos\theta} \right) t_r^2 \end{aligned} \tag{A1}$$

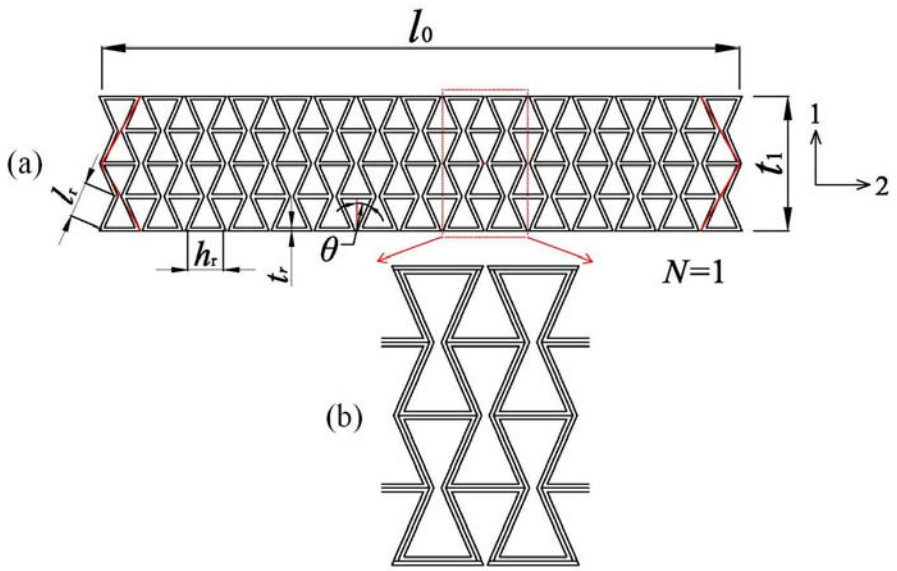

Fig. A (a) Schematics for the representative cell walls of the MHH with re-entrant honeycomb sub-structures ($N=1$) shown in Fig. 4.1(b); (b) details of the re-entrant cells in (a).

The number of the half-thickness re-entrant honeycomb cells in the uncut beam is

$$B' = 2N\left(n+n+1\right) = 2N\left(2n+1\right) \tag{A2}$$

The number of the half-thickness cell walls in the two outward sides is

$$C' = 2\left(n+1\right) \tag{A3}$$

The mass of half-thickness cell walls in the two outward sides is

$$\begin{aligned} D' &= \left(h_r + 2\frac{t_r/2}{\cos\theta} + h_r + 2\frac{t_r/2}{\cos\theta} - 2\frac{t_r}{2}\tan\theta \right)\frac{t_r}{2}\times\frac{1}{2} = \frac{1}{2}h_r t_r + \frac{1}{4}t_r^2\left(\frac{2}{\cos\theta} - \tan\theta\right) \\ &= \frac{1}{2}\alpha l_r t_r + \frac{1}{4}t_r^2\left(\frac{2}{\cos\theta} - \tan\theta\right) \end{aligned} \tag{A4}$$

The ratio of the area encased by the four red lines is

$$E' = 1 - \frac{\frac{1}{2}\times\frac{t_1}{2}\times\frac{t_1}{2}\times\frac{1}{\sqrt{3}}\times 4}{t_1 l_0} = 1 - \frac{1}{2\sqrt{3}}\frac{t_1}{l_0} = 1 - \frac{1}{2\sqrt{3}}\lambda\left(4N\cos\theta + \beta\right) \tag{A5}$$

Then the mass equivalence between the cell walls of the ORHH and the MHH with

re-entrant honeycomb sub-structures gives (Sun et al., in submission)

$$\left(A'B'+C'D'\right)E'=t_0l_0-\frac{1}{2\sqrt{3}}t_0^2 \tag{A6}$$

Rearranging Eq. (A6) gives

$$BD\beta^3+\left(AD+BC\right)\beta^2+AC\beta-E=0 \tag{A7}$$

in which $A=2N\left(2n+1\right)\left(\alpha+2\right)+\alpha\left(n+1\right)$, $B=\left[2N\left(2n+1\right)-\left(n+1\right)\right]\left(\frac{1}{2}\tan\theta-\frac{1}{\cos\theta}\right)$,

$C=1-\frac{2}{\sqrt{3}}N\lambda\cos\theta$, $D=-\frac{1}{2\sqrt{3}}\lambda$, $E=\frac{1}{\lambda^2}\left[\frac{t_0}{l_0}-\frac{1}{2\sqrt{3}}\left(\frac{t_0}{l_0}\right)^2\right]$.

Appendix B: MHH cell wall with chiral honeycomb sub-structures

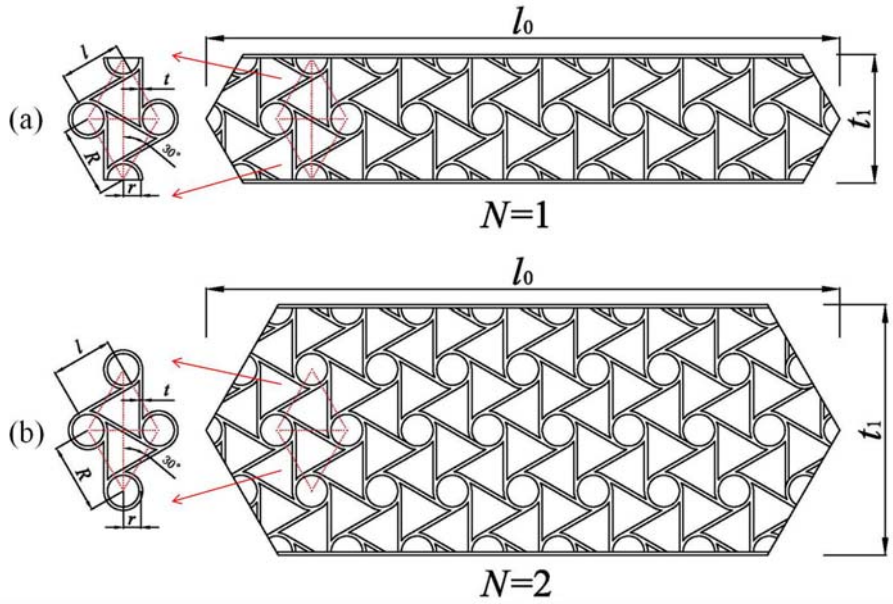

Fig. B Schematics for the representative cell walls of the MHH with chiral honeycomb sub-structures: (a) $N=1$; (b) $N=2$.

Fig. B schematically shows the cell walls of the MHH with chiral honeycomb

sub-structures (Fig. 4.5b). The hierarchical length ratio is $\lambda = 1/n$. M is the number of the circular cells in one cell wall of the MHH structure, N is the number of circular cells in the thickness direction of the cell wall. It is easy to get the following relation between M , N and n :

$$\begin{aligned}
&N=1:\ M=(n-1)+(n-2)+2=2n-(1+2)+2\times 1\\
&N=2:\ M=(n-1)+2(n-2)+(n-3)+2+\frac{1}{2}\times 4\\
&\qquad\quad =4n-(1+2)-(2+3)+2\times 2\\
&N=3:\ M=(n-1)+2(n-2)+2(n-3)+(n-4)+2+\frac{1}{2}\times 8\\
&\qquad\quad =6n-(1+2+3)-(2+3+4)+2\times 3
\end{aligned} \tag{B1}$$

Then, recursively, we find

$$M=N(2n-N)\quad (1\le N\le n) \tag{B2}$$

References

Bettini, P., Airoldi, A., Sala, G., Di Landro, L., Ruzzene, M.,Spadoni, A., 2009. Composite chiral structures for morphing airfoils: numerical analyses and development of a manufacturing process. Composites: Part B, doi:10.1016/j.compositesb.2009.10.005

Bitzer, T., 1994. Honeycomb marine applications. Journal of Reinforced Plastics and Composites 13, 355-360.

Burgueno, R., Quagliata, M.J., Mohanty, A.K., Mehtad, G., Drzale, L.T., Misraf, M., 2005. Hierarchical cellular designs for load-bearing biocomposite beams and plates. Materials Science and Engineering A 390, 178-187.

Carpinteri, A., Pugno, N., 2008. Mechanics of hierarchical materials. International Journal of Fracture 150, 221-226.

Chen, Q., Pugno, N., 2011. Modeling the elastic anisotropy of woven hierarchical tissues. Composites

Part B: Engineering 42, 2030-2037.

Chen, Q., Pugno, N., 2012a. Mechanics of hierarchical 3-D nanofoams. Europhysics Letters 97, 26002.

Chen, Q., Pugno, N., 2012b. In-plane elastic buckling of hierarchical honeycomb materials, European Journal of Mechanics A/Solids 34, 120-129.

Chen, Q., Pugno, N., 2012c. Competition between in-plane buckling and bending collapses in nano-honeycombs. Europhysics Letters 98, 16005.

Fan, H.L., Jin, F.N., Fang, D.N., 2008. Mechanical properties of hierarchical cellular materials. Part I: Analysis. Composite Science and Technology 68, 3380-3387.

Fratzl, P., Weinkamer, R., 2007. Nature's hierarchical materials. Progress in Materials Science 52, 1263-1334.

Gao, H., 2006. Application of fracture mechanics concepts to hierarchical biomechanics of bone and bone-like materials. International Journal of Fracture 138, 101-137.

Garcia, A.P., Pugno, N., Buehler, M.J., 2011. Superductile, wavy silica nanostructures inspired by diatom algae. Advanced Engineering Materials 13, B405-B414.

Gibson, L.J., Ashby, M.F., 1997. Cellular Solids, Structures and Properties, second ed. Cambridge University Press.

Gu, S., Lu, T.J., Evans, A.G., 2001. On the design of two-dimensional cellular metals for combined heat dissipation and structural load capacity. International Journal of Heat and Mass Transfer 44, 2163-2175.

Hyun, S., Torquato, S., 2002. Optimal and manufacturable two-dimensional, Kagome-like cellular solids. Journal of Materials Research 17, 137-144.

Innocenti, P., Scarpa, F., 2009. Thermal conductivity properties and heat transfer analysis of multi-re-entrant auxetic honeycomb structures. Journal of Compostie Materials 43, 2419-2439.

Lakes, R., 1993. Materials with structural hierarchy. Nature 361, 511-515.

Lu, T.J., 1999. Heat transfer efficiency of metal honeycombs. International Journal of Heat and Mass Transfer 42, 2031-2040.

Masters, I.G., Evans, K.E., 1996. Models for the elastic deformation of honeycombs. Composite Structures 35, 403-422.

Prall, D., Lakes, R. S., 1996. Properties of a chiral honeycomb with a Poisson's ratio -1. Int. J. of Mechanical Sciences 39, 305-314.

Price, T., Timbrook, R.L., 2001, Structural honeycomb panel building system, Patent number US6, 253, 530 B1. 3 July.

Pugno, N., 2006. Mimicking nacre with super-nanotubes for producing optimized super-composites. Nanotechnology 17, 5480-5484.

Pugno, N., Carpinteri, A., 2008. Design of micro-nanoscale bio-inspired hierarchical materials. Philosophical Magazine Letters 88, 397-405.

Pugno, N., Chen, Q., 2011. In plane elastic properties of hierarchical cellular solids, Engineering Procedia, Physics Engineering 10, 3026-3031.

Ruzzene, M., 2004. Vibration and sound radiation of sandwich beams with honeycomb truss core. Journal of Sound and Vibration 277, 741-763.

Scarpa, F., and Tomlinson, G., 2000. Theoretical characteristics of the vibration of sandwich plates with in-plane negative Poisson's ratio values. Journal of Sound and Vibration 230, 45-67.

Spadoni, A., Ruzzene M., Scarpa, F., 2006. Dynamic response of chiral truss-core assemblies. Journal of Intelligent Material Systems and Structures 17, 941-952.

Spadoni, A., Ruzzene, M., 2007a. Numerical and experimental analysis of the static compliance of chiral truss-core airfoils. Journal of Mechanics of Materials and Structures 2, 965-981.

Spadoni, A., Ruzzene, M., 2007b. Static aeroelastic response of chiral-core airfoils. Journal of Intelligent Material Systems and Structures18, 1067-1075.

Spadoni A., Ruzzene M., Gonella S., Scarpa F., 2009. Phononic properties of hexagonal chiral lattices. Wave Motion 46, 435-450.

Sun, Y., Chen, Q., Pugno, N., Elastic and transport properties of the tailorable multifunctional hierarchical honeycombs. In submission.

Thompson, R.W., Matthews, F.L., 1995. Load attachments for honeycomb panels in racing cars. Materials and Design 16, 131-150.

Wang, B., Wang, B., Cheng, G., 2007. Multicfunctional design of sandwich panels with Kagome-like cores. Acta Materiae Compositae Sinica 24, 109-115.

Wen, T., Tian, J., Lu, T.J., Queheillalt, D.T., Wadley, H.N.G., 2006. Forced convection in metallic honeycomb structures. International Journal of Heat and Mass Transfer 49, 3313-3324.

Wilson, S., 1990. A new face of aerospace honeycomb. Materials and Design 11, 323-326.

Zhao, Q., Kreplak, L., Buehler, M.J., 2009. Hierarchical Structure Controls Nanomechanical Properties of Vimentin Intermediate Filaments. PLoS ONE, 4, e7294. doi:10.1371/journal.pone.0007294

Chapter 5

Hierarchical fibers with a negative Poisson's ratio for tougher composites

In this chapter, a new kind of hierarchical tubes with a negative Poisson's ratio (NPR) is proposed. The first level tube is constructed by rolling up an auxetic hexagonal honeycomb. Then, substituting the arm of the auxetic sheet with the first level tube and rolling it up give the second level tube. Iteratively, we can build the Nth ($N \geq 1$) level tube. Based on the Euler beam theory, the elastic parameters of the NPR hierarchical tubes under small deformations are derived. Under longitudinal axial tension, instead of shrinking, all levels of the NPR hierarchical tubes expand in the transverse directions. Using this kind of auxetic tubes as reinforced fibers in composite materials results in a higher resistance to fiber pullout. Thus, this chapter provides a new strategy for the design of fiber reinforced hierarchical bio-inspired composites with superior pull-out mechanism and toughness. An application with super carbon nanotubes concludes the chapter.

5.1 Introduction

In the last several years, due to their special mechanical and electronical properties, hierarchical covalent 2D and 3D networks based on 1D nanostructures have attracted many research attentions. One relevant example are the carbon nanotube (CNT) netwoks, in which carbon nanotubes are covalently connected through different nanojunctions such as X-, Y- or T-shape (Terrones, 2002; Romo-Herrera et al., 2007;

Georgios, 2008; Dimitrakakis, 2008; Li et al., 2009a; Li et al., 2009b; Zsoldos, 2011), even in hierarchical ways (Pugno and Chen, 2011; Chen and Pugno, 2011; Chen and Pugno, 2012a, b, c). Coluci et al. (2006) proposed the self-similar hierarchical super carbon nanotubes (STs) and showed that they are stable and could present metallic or semiconducting behavior. Then, through the fractal method, Pugno (2006) evaluated the strength, toughness and stiffness the STs-reinforced composites and revealed that the optimized number of hierarchical levels is 2, similar to the optimization done by Nature in nacre. Then different numerical methods are applied to study the mechanical properties of the STs, such as the continuum (Wang et al., 2007a, b), molecular dynamics (Coluci et al., 2007; Qin et al., 2008) and molecular structure mechanics (Li. et al, 2008a, b) methods. These numerical simulations generally showed that the moduli of the STs were almost independent of the chirality of the ST, slightly affected by its arm tube chirality and determined mainly by the arm tube aspect ratio (Li. et al, 2008c) and that with the increase of the hierarchical level the stiffness and modulus of the STs reduce significantly. Through theoretical analysis and finite element calculation Wang et al. (2007b) indicated that the stiffness reduction was mainly caused by radial shrinking of STs. The deformation of the STs can be greatly decreased if the shrinking is suppressed, therefore, they suggested filling the STs with a matrix, i.e., emphasizing the importance of the STs-reinforced composites as initially proposed by Pugno (2006).

With respect of their disadvantageous shrinking, that normal STs under tension display, the concept of negative Poisson's ratio (NPR) could also be introduced if we appropriately modify the geometrical structures of the super tubes. It is well known that under tension, instead of shrinking, the NPR materials will expand in the directions perpendicular to the loading direction and could thus have some interesting properties, when used as fiber-reinforced cement in a composite, such as enhanced toughness, improved shear stiffness, higher pull-out resistance and so on (Xu et al., 1999; Evans and Alderson, 2000; Yang et al., 2004; Greaves et al. 2011).

In this chapter, combining the peculiar properties that super tubes show and the auxetic characteristics of NPR materials, a new hierarchical structure, hierarchical

tubes with a negative Poisson's ratio, is proposed. Based on the Euler beam theory, the elastic parameters of the NPR hierarchical tubes under small deformations are calculated. Such auxetic hierarchical fibers are ideal to increase pull-out resistance and thus toughness of composites.

5.2 Hierarchical structures with negative Poisson's ratio

5.2.1 Design of hierarchical NPR tubes

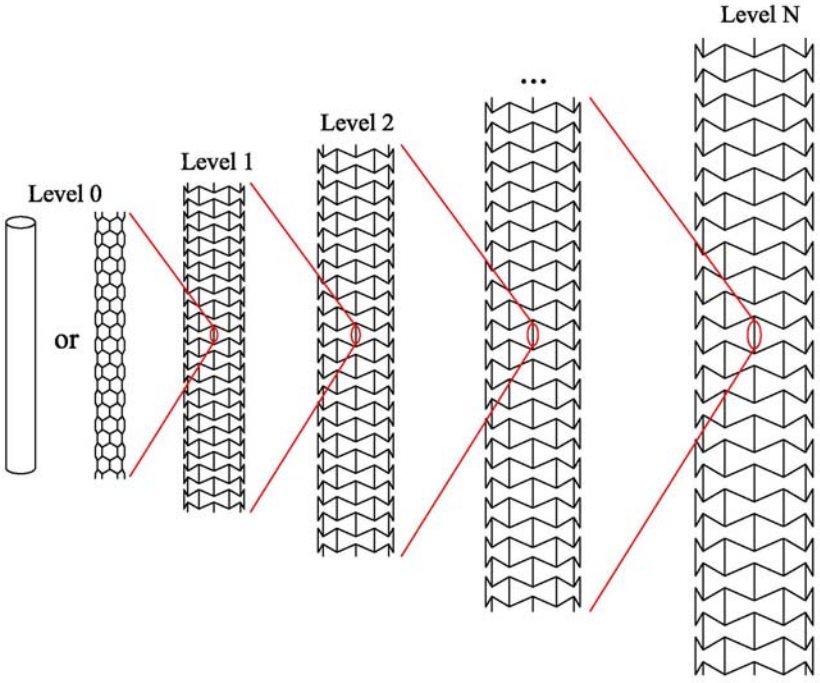

Fig. 5.1 Schematic of the *N*-level hierarchical tube with negative Poisson's ratio

Fig. 5.1 shows the schematic of a *N*-level ($N \geq 1$) hierarchical tube with negative Poisson's ratio. The *N*-level ($N \geq 1$) hierarchical tube is fabricated through iterating *N*

times a process, rolling a NPR sheet to a tube along the *x*-axis, see Figs. 5.1 and 5.2a.

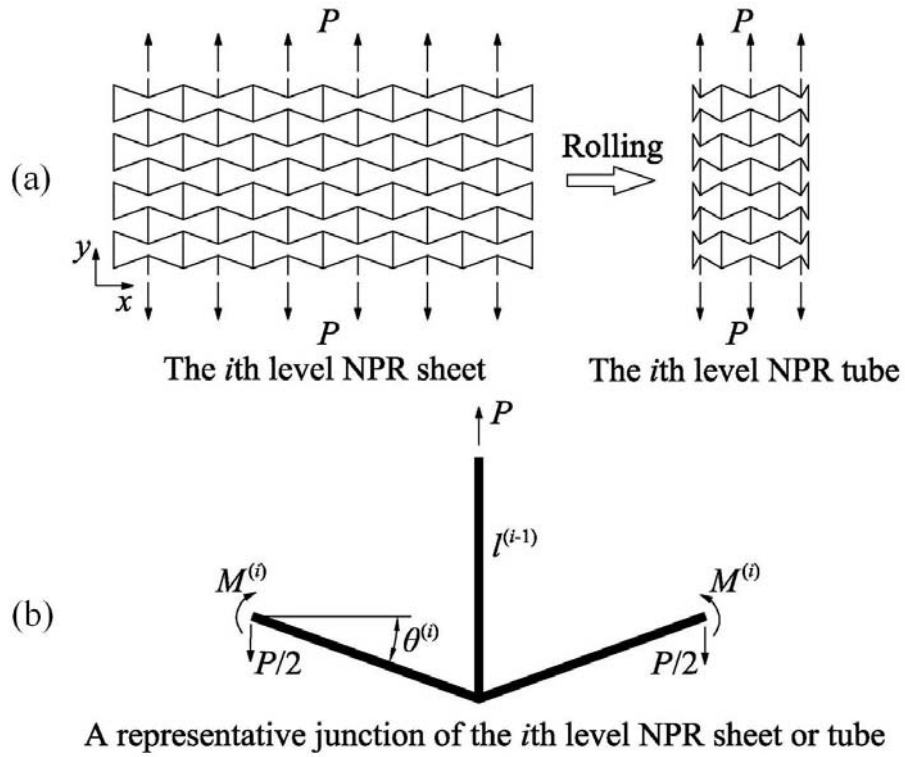

Fig. 5.2 (a) Schematic of the *i*th ($1 \le i \le N$) level NPR sheet and the corresponding *i*th ($1 \le i \le N$) level NPR tube made by rolling the NPR sheet; (b) the force diagram of a representative junction of the *i*th ($1 \le i \le N$) level NPR sheet or tube subject to the *y*-axis tension

At first, based on the considered 1D nanostructure (e.g. a solid nanorod or a thin hollow cylinder, such as CNT) the first level NPR sheet that mimicks the NPR hexagonal honeycomb is constructed. Then, rolling up the first level NPR sheet gives the first level NPR tube. The second level NPR tube is constructed by substituting the arm tube of the first level NPR sheet with the first level NPR tube and then rolling it up. Iteratively, repeating the above process N times, we can build the Nth level tube. A representative junction of the *i*th ($1 \le i \le N$) level NPR sheet or tube is shown in Fig. 5.2b, in which $l^{(i-1)}$ is the length of the arms and $-30^\circ < \theta^{(i)} < 0^\circ$.

5.2.2 Elasticity of the hierarchical NPR tubes

Based on the Euler beam theory, Wang et al. (2007b) derived the equivalent elastic parameters of the STs (positive Poisson's ratio) from that of the arm tubes and verified the results through finite element simulations. Instead of the Young's modulus E, they adopted a parameter $E\beta$ to describe the equivalent modulus of the CNT and STs, in which β is the thickness to diameter ratio of these thin hollow cylinder tubes. Similarly, in the following we analytically study the elastic moduli of the hierarchical NPR tubes shown in Fig. 5.2a.

The level 1 NPR tube

At first, we analyze the level 1 hierarchical NPR sheet and tube under uniaxial tension p in the direction y, in which the fundamental unit (level 0) is a solid nanorod or a thin hollow cylinder such as a CNT (Fig. 5.2a). From the force diagram of the representative junction shown in Fig. 5.2b it is evident that

$$M^{(1)} = \frac{p}{4} l^{(0)} \cos\theta^{(1)} \tag{5.1}$$

in which $M^{(1)}$ is the bending moment and $l^{(0)}$ is the arm length. If the fundamental unit (level 0) is a solid nanorod, we have

$$\begin{cases} A^{(0)} = \dfrac{1}{4}\pi\left(d^{(0)}\right)^2 \\ I^{(0)} = \dfrac{1}{64}\pi\left(d^{(0)}\right)^4 \end{cases} \tag{5.2}$$

in which $d^{(0)}$, $A^{(0)}$ and $I^{(0)}$ are its diameter, cross section area and inertia moment. If the fundamental unit (level 0) is a thin hollow cylinder, such as a CNT, denoting its equivalent thickness as $t^{(0)}$, we have (Wang et al., 2007b)

$$\begin{cases} A^{(0)} = \pi\left(d^{(0)}\right)^2 \beta^{(0)} \\ I^{(0)} = \dfrac{1}{8}\pi\left(d^{(0)}\right)^4 \beta^{(0)} \end{cases} \tag{5.3}$$

in which $d^{(0)}$, $A^{(0)}$ and $I^{(0)}$ are its equivalent diameter, cross section area, inertia moment and $\beta^{(0)} = t^{(0)}/d^{(0)}$ is the thickness-to-diameter ratio.

To analyze the level 1 NPR sheet and tube, we analyze the first level representative junction (Fig. 5.2b). Its lengths along the *x*-axis and *y*-axis are $l_x^{(1)} = 2\cos\theta^{(1)} l^{(0)}$ and $l_y^{(1)} = \left(1+\sin\theta^{(1)}\right) l^{(0)}$. The elongations along the two directions can be obtained through structural analysis; we find:

$$\begin{aligned}
\Delta l_x^{(1)} &= \frac{p l^{(0)}}{E^{(0)} A^{(0)}} \sin\theta^{(1)} \cos\theta^{(1)} - \frac{p\left(l^{(0)}\right)^3}{12 E^{(0)} I^{(0)}} \sin\theta^{(1)} \cos\theta^{(1)} \\
\Delta l_y^{(1)} &= \frac{p l^{(0)}}{E^{(0)} A^{(0)}} \left(1 + \frac{1}{2}\sin^2\theta^{(1)}\right) + \frac{p\left(l^{(0)}\right)^3}{24 E^{(0)} I^{(0)}} \cos^2\theta^{(1)}
\end{aligned} \tag{5.4}$$

in which $E^{(0)}$ is the Young's modulus of the fundamental unit (level 0). Then, the equivalent strains along the two directions can be easily calculated as

$$\varepsilon_x^{(1)} = \frac{\Delta l_x^{(1)}}{l_x^{(1)}} = \frac{p\sin\theta^{(1)}}{2E^{(0)}} \left(\frac{1}{A^{(0)}} - \frac{\left(l^{(0)}\right)^2}{12 I^{(0)}} \right) = \begin{cases} \dfrac{2p\sin\theta^{(1)}}{3E^{(0)}\pi\left(d^{(0)}\right)^2} \left(3 - 4\left(\alpha^{(0)}\right)^2\right) & \text{for the solid nanorod} \\ \dfrac{p\sin\theta^{(1)}}{6E^{(0)}\pi\left(d^{(0)}\right)^2 \beta^{(0)}} \left(3 - 2\left(\alpha^{(0)}\right)^2\right) & \text{for the thin hollow cylinder} \end{cases} \tag{5.5}$$

$$\begin{aligned}
\varepsilon_y^{(1)} &= \frac{\Delta l_y^{(1)}}{l_y^{(1)}} = \frac{p}{E^{(0)}\left(1+\sin\theta^{(1)}\right)} \left(\frac{1 + 1/2\sin^2\theta^{(1)}}{A^{(0)}} + \frac{\left(l^{(0)}\right)^2 \cos^2\theta^{(1)}}{24 I^{(0)}} \right) \\
&= \begin{cases} \dfrac{4p}{E^{(0)}\pi\left(d^{(0)}\right)^2} \dfrac{1 + 1/2\sin^2\theta^{(1)} + 2/3\left(\alpha^{(0)}\right)^2 \cos^2\theta^{(1)}}{1+\sin\theta^{(1)}} & \text{for the solid nanorod} \\ \dfrac{p}{E^{(0)}\pi\left(d^{(0)}\right)^2 \beta^{(0)}} \dfrac{1 + 1/2\sin^2\theta^{(1)} + 1/3\left(\alpha^{(0)}\right)^2 \cos^2\theta^{(1)}}{1+\sin\theta^{(1)}} & \text{for the thin hollow cylinder} \end{cases}
\end{aligned} \tag{5.6}$$

in which $\alpha^{(0)} = l^{(0)}/d^{(0)}$ is the aspect ratio of the level 0 arms. Thus, the equivalent Poisson's ratio $\nu^{(1)}$ is calculated as

$$\nu^{(1)} = -\frac{\varepsilon_x^{(1)}}{\varepsilon_y^{(1)}}$$
$$= \begin{cases} \dfrac{1}{6}\sin\theta^{(1)}\left(4\left(\alpha^{(0)}\right)^2 - 3\right)\dfrac{1+\sin\theta^{(1)}}{1+1/2\sin^2\theta^{(1)} + 2/3\left(\alpha^{(0)}\right)^2\cos^2\theta^{(1)}} & \text{for the solid nanorod} \\ \dfrac{1}{6}\sin\theta^{(1)}\left(2\left(\alpha^{(0)}\right)^2 - 3\right)\dfrac{1+\sin\theta^{(1)}}{1+1/2\sin^2\theta^{(1)} + 1/3\left(\alpha^{(0)}\right)^2\cos^2\theta^{(1)}} & \text{for the thin hollow cylinder} \end{cases} \quad (5.7)$$

The level 1 NPR sheet with size $L_x^{(1)} \times L_y^{(1)}$ is constituted by repeating the representative junction (Fig. 5.2b) in its plane $m^{(1)}$ times along the *x*-axis and $n^{(1)}$ times along the *y*-axis (Fig. 5.2a). We treat it as a plate with equivalent thickness $t^{(1)}$, Young's modulus $E^{(1)}$ and Poisson's ratio $\nu^{(1)}$. Rolling the level 1 NPR sheet, with direction *y* as longitudinal axis, gives the level 1 NPR tube. From the equivalence between the circumference of the level 1 NPR tube and the width $L_x^{(1)}$ of the level 1 NPR sheet, it is easy to calculate the equivalent diameter $d^{(1)}$ of the level 1 NPR tube

$$d^{(1)} = L_x^{(1)}/\pi = m^{(1)} l_x^{(1)}/\pi = 2m^{(1)} l^{(0)} \cos\theta^{(1)}/\pi \quad (5.8)$$

Then, the slenderness ratio $\alpha^{(1)}$ and the thickness-to-diameter ratio $\beta^{(1)}$ become:

$$\alpha^{(1)} = l^{(1)}/d^{(1)} = n^{(1)} l_y^{(1)}/d^{(1)} = n^{(1)}\left(1+\sin\theta^{(1)}\right)\pi/\left(2m^{(1)}\cos\theta^{(1)}\right) \quad (5.9)$$

$$\beta^{(1)} = t^{(1)}/d^{(1)} \quad (5.10)$$

where $l^{(1)}$ is the length of the level 1 NPR tube.

Except for the NPR tubes with very small diameters, the slight change of angles between the arms due to rolling can be ignored. Thus the results obtained for the level 1 NPR sheet are easily extended to the level 1 NPR tube. Accordingly, the total deformation $\Delta L_y^{(1)}$ along the length direction of the level 1 NPR tube can be expressed as:

$$\Delta L_y^{(1)} = n^{(1)}\Delta l_y^{(1)} = n^{(1)}\varepsilon_y^{(1)}\left(1+\sin\theta^{(1)}\right)l^{(0)}$$
$$= \begin{cases} \dfrac{4n^{(1)}pl^{(0)}}{E^{(0)}\pi\left(d^{(0)}\right)^2}\left(1+1/2\sin^2\theta^{(1)}+2/3\left(\alpha^{(0)}\right)^2\cos^2\theta^{(1)}\right) & \text{for the solid nanorod} \\ \dfrac{n^{(1)}pl^{(0)}}{E^{(0)}\pi\left(d^{(0)}\right)^2\beta^{(0)}}\left(1+1/2\sin^2\theta^{(1)}+1/3\left(\alpha^{(0)}\right)^2\cos^2\theta^{(1)}\right) & \text{for the thin hollow cylinder} \end{cases} \tag{5.11}$$

Thus the tensional rigidity $k_y^{(1)}$ of the level 1NPR tube is

$$k_y^{(1)} = \frac{m^{(1)}p}{\Delta L_y^{(1)}}$$
$$= \begin{cases} \dfrac{m^{(1)}E^{(0)}\pi d^{(0)}}{4n^{(1)}\alpha^{(0)}}\dfrac{1}{1+1/2\sin^2\theta^{(1)}+2/3\left(\alpha^{(0)}\right)^2\cos^2\theta^{(1)}} & \text{for the solid nanorod} \\ \dfrac{m^{(1)}E^{(0)}\pi d^{(0)}\beta^{(0)}}{n^{(1)}\alpha^{(0)}}\dfrac{1}{1+1/2\sin^2\theta^{(1)}+1/3\left(\alpha^{(0)}\right)^2\cos^2\theta^{(1)}} & \text{for the thin hollow cylinder} \end{cases} \tag{5.12}$$

Then, the axial rigidity of the level 1 NPR tube can be obtained as

$$E^{(1)}A^{(1)} = k_y^{(1)}l^{(1)} = k_y^{(1)}n^{(1)}l^{(0)}\left(1+\sin\theta^{(1)}\right)$$
$$= \begin{cases} \dfrac{m^{(1)}E^{(0)}\pi\left(d^{(0)}\right)^2}{4}\dfrac{1+\sin\theta^{(1)}}{1+1/2\sin^2\theta^{(1)}+2/3\left(\alpha^{(0)}\right)^2\cos^2\theta^{(1)}} & \text{for the solid nanorod} \\ m^{(1)}E^{(0)}\pi\left(d^{(0)}\right)^2\beta^{(0)}\dfrac{1+\sin\theta^{(1)}}{1+1/2\sin^2\theta^{(1)}+1/3\left(\alpha^{(0)}\right)^2\cos^2\theta^{(1)}} & \text{for the thin hollow cylinder} \end{cases} \tag{5.13}$$

that is to say,

$$\frac{E^{(1)}A^{(1)}}{E^{(0)}A^{(0)}} = \begin{cases} m^{(1)}\dfrac{1+\sin\theta^{(1)}}{1+1/2\sin^2\theta^{(1)}+2/3\left(\alpha^{(0)}\right)^2\cos^2\theta^{(1)}} & \text{for the solid nanorod} \\ m^{(1)}\dfrac{1+\sin\theta^{(1)}}{1+1/2\sin^2\theta^{(1)}+1/3\left(\alpha^{(0)}\right)^2\cos^2\theta^{(1)}} & \text{for the thin hollow cylinder} \end{cases} \tag{5.14}$$

in which $A^{(1)} = \pi\left(d^{(1)}\right)^2 \beta^{(1)}$ is the equivalent cross section area of the level 1 NPR tube.

The bending rigidity of the level 1 NPR tube can be expressed as (Wang et al., 2007b)

$$E^{(1)} I^{(1)} = \frac{1}{8}\left(d^{(1)}\right)^2 E^{(1)} A^{(1)} \tag{5.15}$$

Substituting the expression $A^{(1)} = \pi\left(d^{(1)}\right)^2 \beta^{(1)}$ into Eq. (5.13) gives the equivalent modulus $E^{(1)}\beta^{(1)}$ of the level 1 tube. If the fundamental unit (level 0) is the solid nanorod,

$$\frac{E^{(1)}\beta^{(1)}}{E^{(0)}} = \frac{\pi^2}{m^{(1)}\left(\alpha^{(0)}\right)^2} \frac{1+\sin\theta^{(1)}}{1+1/2\sin^2\theta^{(1)} + 2/3\left(\alpha^{(0)}\right)^2\cos^2\theta^{(1)}} \frac{1}{16\cos^2\theta^{(1)}} \tag{5.16}$$

or, if the fundamental unit (level 0) is the thin hollow cylinder, we have

$$\frac{E^{(1)}\beta^{(1)}}{E^{(0)}\beta^{(0)}} = \frac{\pi^2}{m^{(1)}\left(\alpha^{(0)}\right)^2} \frac{1+\sin\theta^{(1)}}{1+1/2\sin^2\theta^{(1)} + 1/3\left(\alpha^{(0)}\right)^2\cos^2\theta^{(1)}} \frac{1}{4\cos^2\theta^{(1)}} \tag{5.17}$$

The level N NPR tube

The elastic parameters of any level N ($N \geq 1$) NPR tube can be recursively derived by repeating the analysis reported in section 2.2.1.

About the Poisson's ratio of the level N tube, similar to Eq. (5.7), if the fundamental unit (level 0) is the solid nanorod,

$$\nu^{(N)} = \begin{cases} \frac{1}{6}\sin\theta^{(N)}\left(4\left(\alpha^{(N-1)}\right)^2 - 3\right)\frac{1+\sin\theta^{(N)}}{1+1/2\sin^2\theta^{(N)} + 2/3\left(\alpha^{(N-1)}\right)^2\cos^2\theta^{(N)}} & N = 1 \\ \frac{1}{6}\sin\theta^{(N)}\left(2\left(\alpha^{(N-1)}\right)^2 - 3\right)\frac{1+\sin\theta^{(N)}}{1+1/2\sin^2\theta^{(N)} + 1/3\left(\alpha^{(N-1)}\right)^2\cos^2\theta^{(N)}} & N \geq 2 \end{cases} \tag{5.18}$$

or if the fundamental unit (level 0) is the thin hollow cylinder,

$$\nu^{(N)} = \frac{1}{6}\sin\theta^{(N)}\left(2\left(\alpha^{(N-1)}\right)^2 - 3\right)\frac{1+\sin\theta^{(N)}}{1+1/2\sin^2\theta^{(N)} + 1/3\left(\alpha^{(N-1)}\right)^2\cos^2\theta^{(N)}} \quad N \geq 1 \tag{5.19}$$

where, $-30^\circ < \theta^{(N)} < 0^\circ$ and

$$\alpha^{(N-1)} = l^{(N-1)}/d^{(N-1)} = \begin{cases} l^{(0)}/d^{(0)} & N=1 \\ n^{(N-1)}\left(1+\sin\theta^{(N-1)}\right)\pi \Big/ \left(2m^{(N-1)}\cos\theta^{(N-1)}\right) & N \geq 2 \end{cases} \tag{5.20}$$

is the slenderness ratio of the arms of the *N*th level NPR tube.

With respect to the axial rigidity $E^{(N)}A^{(N)}$ of the level N NPR tube, if the fundamental unit (level 0) is the solid nanorod, from Eq. (5.14) it is easy to obtain that

$$\frac{E^{(N)}A^{(N)}}{E^{(0)}A^{(0)}} = \begin{cases} C_1 & N=1 \\ C_1 \prod_{i=2}^{N} \left(m^{(i)} \dfrac{1+\sin\theta^{(i)}}{1+1/2\sin^2\theta^{(i)} + 1/3\left(\alpha^{(i-1)}\right)^2 \cos^2\theta^{(i)}} \right) & N \geq 2 \end{cases} \tag{5.21}$$

in which $C_1 = m^{(1)} \dfrac{1+\sin\theta^{(1)}}{1+1/2\sin^2\theta^{(1)} + 2/3\left(\alpha^{(0)}\right)^2 \cos^2\theta^{(1)}}$; or if the fundamental unit (level 0) is the thin hollow cylinder,

$$\frac{E^{(N)}A^{(N)}}{E^{(0)}A^{(0)}} = \prod_{i=1}^{N} \left(m^{(i)} \frac{1+\sin\theta^{(i)}}{1+1/2\sin^2\theta^{(i)} + 1/3\left(\alpha^{(i-1)}\right)^2 \cos^2\theta^{(i)}} \right) \tag{5.22}$$

where, $-30^\circ < \theta^{(i)} < 0^\circ$ and

$$\alpha^{(i-1)} = l^{(i-1)}/d^{(i-1)} = \begin{cases} l^{(0)}/d^{(0)} & i=1 \\ n^{(i-1)}\left(1+\sin\theta^{(i-1)}\right)\pi \Big/ \left(2m^{(i-1)}\cos\theta^{(i-1)}\right) & i=2,\cdots,N \end{cases} \tag{5.23}$$

is the slenderness ratio of the arms of the *i*th level NPR tube.

Similar to Eq. (5.15), the bending rigidity $E^{(N)}I^{(N)}$ of the level N NPR tube is

$$E^{(N)}I^{(N)} = \frac{1}{8}\left(d^{(N)}\right)^2 E^{(N)}A^{(N)} \tag{5.24}$$

in which $d^{(N)} = L_x^{(N)}/\pi = 2m^{(N)}l^{(N-1)}\cos\theta^{(N)}/\pi$ is the equivalent diameter of the level N NPR tube.

It is also easy to get that, if the fundamental unit (level 0) is the solid nanorod,

$$\frac{E^{(N)}\beta^{(N)}}{E^{(0)}}=\begin{cases} C_2 & N=1 \\ C_2\prod_{i=2}^{N}\left(\dfrac{\pi^2}{m^{(i)}\left(\alpha^{(i-1)}\right)^2}\dfrac{1+\sin\theta^{(i)}}{1+1/2\sin^2\theta^{(i)}+1/3\left(\alpha^{(i-1)}\right)^2\cos^2\theta^{(i)}}\dfrac{1}{4\cos^2\theta^{(i)}}\right) & N\geq 2 \end{cases} \tag{5.25}$$

in which $C_2=\dfrac{\pi^2}{m^{(1)}\left(\alpha^{(0)}\right)^2}\dfrac{1+\sin\theta^{(1)}}{1+1/2\sin^2\theta^{(1)}+2/3\left(\alpha^{(0)}\right)^2\cos^2\theta^{(1)}}\dfrac{1}{16\cos^2\theta^{(1)}}$; or if the fundamental unit (level 0) is the thin hollow cylinder,

$$\frac{E^{(N)}\beta^{(N)}}{E^{(0)}\beta^{(0)}}=\prod_{i=1}^{N}\left(\frac{\pi^2}{m^{(i)}\left(\alpha^{(i-1)}\right)^2}\frac{1+\sin\theta^{(i)}}{1+1/2\sin^2\theta^{(i)}+1/3\left(\alpha^{(i-1)}\right)^2\cos^2\theta^{(i)}}\frac{1}{4\cos^2\theta^{(i)}}\right) \tag{5.26}$$

Effects of the parameters $\theta^{(N)}$, $\alpha^{(N-1)}$ and N

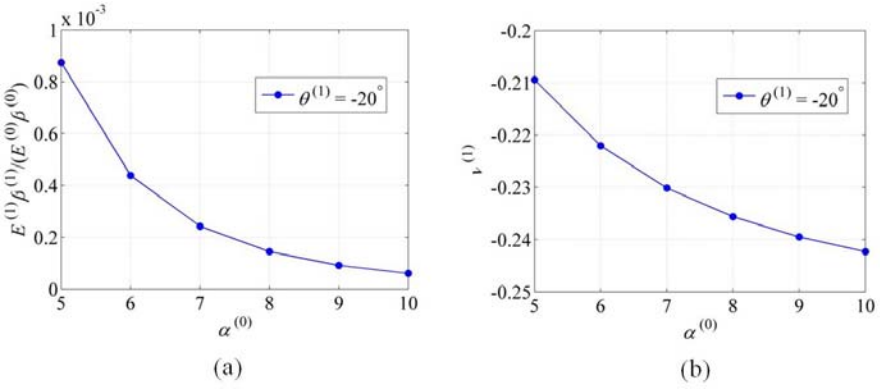

Fig. 5.3 Schematics of (a) $E^{(1)}\beta^{(1)}$ *vs* $\alpha^{(0)}$ and (b) $\nu^{(1)}$ *vs* $\alpha^{(0)}$

To see the effects of $\theta^{(N)}$, $\alpha^{(N-1)}$ and N on the elastic parameters of the level N NPR tube, we use the following examples, considering the NPR tubes with CNT as fundamental unit. With respect to the effects of $\alpha^{(N-1)}$ on $E^{(N)}\beta^{(N)}$ and $\nu^{(N)}$, the parameters $N=1$, $\theta^{(1)}=-20^{\circ}$, $m^{(1)}=10$, $\alpha^{(0)}=5-10$ are adopted and the related results are reported in Fig. 5.3. From Fig. 5.3 we can see that both $E^{(1)}\beta^{(1)}$ and $\nu^{(1)}$ decrease with

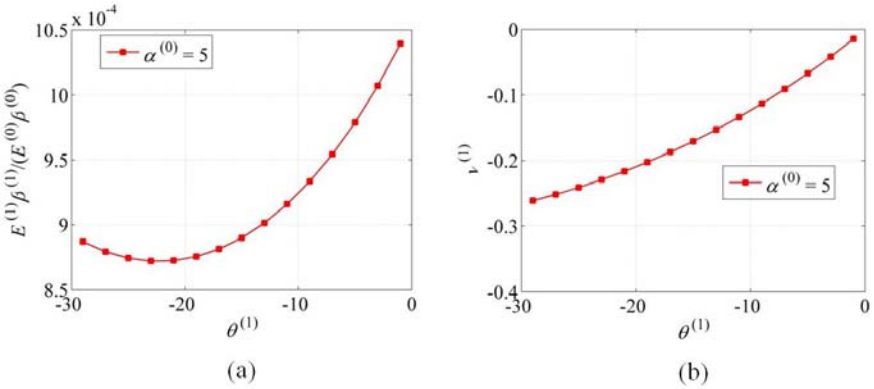

Fig. 5.4 Schematics of (a) $E^{(1)}\beta^{(1)}$ *vs* $\theta^{(1)}$ and (b) $\nu^{(1)}$ *vs* $\theta^{(1)}$

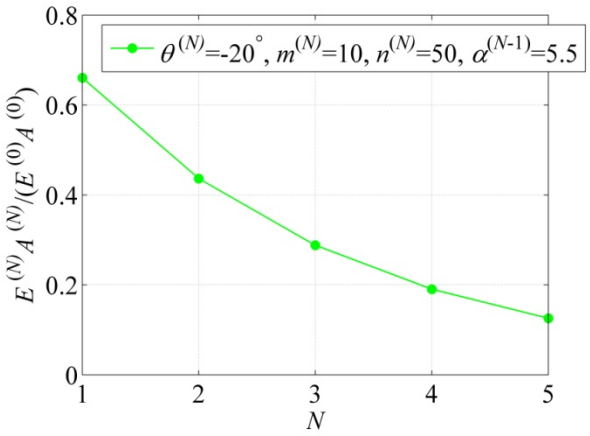

Fig. 5.5 Schematic of the axial rigidity $E^{(N)}A^{(N)}$ *vs* the hierarchical level N

the increase of $\alpha^{(0)}$. Similarly, about the effects of $\theta^{(N)}$ on $E^{(N)}\beta^{(N)}$ and $\nu^{(N)}$, the parameters $N=1$, $\alpha^{(0)}=5$, $m^{(1)}=10$, $\theta^{(1)}=-30^{\circ}-0^{\circ}$ are considered. The related results are shown in Fig. 5.4. It can be seen that $\nu^{(1)}$ increases with the increase of $\theta^{(1)}$, however, $E^{(1)}\beta^{(1)}$ at first decreases with the increase of $\theta^{(1)}$ until about -22° and after that it increases with the increase of $\theta^{(1)}$, showing an interesting minimum, see Fig. 5.4a. For higher level N ($N>1$), the effects of $\theta^{(N)}$ on $E^{(N)}\beta^{(N)}$ and $\nu^{(N)}$ are similar to that of level 1. Finally, about the effect of the hierarchical level N on the axial rigidity $E^{(N)}A^{(N)}$, the following parameters are considered: $N=1-5$, $\theta^{(N)}=-20^{\circ}$, $m^{(N)}=10$,

$n^{(N)} = 50$, $\alpha^{(N-1)} = 5.5$. The related results are displayed in Fig. 5.5. We can see that axial rigidity $E^{(N)}A^{(N)}$ decreases with the increase of *N*. Also for higher level *N* ($N > 1$) NPR tube the effects of the parameters $\theta^{(N)}$, $\alpha^{(N-1)}$ and *N* are similar to those of the level 1 NPR tube. Note that with the increase of the hierarchical level *N* the equivalent modulus $E^{(N)}\beta^{(N)}$ of the level *N* NPR tube sharply decreases, as can be easily seen from Eqs. (5.25) or (5.26).

5.3 Conclusions

A new kind of hierarchical tubes with negative Poisson's ratio is proposed in this chapter. The equivalent elastic parameters of the NPR hierarchical tubes under small deformations are derived through the Euler beam theory. The results show that both the angles between the arms and the slenderness ratio of the arms have great influences on the equivalent modulus, axial rigidity and Poisson's ratio of the hierarchical NPR tube and can thus be tuned to match the requirement of a specific application. Under longitudinal axial tension, all levels of the negative Poisson's ratio hierarchical tubes will expand in the transverse directions rather than shrink. Using these NPR tubes as reinforced fibers in composite materials can result in a higher resistance to fiber pullout and thus provides new strategies for the design of the fiber reinforced tougher hierarchical bio-inspired composites. It should be noted that the theory in this chapter is limited to the hierarchical NPR tubes with slender arms in small bending deformations.

References

Chen, Q., Pugno, N., 2011. Modeling the elastic anisotropy of woven hierarchical tissues. Composites Part B: Engineering 42, 2030-2037.

Chen, Q., Pugno, N., 2012a. Mechanics of hierarchical 3-D nanofoams. Europhysics Letters 97, 26002.

Chen, Q., Pugno, N., 2012b. In-plane elastic buckling of hierarchical honeycomb materials, European Journal of Mechanics A/Solids 34, 120-129.

Chen, Q., Pugno, N., 2012c. Competition between in-plane buckling and bending collapses in nano-honeycombs. Europhysics Letters 98, 16005.

Coluci, V. R., Galvao D.S., Jorio, A., 2006. Geometric and electronic structure of carbon nanotube networks: 'super'-carbon nanotubes. Nanotechnology 17, 617-621.

Coluci, V.R., Pugno, N., Dantas, S.O., Galvao, D.S., Jorio, A., 2007. Atomistic simulations of the mechanical properties of 'super' carbon nanotubes. Nanotechnology 18, 335702.

Dimitrakakis, G.K., Tylianakis, E., Froudakis, G.E., 2008. Pillared Graphene: A New 3-D Network Nanostructure for Enhanced Hydrogen Storage. Nano Letters 8, 3166-3170.

Evans, K.E., Alderson, A., 2000. Auxetic materials: Functional materials and structures from lateral thinking. Advanced Materials 12, 617-628.

Greaves, G. N., Greer, A. L., Lakes, R.S., Rouxel, T., 2011. Poisson's ratio and modern materials. Nature Materials 10, 823-837.

Li, Y., Qiu, X.M., Yang, F., Wang, X.S., Yin, Y.J., 2008a. Ultra-high sensitivity of super carbon-nanotube-based mass and strain sensors. Nanotechnology 19, 165502.
Li, Y., Qiu, X.M., Yang, F., Wang, X.S., Yin, Y.J., 2008b. The effective modulus of super carbon nanotubes predicted by molecular structure mechanics. Nanotechnology 19, 225701.

Li, Y., Qiu, X.M., Yang, F., Wang, X.S., Yin, Y.J., Fan, Q.S., 2008c. A comprehensive study on the mechanical properties of super carbon nanotubes. Journal of Physics D: Applied Physics 41, 155423.

Li , Y., Qiu, X., Yang, F., Yin, Y., Fan, Q., 2009a. Stretching-dominated deformation mechanism in a super square carbon nanotube network. Carbon 47, 812-819.

Li , Y., Qiu, X., Yang, F., Yin, Y., Fan, Q., 2009b. The specific heat of carbon nanotube networks and their potential applications. Journal of Physics D: Applied Physics 42, 155405.

Pugno, N.M., 2006. Mimicking nacre with super-nanotubes for producing optimized super-composites. Nanotechnology 17, 5480-5484.

Pugno, N., Chen, Q., 2011. In plane elastic properties of hierarchical cellular solids, Engineering Procedia, Physics Engineering 10, 3026-3031.

Qin, Z., Feng, X.Q., Zou, J., Yin, Y.J., Yu, S.W., 2008. Molecular Dynamics Simulations of Deformation and Rupture of Super Carbon Nanotubes Under Tension. Journal of Nanoscience and Nanotechnology 8, 6274-6282.

Romo-Herrera, J. M., Terrones, M., Terrones, H., Dag, S., Meunier, V., 2007. Covalent 2D and 3D Networks from 1D Nanostructures: Designing New Materials, Nano Letters 7, 570-576.

Terrones, M., Banhart, F., Grobert, N., Charlier, J.C., Terrones, H., Ajayan, P.M., 2002. Molecular Junctions by Joining Single-Walled Carbon Nanotubes. Physical Review Letters 89, 075505.

Wang, M., Qiu, X.M., Zhang, X., 2007a. Mechanical properties of super honeycomb structures based on carbon nanotubes. Nanotechnology 18, 075711.
Wang, M., Qiu, X.M., Zhang, X., Yin, Y.J., 2007b. Equivalent parameter study of the mechanical properties of super carbon nanotubes. Nanotechnology 18, 295708.

Xu, B., Arias, F., Brittain, S.T., Zhao, X.M., Grzybowski, B., Torquato, S., Whitesides, G.M., 1999. Making negative Poisson's ratio microstructures by soft lithography. Advanced Materials 11, 1186-1189.

Yang, W., Li, Z.M., W., Shi, B.H., Xie, Yang, M.B., 2004. Review on auxetic materials. Journal of Materials Science 39, 3269-3279.

Zsoldos, I., 2011. Planar trivalent polygonal networks constructed from carbon nanotube Y-junctions. Journal of Geometry and Physics 61, 37-45.

Chapter 6

A hierarchical bridged crack model

The constitutive flexural and tensile behaviors of the discontinuous fiber reinforced brittle matrix composites are analyzed. Snap-back or snap-through instabilities exist in both cases under the assumption of rigid-plastic bridging law. Results show that with the increase of the brittleness number, a brittle to ductile transition appears for the flexural loading case but for the tensile loading case our responses calculated here always tend to be brittle with the increase of the crack length. This illustrates that for fiber reinforced brittle matrix composites size-scale effects are influenced by the loading configurations. Meanwhile, the bridged crack model is hierarchically extended through the recursive method. A two level numerical example is discussed and the results are compared with the beam of the same geometry without hierarchy. The maximum strength for the former case is larger than that of the later one, which suggests the use of hierarchy to optimize fiber-reinforced hierarchical bio-inspired materials.

6.1 Introduction

Crack growth in brittle matrix composites attracted many attentions in the past thirty years. It is a discontinuous phenomenon which can be characterized by sudden initiations or arrests of the crack propagation caused by the bridging actions of the inclusion phases or by the rise and coalescences of microcracks in the process or bridging zone. Due to these kinds of local discontinuities, snap-back and snap-through

phenomena can appear in the crack loading process. Carpinteri et al. analyzed the size-scale effects involving snap-back instabilities in different kinds of materials and conditions, such as concrete, elastic softening slabs, brittle matrix fibrous composites, strengthened beams, multi-cracked solids, etc.(Bocca et al., 1990; Bosco et al., 1990; Carpinteri and Massabo, 1997). In particular, they introduced a parameter, the brittleness number, which explicitly describes the size-scale effects of materials. Bazant (1987) investigated the snap instability at crack ligament tearing and explained its implications for fracture micromechanics. Also, the fiber bundle model is used to consider the snap-back phenomenon in quasi-brittle materials (Ren and Li, 2011) or in the hierarchical supertough nanofibers inspired by spider silks (Bosia et al., 2010). General reviews about the crack-bridging concepts are given by Bao and Suo (1992) and Cox and Marshall (1994).

Although the bridged crack model under monotonic and cyclic bending conditions have been extensively studied (Carpinteri and Massabo, 1997; Carpinteri et al., 2006), its applications to the axial tensile loading cases are not wildely discussed, and more importantly hierarchy has never been investigated. Therefore, in this chapter, based on the bridged crack model, the flexural and tensile behaviors of the discontinuous fiber reinforced brittle matrix hierarchical composites are studied. In fact, bio-inspired hierarchical materials (Lakes, 1993), especially the super-composites (Bosia et al., 2010; Pugno, 2006), are attracting increasing interests. In this regard, hierarchy suggests a due to design materials with simltaneously optimized strength, stiffness and toughness (Gao, 2006).

6.2 Bridged crack model and dimensional analysis

As shown in Fig. 6.1, the bridged crack model is schematically illustrated for the discontinuous fiber reinforced brittle matrix composites. One is for the tensile loading case (Fig. 6.1a), and the other one is for the flexural loading condition (Fig. 6.1b). The load is placed on the composite beam with a notched through thickness edged crack

and the loading process is controlled by monotonically increasing the crack length. The cracked cross section of the composite beam is shown in the right picture of Fig. 6.1a or Fig. 6.1b, in which symbols h and b denote the depth and thickness of the cross section respectively. The crack length and the normalized crack depth are denoted by a and $\xi = a/h$. The closing force P_i $(i = 1, 2, \cdots, m)$ represents the bridging actions of a discrete number of localized reinforcements, C_i is the relative localized coordinate of the reinforcement related to the bottom of the cross section and its normalized value is expressed as $\zeta_i = C_i/h$. The symbol w_i stands for the corresponding crack opening of the *i*-th reinforcement.

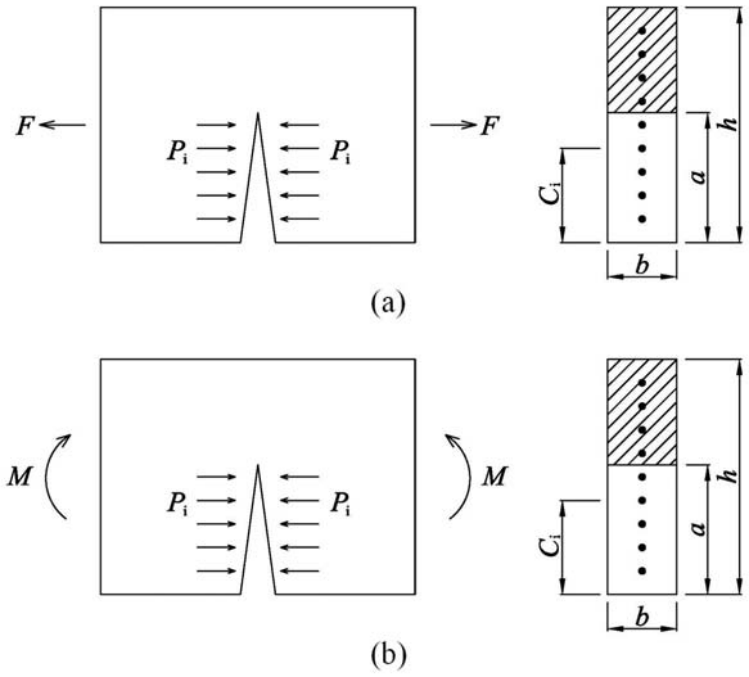

Fig. 6.1 Schemes for the discontinuous fiber reinforced brittle matrix composite under (a) tension or (b) bending

The crack propagation condition for the matrix is defined to be brittle, i.e., the crack starts to propagate when the global stress intensity factor K_I, which is a measure of the singular stress field in the crack tip vicinity, reaches the fracture

toughness K_{IC} of the matrix. A rigid-perfectly plastic bridging law relating the closing force P_i to the crack opening w_i is assumed for the reinforcements. This law is a simple model which is physically realistic for small slips that could represent both the fiber yielding and the matrix-fiber sliding. Moreover, it implies that a maximum bridging traction $P_{p_i} = A_i \sigma_y$ is defined, in which A_i is the cross section area of the *i*-th reinforcement and σ_y is the minimum between the *i*-th reinforcement yield strength and the sliding stress. Besides, low reinforcement volume ratios are considered in order that only the matrix properties control the composite elastic behavior. Here we define ρ as the total volume ratio of the reinforcements and ρ_i the single volume ratio of the *i*-th reinforcement. The constitutive flexural and tensile behaviors, which link the bending moment M to the localized rotation ϕ and the tensile force F to the local displacement $\tilde{\Delta}$, could be derived from the above introduced principles and laws.

To synthetically investigate the flexural responses and final collapse of the cross section shown in Fig. 6.1b, the dimensional analysis with respect to the bending moment M and the localized rotation ϕ can be adopted (Carpinteri and Massabo, 1997):

$$f\left(\frac{M}{K_{IC}h^{2.5}}, \phi, \frac{\rho\sigma_y h^{0.5}}{K_{IC}}, \frac{Eh^{0.5}}{K_{IC}}\right) = f\left(\tilde{M}, \phi, N_p, \tilde{E}\right) = 0 \tag{6.1}$$

in which $\tilde{M}$, $\tilde{E}$, N_p are defined in Eq. (6.1) and represent the dimensionless values of the applied bending moment M, the matrix's Young's modulus E and the reinforcement ultimate strength σ_y. Because the parameter $\tilde{E}$ is simply a constant, then Eq. (6.1) can be simplified to the following form:

$$f\left(\tilde{M}, \phi, N_p\right) = 0 \tag{6.2}$$

in which the dimensionless parameter

$$N_p = \frac{\rho\sigma_y h^{0.5}}{K_{IC}} \tag{6.3}$$

is also called brittleness number and reflects the brittleness of the composite beam.

Similarly, the dimensionless physical equation for the tensile force F and the local displacement D can be expressed as:

$$f\left(\frac{F}{K_{IC}h^{1.5}}, D, \frac{\rho\sigma_y h^{0.5}}{K_{IC}}\right) = f\left(\tilde{F}, D, N_p\right) = 0 \tag{6.4}$$

in which $\tilde{F}$ represents the dimensionless applied tensile force.

For a fixed crack length, the crack propagation tensile force F_F, i.e., the force for the crack at the onset of propagation, can be obtained through the superposition principle and the mobile equilibrium conditions:

$$K_{\mathrm{I}} = K_{1F} - \sum_{i=1}^{m} K_{1i} = \frac{F}{bh^{0.5}} Y_F\left(\xi\right) - \sum_{i=1}^{m} \frac{P_i}{bh^{0.5}} Y_P\left(\xi, \zeta_i\right) = K_{\mathrm{IC}} \tag{6.5}$$

in which K_{I} is the global crack tip stress intensity factor; K_{1F} and K_{1i} are the stress intensity factors due to the tensile force F and the generic closing forces P_i; $Y_F\left(\xi\right)$ and $Y_P\left(\xi, \zeta_i\right)$ are the dimensionless geometry functions for the tensile force F and the closing forces P_i (Appendix B). By rearranging Eq. (6.5) we get the dimensionless form of the crack propagation tensile force F_F:

$$\frac{F_F}{K_{\mathrm{IC}}bh^{0.5}} = \frac{1}{Y_F\left(\xi\right)}\left[\frac{N_{\mathrm{P}}}{\rho}\sum_{i=1}^{m}\rho_i \frac{P_i}{P_{P_i}} Y_{\mathrm{P}}\left(\xi, \zeta_i\right) + 1\right] \tag{6.6}$$

The localized displacement D at the onset of crack propagation can be calculated using the Castigliano's Theorem:

$$D = \frac{\partial u_F}{\partial F} \tag{6.7}$$

in which u_F is the strain energy of the cracked body. The relationship among u_F, the energy release rate G and the global stress intensity factor K_I has the following form:

$$u_{\mathrm{F}} = \int_0^{\xi} Gbh\mathrm{d}y = \int_0^{\xi} \frac{K_{\mathrm{I}}^2}{E} bh\mathrm{d}y \tag{6.8}$$

Combining Eqs. (6.5), (6.7) and (6.8) we obtain the localized displacement D:

$$D = \frac{\partial}{\partial F}\frac{1}{E}\int_0^{\xi}\left(K_{1F} - \sum_{i=1}^{m} K_{1i}\right)^2 bh\mathrm{d}y \tag{6.9}$$

Rearranging Eq. (6.9) gives the dimensionless form Δ of the localized displacement D:

$$\Delta = \frac{D}{h} = \frac{2K_{\mathrm{IC}}}{Eh^{0.5}}\left[\frac{F_F}{K_{\mathrm{IC}}bh^{0.5}}\int_0^{\xi} Y_F^2(\xi)\mathrm{d}y - \frac{N_P}{\rho}\sum_{i=1}^{m}\rho_i\frac{P_i}{P_{P_i}}\int_{\zeta_i}^{\xi} Y_F(y)Y_P(y,\zeta_i)\mathrm{d}y\right] \tag{6.10}$$

Similarly, we can get the dimensionless form of the crack propagation moment M_F and the corresponding localized rotation ϕ:

$$\frac{M_F}{K_{\mathrm{IC}}bh^{1.5}} = \frac{1}{Y_M(\xi)}\left[\frac{N_{\mathrm{P}}}{\rho}\sum_{i=1}^{m}\rho_i\frac{P_i}{P_{P_i}}Y_{\mathrm{P}}(\xi,\zeta_i)+1\right] \tag{6.11}$$

$$\phi = \frac{2K_{\mathrm{IC}}}{Eh^{0.5}}\left[\frac{M_F}{K_{\mathrm{IC}}h^{1.5}b}\int_0^{\xi} Y_M^2(\xi)\mathrm{d}y - \frac{N_{\mathrm{P}}}{\rho}\sum_{i=1}^{m}\rho_i\frac{P_i}{P_{P_i}}\int_{\zeta_i}^{\xi} Y_M(y)Y_P(y,\zeta_i)\mathrm{d}y\right] \tag{6.12}$$

in which $Y_M(\xi)$ and $Y_P(\xi,\zeta_i)$ are the dimensionless geometry functions for the bending moment M and the generic closing forces P_i (Appendix B).

6.3 Flexural behavior vs tensile behavior

In this part, numerical simulations for the above derived bridged crack model are analyzed. A comparison between the flexural behavior and the tensile behavior of a two layers reinforced composite beam is performed to study the influence of the brittleness number in different loading configurations.

Using the calculating procedure reported in Appendix A, the flexural and tensile behaviors of a two layers reinforced brittle matrix composite beam are analyzed respectively for different brittleness numbers. The parameters used for the composite beam are $E = 3\times10^4$ MPa, $\sigma_y = 390$ MPa, $b = 0.1$ m, $h = 0.1$ m, the number of reinforced layers is $m = 2$, the fracture toughness of the matrix $K_{IC} = 1.75$ MPa$\sqrt{\mathrm{m}}$ and $N_P = \rho\left(\sigma_y h^{0.5}/K_{IC}\right) = 0.1,\ 0.4,\ 0.6,\ 0.9$. The normalized local coordinates of the two layers reinforcements are $\xi_1 = 0.1$ and $\xi_2 = 0.2$. The initial crack length $\xi = 0.11$. From the brittleness number $N_P = \rho\left(\sigma_y h^{0.5}/K_{IC}\right)$ we can see that only the reinforcements volume ratio ρ is changing with the change of N_P. The flexural and tensile responses

of the beam are shown in Fig. 6.2 and Fig. 6.3 respectively.

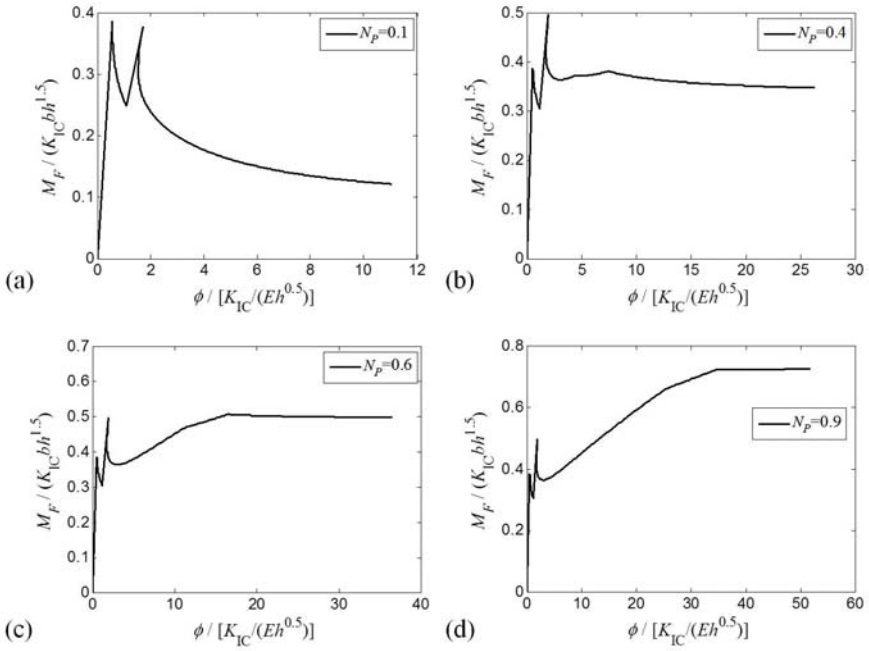

Fig. 6.2 Dimensionless bending moments *vs* normalized local rotations for a beam with two reinforcements as the brittleness number N_p varies

From Fig. 6.2 and Fig. 6.3 we can see that due to the nonlinear properties of the reinforcements snap-back and snap-through instabilities exist in both loading conditions. In Fig. 6.2 it is obvious that with the increase of the brittleness number from 0.1 to 0.9 a brittle to ductile transition appears for the bending case. But for the tensile loading case in Fig. 6.3 even though the brittleness number increases, the response of the beam always tends to be brittle with the increase of the crack length. In fact, in Fig. 6.2a to Fig. 6.2d both the two reinforcements always yield, so the ultimate moment M_u can change linearly with the brittleness number N_P. From the moment equilibrium it is easy to get the relationship $M_u \big/ \left(K_{\mathrm{IC}} bh^{1.5}\right) = N_{\mathrm{P}} \left[1-\left(\zeta_1+\zeta_2\right)/2\right]$. In Fig. 6.3a both the two reinforcements yield in the loading process while in Fig. 6.3b to Fig. 6.3d the two reinforcements do not yield although the crack length is keeping increasing, thus leading to the same tensile responses. In other words, in the

investigated tensile loading cases when the brittleness number is large enough the reinforcements do not reach their yielding strength, which means that the tensile behavior is independent of the brittleness number. The above different responses in Fig. 6.2 and Fig. 6.3 imply that size-scale effects for the discontinuous fiber reinforced composites are closely related to the loading configurations.

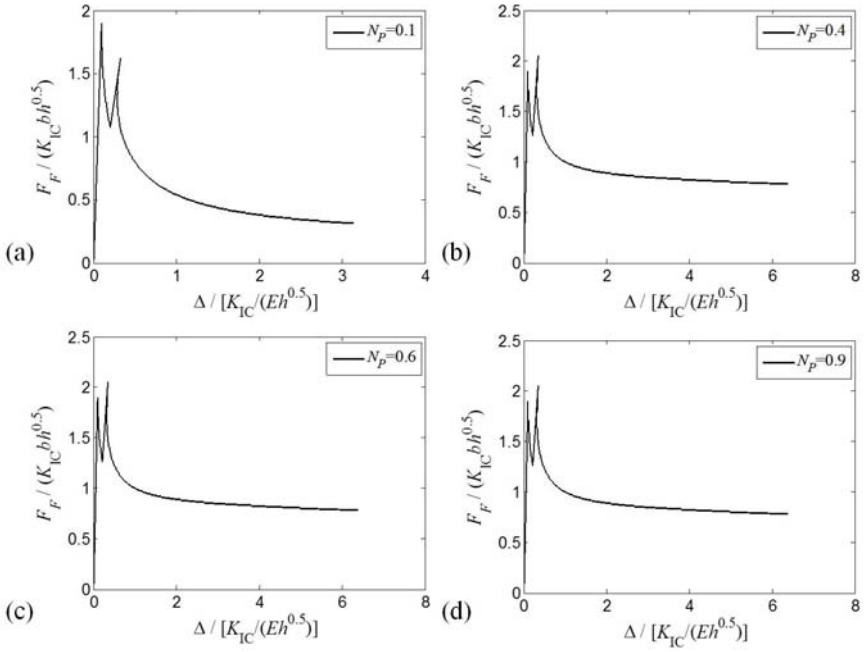

Fig. 6.3 Dimensionless tensile forces *vs* normalized localized displacements for the same beam in Fig. 6.2 as the brittleness number N_p varies

6.4 The hierarchical bridged crack model

In this section the bridged crack model is expanded to the self-similar hierarchical discontinuous fiber reinforced brittle matrix composite (Fig. 6.4), a relevant case for biological or bio-inspired nanomaterials.

6.4.1 Basic theory

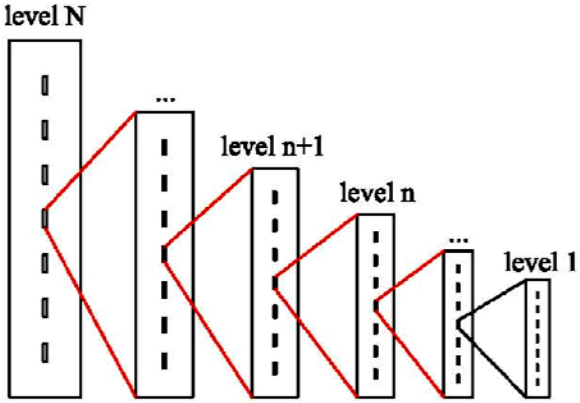

Fig. 6.4 Schematic of the self-similar hierarchical discontinuous fiber reinforced brittle matrix composite

As shown in Fig. 6.4, the definition "self-similar" implies that the whole part of the lower level is treated as the reinforcement for the higher level. For each hierarchical level the rigid-perfectly plastic bridging law is assumed and the maximum strength of the lower level is treated as the yield strength for the fiber of the next hierarchical level. Then the recursive parameters for each hierarchy can be attained accordingly.

The brittleness number for each hierarchy is

$$N_P^{(n)} = \rho_n \frac{\sigma_{yn} h_n^{0.5}}{K_{\mathrm{IC}}^{(n)}} = \begin{cases} \rho_1 \dfrac{\sigma_{y1} h_1^{0.5}}{K_{\mathrm{IC}}^{(1)}} & n = 1 \\ \rho_n \dfrac{\sigma_{\max}^{(n-1)} h_n^{0.5}}{K_{\mathrm{IC}}^{(n)}} & n \geq 2 \end{cases} \tag{6.13}$$

Here we consider the tensile behavior of the hierarchical model. Similar to Eq. (6.6), the dimensionless tensile force for each hierarchy is

$$\frac{F_F(n)}{K_{\mathrm{IC}}^{(n)} b_n h_n^{0.5}} = \frac{1}{Y_F(\xi)} \left[\frac{N_P^{(n)}}{\rho_n} \sum_{i=1}^{m} \rho_i \frac{P_i}{P_{P_i}} Y_P(\xi, \zeta_i) + 1 \right] \quad (n \geq 1) \tag{6.14}$$

And the corresponding dimensionless local displacement is

$$\Delta_n = \frac{D_n}{h_n} = \frac{2K_{\mathrm{IC}}^{(n)}}{E_n h_n^{0.5}}\left[\frac{F_F^{(n)}}{K_{\mathrm{IC}}^{(n)} b_n h_n^{0.5}}\int_0^{\xi} Y_F^2(\xi)\mathrm{d}y - \frac{N_{\mathrm{P}}^{(n)}}{\rho_n}\sum_{i=1}^{m}\rho_i \frac{P_i}{P_{P_i}}\int_{\zeta_i}^{\xi} Y_F(y) Y_P(y,\zeta_i)\mathrm{d}y\right] \quad (n \geq 1) \tag{6.15}$$

6.4.2 An example of a two levels hierarchical beam

In this section a simple example for a two level hierarchical beam is given using the hierarchical bridged crack model presented in section 4.1 and the results (Fig. 6.5a) are compared with those related to the same geometry without hierarchy (Fig. 6.5b).

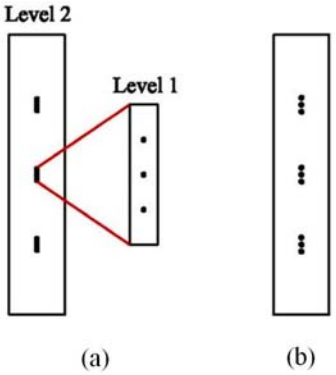

Fig. 6.5 (a) A two level self-similar hierarchical beam with 3 reinforcements; (b) the composite beam with the same geometry as that of level 2 in (a)

For level 1 of the hierarchical beam shown in Fig. 6.5a, we consider 3 layers of reinforcements which are located at $\xi = 0.25,\ 0.5,\ 0.75$ respectively. The employed parameters are $E_{m1} = 3\times10^4$ MPa, $E_1 = 2.06\times10^5$ MPa, $\sigma_{y1} = 450$ MPa, $\sigma_m = 1.43$ MPa, $b_1 = 0.001$ m, $h_1 = 0.005$ m, $n_1 = 3$ (reinforced layers), $K_{IC}^{(1)} = 1.75$ MPa$\sqrt{\mathrm{m}}$, $\rho_1 = N_P^{(1)} K_{IC}^{(1)} \big/ \left(\sigma_{y1} h_1^{0.5}\right) = 0.033$, $N_{\mathrm{P}}^{(1)} = \rho_1 \left(\sigma_{y1} h_1^{0.5}\right) \big/ K_{IC}^{(1)} = 0.6$. Using the procedure reported in Appendix A we get the tensile behavior of the level 1 beam involving the dimensionless tensile force and the normalized local displacement (Fig. 6.6).

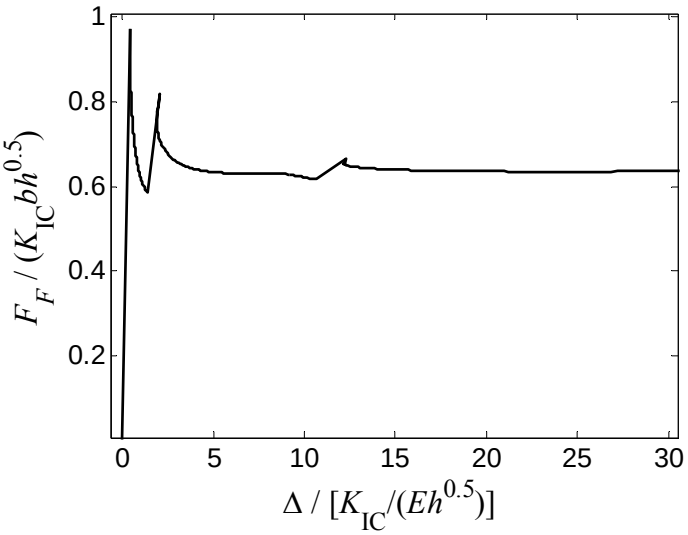

Fig. 6.6 Dimensionless tensile forces vs normalized localized displacements for hierarchical level 1 beam shown in Fig. 6.5a

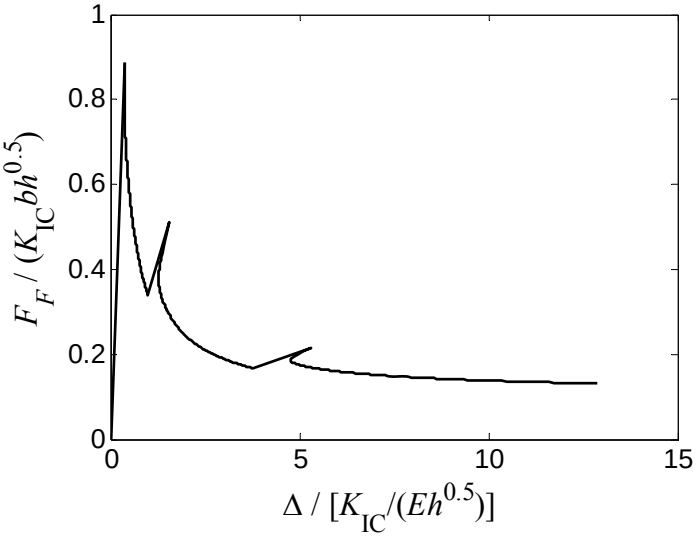

Fig. 6.7 Dimensionless tensile forces vs normalized localized displacements for hierarchical level 2 beam shown in Fig. 6.5a

Using the assumptions given in section 4.1, that connect level 1 and level 2 of the hierarchical beam, we obtain the following parameters for hierarchical level 2 (Fig. 6.5a): $E_{m2} = E_{m1} = 3\times10^4$ MPa, $E_2 = E_1\rho_1 + E_m(1-\rho_1) = 3.1\times10^4$ MPa, $n_2 = 3$, $K_{IC}^{(2)} = K_{IC}^{(1)} = 1.75$ MPa$\sqrt{\text{m}}$, $\rho_2 = n_2 b_1 h_1 / (b_2 h_2) = n_2 b_1 h_1 / (Ab_1 Ah_1) = n_2 / A^2 = \rho_1 = \rho = 3.3\%$, $b_2 = Ab_1 = 0.01$, $h_2 = Ah_1 = 0.05$, $\sigma_{y2} = \sigma_{\max}^{(1)} = F_{\max}^{(1)} / (b_1 h_1) = 0.9713 K_{IC}^{(1)} b_1 h_1^{0.5} / (b_1 h_1)$ $= 24.04$ MPa, $N_P^{(2)} = \rho_2 \sigma_{y2} h_2^{0.5} / K_{IC}^{(2)} = \rho_2 \sigma_{\max}^{(1)} h_2^{0.5} / K_{IC}^{(2)} = 0.1014$. The corresponding dimensionless tensile forces versus the normalized local displacements are depicted in Fig. 6.7.

For the beam without hierarchy shown in Fig. 6.5b which has the same geometry of the 2 hierarchical level beam shown in Fig. 6.5a, we consider 9 reinforcements located at $\xi = 0.225$, 0.25, 0.275; 0.475, 0.5, 0.525; 0.725, 0.75, 0.775 respectively. Referring to Appendix A, we get its fracture response under the tensile loading (Fig. 6.8).

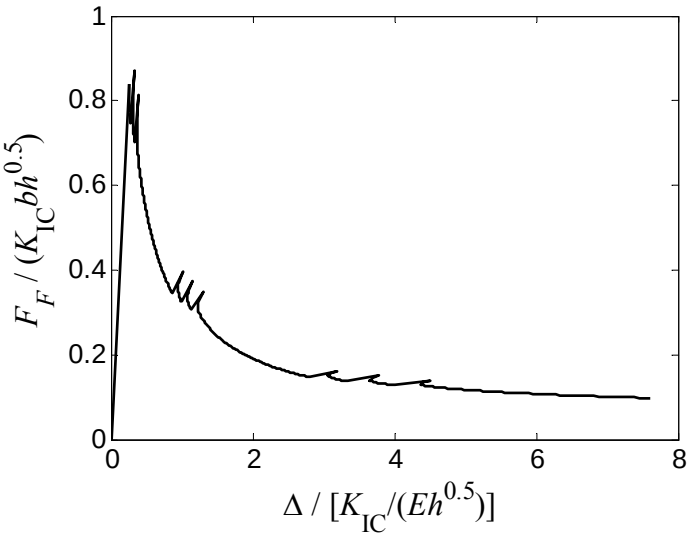

Fig. 6.8 Dimensionless tensile forces vs normalized local displacements for the beam without hierarchy shown in Fig. 6.5b

From Fig. 6.6 and Fig. 6.7 we can see that snap-back instability phenomena exist

in both the hierarchical levels. With the increase of the hierarchy level, the maximum strength is decreasing. In order to investigate the efficiency of hierarchy in structural design we have compared the 2 level hierarchy beam in Fig. 6.5a with the beam without hierarchy shown in Fig. 6.5b. From Fig. 6.7 and Fig. 6.8 we can see that the global tensile behavior trends of the two beams are similar. In the hierarchical beam (Fig. 6.7) the amplitude of snap back is much larger than that in the beam without hierarchy (Fig. 6.8), because level 1 is treated as a whole reinforcement for level 2. But the number of snap- back for the hierarchical beam is less than those of the beam without hierarchy. Also the maximum strength for the two levels hierarchical beam is larger than that of the same geometry beam without hierarchy, which in some extent may imply that hierarchy could be a better design strategy in material science.

6.5 Conclusions

In this chapter, the constitutive response of the discontinuous fiber reinforced brittle matrix composites are analyzed through the bridged crack model. Under the assumption of the rigid-plastic bridging law, the flexural and tensile behaviors of the composite beam are compared. Due to the nonlinear properties of the reinforcements and the way of crack length controlled loading, snap- back or snap-through phenomena appear in both cases. Results show that with the increasing of the brittleness number, a brittle to ductile transition phenomenon appears for the bending case but for the tensile case the responses always tend to be brittle with the increase of the crack length. This illustrates that size scale effects can be greatly influenced by loading configurations for the discontinuous fiber reinforced composites. At the same time, the bridged crack model is extended to the hierarchical case through the recursive method. A simple example about a two levels hierarchical beam is given and the results are compared with the beam of the same geometry without hierarchy. The maximum strength for the hierarchical case is larger than that without hierarchy, which in some extent suggests hierarchy as a promising strategy to maximize the strength of composites.

Appendix A

This appendix describes the adopted numerical procedure to plot Eq. (6.11) and Eq. (6.12), Eq. (6.6) and Eq. (6.10). Suppose there are *m* bridging fibers in the crack length. Under the assumption of rigid-perfectly plastic law for the reinforcements, the compatability equation for the flexural behavior can be expressed as

$$\{w\} = \{\lambda_M\} M_F - [\lambda]\{P\} = \{0\} \tag{A1}$$

in which $\{w\} = \{w_1, \cdots, w_m\}^{\mathrm{T}}$ is the vector of the crack opening displacements at different bridged levels, $\{P\} = \{P_1, \cdots, P_m\}^{\mathrm{T}}$ is the vector of the corresponded bridging forces, $\{\lambda_M\}$ and $[\lambda]$ are the vector of the localized compliances related to the bending moment M and the symmetrical $m \times m$ matrix whose generic element ij represents the localized compliance λ_{ij}. The general form of the localized compliances λ_{ij} for Fig. 6.1 is (Carpinteri and Massabo, 1997)

$$\lambda_{ij} = \frac{2}{E}\int_0^a \frac{K_{Ii}K_{Ij}}{P_i P_j} b \mathrm{d}a \tag{A2}$$

For the beam under bending in Fig. 6.1(b), by substituting (B1) and (B3) (see next Appendix) into Eq. (A2) we can get the following localized compliances:

$$\lambda_{iM} = \frac{2}{Ebh}\int_{\zeta_i}^{\xi} Y_M(y) Y_P(y, \zeta_i) \mathrm{d}y \tag{A3}$$

$$\lambda_{ij} = \frac{2}{Eb}\int_{\max[\zeta_i, \zeta_j]}^{\xi} Y_P(y, \zeta_i) Y_P(y, \zeta_j) \mathrm{d}y \tag{A4}$$

$$\lambda_{MM} = \frac{2}{Ebh^2}\int_0^{\xi} Y_M^2(y) \mathrm{d}y \tag{A5}$$

The integral singularity that may exist in (A3) and (A4) can be solved by using the trapezoidal quadrature rule, not necessarily the method introduced in reference (Bao and Suo, 1992) .

If no reinforcements are yielded, from (A1) we can get the vector for the bridging forces

$$\{p\} = [\lambda]^{-1} \{\lambda_M\} M \tag{A6}$$

Rearranging Eq. (A6) gives

$$p_i = r_i M \quad (i = 1, \cdots, m) \tag{A7}$$

The first plastic bending moment is

$$M_{P_1} = \frac{p_{P_1}}{r_1} \tag{A8}$$

Substituting Eq. (A7) into Eq. (6.5) we get the dimensionless crack propagation bending moment

$$\frac{M_{\mathrm{F}}}{K_{\mathrm{IC}} b h^{1.5}} = \frac{1}{Y_{\mathrm{M}}(\xi) - \sum_{i=1}^{m} r_i h Y_p(\xi, \zeta_i)} \tag{A9}$$

When $M_{\mathrm{F}} = M_{P_1}$ or $M_{\mathrm{F}} > M_{P_1}$, the first fiber $i = 1$ will yield.

If $n\ (1 \le n < m)$ fibers have yielded, we get the following form of the compatability equation:

$$\begin{Bmatrix} w_p \\ w_e \end{Bmatrix} = \begin{Bmatrix} \lambda_{M,p} \\ \lambda_{M,e} \end{Bmatrix} M - \begin{bmatrix} \lambda_{pp} & \lambda_{pe} \\ \lambda_{ep} & \lambda_{ee} \end{bmatrix} \begin{Bmatrix} p_p \\ p_e \end{Bmatrix} \tag{A10}$$

in which the subscripts *p* and *e* refer to *plastic* and *elastic* or *yielded* and *not yielded* respectively.

For the *n* yielded fibers the bridging forces are $P_i = P_{p_i}\ (1 \le i \le n)$. From $\{w_e\} = \{0\}$, we get

$$\{p_e\} = [\lambda_{pp}]^{-1} \left(\{\lambda_{M,e}\} M - [\lambda_{ep}] \{p_p\} \right) \tag{A11}$$

which implies that

$$p_i = r_i' M - r_i'' \quad (n+1 \le i \le m) \tag{A12}$$

The plastic bending moment for $n+1 \le i \le m$ is:

$$M_{P_i} = \frac{p_{P_i} + r_i''}{r_i'} \ (n+1 \le i \le m) \tag{A13}$$

Substituting Eq. (A13) into Eq. (6.5) we obtain the dimensionless crack propagation bending moment

$$\frac{M_{\mathrm{F}}}{K_{\mathrm{IC}} bh^{1.5}} = \begin{cases} \dfrac{1+\sum_{i=1}^{n} \dfrac{P_{p_i}}{K_{\mathrm{IC}} bh^{0.5}} Y_p(\xi,\zeta_i) - \sum_{i=n+1}^{m} \dfrac{r_i''}{K_{\mathrm{IC}} bh^{0.5}} Y_p(\xi,\zeta_i)}{Y_{\mathrm{M}}(\xi) - \sum_{i=n+1}^{m} r_i' h Y_p(\xi,\zeta_i)} & (n<m) \\ \dfrac{1+\sum_{i=1}^{n} \dfrac{P_{p_i}}{K_{\mathrm{IC}} bh^{0.5}} Y_p(\xi,\zeta_i)}{Y_{\mathrm{M}}(\xi)} & (n=m) \end{cases} \tag{A14}$$

Substituting Eqs. (A7) and (A9) or (A12) and (A14) into Eq. (6.12) gives the localized rotation ϕ.

Similarly, by simply revising the equations and repeat the process from (A1) to (A14) we can numerically plot Eq. (6.6) and Eq. (6.10) for the tensile case.

Appendix B

$$K_{IM} = \frac{M}{bh^{1.5}} Y_M(\xi) \tag{B1}$$

$$K_{IF} = \frac{F}{bh^{0.5}} Y_F(\xi) \tag{B2}$$

$$K_{Ii} = \frac{P_i}{bh^{0.5}} Y_P(\xi,\zeta_i) \tag{B3}$$

$$Y_M(\xi) = \frac{6\sqrt{2\tan\left(\frac{\pi}{2}\xi\right)}}{\cos\left(\frac{\pi}{2}\xi\right)}\left[0.923 + 0.199\left\{1-\sin\left(\frac{\pi}{2}\xi\right)\right\}^4\right] \tag{B4}$$

$$Y_F(\xi) = \frac{\sqrt{2\tan\left(\frac{\pi}{2}\xi\right)}}{\cos\left(\frac{\pi}{2}\xi\right)}\left[0.752 + 2.02\xi + 0.37\left\{1-\sin\left(\frac{\pi}{2}\xi\right)\right\}^3\right] \tag{B5}$$

$$Y_P(\xi,\zeta_i)=\frac{2}{\sqrt{\pi\xi}}\frac{1}{(1-\xi)^{1.5}\sqrt{1-\left(\frac{\zeta_i}{\xi}\right)^2}}G(\xi,\zeta_i)$$

$$G(\xi,\zeta_i)=g_1(\xi)+g_2(\xi)\frac{\zeta_i}{\xi}+g_3(\xi)\left(\frac{\zeta_i}{\xi}\right)^2+g_4(\xi)\left(\frac{\zeta_i}{\xi}\right)^3$$

$$g_1(\xi)=0.46+3.06\xi+0.84(1-\xi)^5+0.66\xi^2(1-\xi)^2$$

$$g_2(\xi)=-3.52\xi^2$$

$$g_3(\xi)=6.17-28.22\xi+34.54\xi^2-14.39\xi^3-(1-\xi)^{1.5}-5.88(1-\xi)^5-2.64\xi^2(1-\xi)^2 \quad \text{(B6)}$$

$$g_4(\xi)=-6.63+25.16\xi-31.04\xi^2+14.41\xi^3+2(1-\xi)^{1.5}+5.04(1-\xi)^5+1.98\xi^2(1-\xi)^2$$

References

Bazant, Z., Snap instability at crack ligament tearing and its implication for fracture micromechanics. *Cement and Concrete Research*, 1987, 17: 951-967.

Bocca, P., Carpinteri, A., Valente, S., Size effects in the mixed mode crack propagation: softening and snap-back analysis. *Engineering Fracture Mechanics*, 1990, 35: 159-170.

Bosco, C., Carpinteri, A., Debernardi, P., Fracture of reinforced concrete: size scale effects and snap-back instability. *Engineering Fracture Mechanics*, 1990, 35: 665-677.

Bosia, F., Buehler, M. J., Pugno, N., Hierarchical simulations for the design of supertough nanofibers inspired by spider silk. *Physical Review E*, 2010, 82: 056103.

Bao, G., Suo, Z., Remarks on crack-bridging concepts. *Applied Mechanics Reviews*, 1992, 45: 355-366.

Cox, B. N., Marshall, D. B., Concepts for bridged cracks in fracture and fatigue. *Acta Metallurgica et Materialia*, 1994, 42: 341-363.

Carpinteri, A., Massabo, R., Continuous vs discontinuous bridged-crack model for fiber-reinforced materials in flexure. *International Journal of Solids and Structures*, 1997, 34: 2321-2338.

Carpinteri, A., Spagnoli, A., Vantadori, S., An elastic–plastic crack bridging model for brittle-matrix fibrous composite beams under cyclic loading. *International Journal of Solids and Structures*, 2006, 43: 4917-4936.

Fratzl, P., Weinkamer, R., Nature's hierarchical materials. *Progress in Materials Science*, 2007, 52: 1263-1334.

Gao, H., Application of fracture mechanics concepts to hierarchical biomechanics of bone and bone-like materials. *International Journal of Fracture*, 2006, 138: 101-137.

Lakes, R., Materials with structural hierarchy. *Nature*, 1993, 361: 511-515.

Pugno, N., Mimicking nacre with super-nanotubes for producing optimized super-composites. *Nanotechnology*, 2006, 17: 5480-5484.

Ren, X., Li, J., Pragmatic analysis of material instability under strain control loading. *Engineering Fracture Analysis*, 2011, 18: 720-725.

Chapter 7

Conclusions and Outlook

The light weight cellular solids are widely used in industries and play a vital role in our daily life. Two of the most peculiar celluar solids are honeycombs and the carbon nanotube networks. With respaect to these two kinds of common cellular solids, what we care about are not only their mechicanl properties but also the potential multifunctionality they may have, in order that they could serve the human being more effectively and more conveniently. Therefore, in this thesis we have focused on the multifunctional hierarchical cellular solids, involving honeycombs and super carbon nanotubes, respectively.

Firstly, we reviewed some recent developments of honeycombs and carbon nanotube networks and summarized the potential multifunctionality they may show for practical applications.

In chapter 2, through the effective media model, the thermal and thermomechanical performances of the two-dimensional metal honeycombs (with relative density less than 0.3), hexagonal, triangular, square and Kagome honeycombs, are systematically studied. With respect to the overall thermal performance, regular hexagonal honeycombs are found to provide the highest level of heat dissipation. Under the same structural weight, the thermomechanical performance of Kagome honeycombs generally outperforms the other three kinds of honeycombs.

The multifunctional hierarchical honeycomb (MHH) is proposed in chapters 3 and 4. It is constructed by substituting the cell wall of an original regular honeycomb with five different equal mass lattices, hexagonal, triangular, Kagome, re-entrant hexagonal

and chiral honeycombs. Elastic and transport properties of the MHH with hexagonal, triangular and Kagome substructures are analyzed. In plane stiffness of the MHH with re-entrant hexagonal and chiral honeycombs are studied. Results show that the hexagonal sub-structure is difficult to greatly improve the elastic properties of the MHH structure, however, its counterparts, the triangular or Kagome sub-structures, result in a substantial improvement by 1 magnitude or even 3 orders of magnitude on the Young's and shear moduli of the MHH structure, depending on the cell-wall thickness-to-length ratio of the ORHH. By appropriately adjusting the geometrical parameters also both the re-entrant honeycomb (when the cell-wall thickness-to-length ratio of the ORHH is less than 0.045) and the chiral honeycomb (when the cell-wall thickness-to-length ratio of the ORHH is less than 0.75) can greatly tune the in-plane stiffness of the MHH structure.

The hierarchical fibers with a negative Poisson's ratio (NPR) for tougher composites is proposed in Chapter 5 and the related effective elastic moduli are calculated, based on the Euler beam theory. Under longitudinal axial tension, instead of shrinking, all levels of the NPR hierarchical tubes expand in the transverse directions. Using this kind of auxetic tubes as reinforced fibers in composite materials could produce a higher resistance to fiber pullout. In chapter 6 an application of the hierarchical fibers in bridged crack model is reported. Results show that for fiber reinforced brittle matrix composites size-scale effects are influenced by the loading configurations.

Still there are a lot of points we can focus in the future, such as the heat transfer efficiency and dynamic properties of the multifunctional hierarchical honeycombs (MHH), the methods to fabricate the MHH and the negative Poisson's ratio hierarchical fibers, and the experimental and numerical simulations to verify the analytical results obtained in this thesis.